Electronic and Optical Surface Properties of Noble Metals Studied by Reflection Anisotropy Spectroscopy

Jon-Kåre Hansen

Doktor ingeniøravhandling

Institutt for fysikk
Norges teknisk-naturvitenskapelige universitet, Trondheim

Abstract

The thesis demonstrates some of the possibilities of using light to measure and understand microscopic properties of noble metal and nickel surfaces. The work consist mainly of three parts:

1. The design and construction of a complete reflection anisotropy spectroscopy (RAS) system, connected to a ultra-high vacuum (UHV) chamber where samples can be cleaned and measured at pressure levels less than $1 \cdot 10^{-10}$ mbar.

2. Theoretical progress in classical local field effect calculations of resonant dipoles at (110) surfaces of noble metals. Methods to solve the plane-wise dipole-interaction coefficients are developed. It is investigated how variations in local-field effect model parameters including effective surface height and plasma-frequency, change the shape of the calculated spectra. In addition, it is discussed how imperfections in the surface, such as steps and vacancies, can be included in the model.

3. RAS measurements of clean and reconstructed surfaces Ag(110), Cu(110), Au(110), Au(100), Pt(100) and Ni(110) surfaces. The spectra for each of these surfaces are compared to theoretical model spectra. Using expressions for the screened dipole-dipole interaction we have found that the surface local-field effect contribute to the reflection anisotropy of all the above surfaces except for Pt(100). Transitions between surface states at the $\overline{Y}$ point of the surface Brillouin zone are responsible for features in the spectra of Ag(110), Cu(110). Many of the above surfaces have a reflection anisotropy that can be described by a phenomenological shift or broadening of the permittivity near a critical-point energy.

Preface

This thesis is submitted by the author to the Norwegian University of Science and Technology (NTNU), in partial fulfilment of the requirements for the doctoral degree "Doktor ingeniør". The research presented here has been carried out for almost four years; starting in 1995, with twelve months break for compulsory civil service. During this period I have participated in the evolving surface science group at the Department of Physics, NTNU.

At the time of submission, a cycle is completed for the RAS laboratory. When I arrived, the room was empty, where after we have filled it with mechanical, optical and electronic equipment to form the RAS-UHV system. Now, after finishing the thesis, the room is again empty, as a result of moving the complete system to 'Realfagsbygget'.

In addition to the results from our RAS system, I have also performed measurements (STM, RAS) at the STM laboratory at NTNU and at TU-Berlin (RAS). As part of my work with this thesis, I have contributed to six scientific papers in international publications, I participated in three international conferences (two of them with oral presentation of our work), I participated in three national conferences (two with oral presentation) and I was a member of the local committee of the international Workshop on Surface an Interface Optics 1997 in Ålesund.

I have found the working environment at the Group of Applied Optics in Trondheim to be both enjoyable and stimulating, and would like to thank everybody there, and at Sintef Anvendt Fysikk, for they encouraging support. In particular, I have greatly appreciated working with Johannes Bremer and Ola Hunderi. I would specifically like to thank them, together with Anne Borg, Håkon Mikkelsen, Magnus Reigstad, Lars Seime, Knut Stahrenberg, Theodore Hoffman, Wolfgang Richter, Turid Worren and Arnulf Bjølstad, Ove Holthe and all the others at the mechanical and electronic workshops. Finally, thanks to Trude, Magnus, Signe and Knut for keeping up with me these years.

Trondheim, 31.3.2000,
Jon-Kåre Hansen

Contents

List of acronyms

AC	Alternating current
ADC	Analog-to-digital converter
CF	Conflat flange
DC	Direct current
fcc	Face-centred cubic
HIBW	Half intensity bandwidth
IR	Infrared
LDA	Local density approximation
LEED	Low energy electron diffraction
LFE	Local-field effect
MOVPE	Metal organic vapour phase epitaxy
MUX	Multiplexer
PEM	Photoelastic modulator
RA	Reflection anisotropy
RAS	Reflection anisotropy spectroscopy
RASLab	The RAS system control software
RDS	Reflection difference spectroscopy
RMS	Root mean square
STM	Scanning tunneling microscopy
TSP	Titan sublimation pump
TTL	Transistor-transistor logic
UHV	Ultrahigh vacuum
UV	Ultraviolet

1 Introduction

A metal is characterised by high electrical and thermal conductivity and high reflectivity of light. Noble metals are characterised by being chemically reactive, especially with oxygen and water. For that reason they can often be found as pure elements in the nature, and they are used frequently for coins and jewellery. Copper, gold, silver, platinum, iridium, osmium, palladium, rhodium and ruthenium are all noble metals.

The surface of a noble metal is the part of the metal that is exposed to the ambients. Among the microscopic surface properties of interest are electronic states, geometrical arrangement and interaction with gas molecules. Many of the electronic properties differ from their bulk counterparts only in the 2-10 top atomic planes, corresponding to a surface layer with a thickness of a few nanometers. A number of experimental methods exist for examining the surface. They are typically based on electrons and photons with wavelength of the same order as the thickness of surface layer. For photons this often means x-rays.

1.1 Optical methods

Infrared (IR), visible and ultraviolet (UV) light is an economical alternative as an experimental tool compared to electrons and x-rays. Light can be used at any pressure and temperature, provides high resolution, can easily be aligned with the sample, and is easy to generate and detect. In addition, the photon energy for visible light (1.5 - 4 eV) is in the energy range of many interesting electronic transitions close to the Fermi level. The problem with light when measuring surface properties is the long photon wavelength. In the visible range it amounts to 400-800 nm. Consequently, reflected light typically contains information about the upper micrometer of the material. Although this large penetration depth makes it possible to probe hidden interfaces beneath the surface, the signal from the surface layer is often drowned in the bulk contribution.

In certain situations, it is still possible to single out information from only the top atom layers using visible light. Methods have been developed to measure the reflectivity difference between the substrate with and without a thin film. This method is called reflection difference spectroscopy (RDS). The resulting spectrum contains information about the film, or altered parameters of the top atom layers due to the existence of the film.

An alternative approach is to measure the reflection difference between two axes of the surface. If the bulk material has isotropic optical properties, then any measured deviation from zero will stem from the surface. Reflection anisotropy spectroscopy (RAS) is a normal incidence optical technique that uses polarised light to measure the surface anisotropy of a sample with an isotropic bulk.

The first to use a RAS (RDS) system to study surfaces were Aspnes and Studna [1] and Berkovitz *et al* [2]. Figure 1.1 shows the RAS spectrum of Si(110). The curve is measured by the author and is agreement with the spectrum published by Aspnes and Studna [1]. The company Bellcore holds a US patent for the application of RAS (RDS) on semiconductor growth monitoring. The first commercial RAS system was presented in 1990 by ISA Jobin Yvon [3], and today several companies supply pre-build RAS units. In general the specifications of self-made set-ups like ours exceed by far the commercial units (bandwidth,

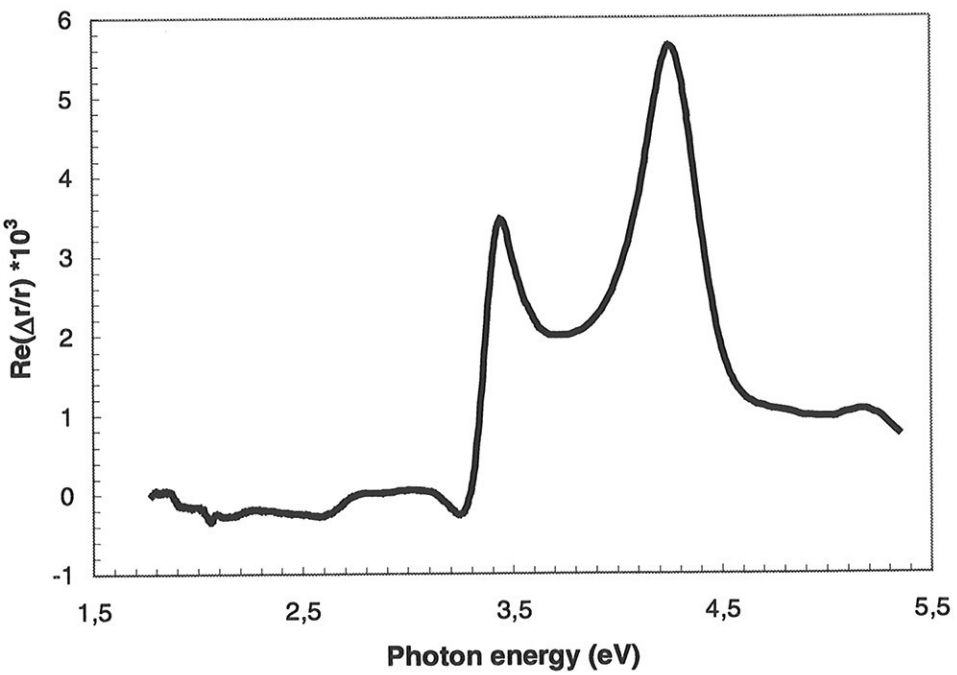

Figure 1.1. The RAS spectrum of Si(110), in agreement with the one published by Aspnes and Studna [1].

signal-to-noise ratio, resolution, etc.).

1.2 Optical properties of metals

Many interesting phenomena in physics involve interaction of a solid surface with foreign matter. If the interaction is weak, the surface responds to the external disturbance, but retains its individual identity. Any experiment whose goal is to probe the surface properties perturbs the surface in some way. In many cases the perturbation is excitations with respect to the physical state of charge, ion and spin variables of the system. The result is plasmon, phonon and magnon excitations, respectively.

The reflected light, the refractive index and the dielectric function

The measured reflection anisotropy spectra presented in this work result mainly from pertubations caused by incoming electromagnetic waves. A plane electromagnetic wave can be represented by constant amplitude E_0 multiplied by a position r and time-dependent t phase,

$$\vec{E} = \vec{E}_0 \exp\left[i(\vec{k}\cdot\vec{r} - \omega t)\right], \tag{1.1}$$

where $\vec{k} = \vec{k}_1 + i\vec{k}_2$ is the complex wave vector and ω the angular frequency. This wave is a solution of the Maxwell equations provided the wave vector and frequency satisfies the dispersion relation

$$\vec{k}\cdot\vec{k} = \frac{\omega^2}{c^2}\varepsilon, \tag{1.2}$$

where $\varepsilon \equiv \varepsilon_1 + \varepsilon_2$ is the complex dielectric function. We introduce the complex refractive index

$$N \equiv n + i\kappa = \sqrt{\varepsilon}, \tag{1.3}$$

where n and κ represent the real refractive index and attenuation index, respectively. The above equation can be reworked to give

$$\begin{aligned} \varepsilon_1 &= n^2 - \kappa^2 \\ \varepsilon_2 &= 2n\kappa \end{aligned}. \tag{1.4}$$

If a plane wave passes an interface between media of different dielectric constants, the wave splits into a reflected and refracted wave. From the boundary conditions of the electromagnetic field we can obtain the familiar Fresnel equations for the amplitude reflection coefficient r and the intensity reflection coefficient $R = |r|^2$. In the case of normal incidence

$$R = \frac{(n-1)^2 + \kappa^2}{(n+1)^2 + \kappa^2}. \tag{1.5}$$

The reflection coefficient gives information about the dielectric response of the material. On the other hand, to understand the contributions to the measured spectrum we need to consider the origin of the dielectric function. The main contribution to the dielectric function of metals originates from free electrons (intraband transitions) and bound electrons (interband transitions).

The validity of Fresnel formulas in RAS

The macroscopic constitutive relation between the electric displacement and the electric field

$$\vec{D} = \varepsilon \vec{E}, \tag{1.6}$$

has some undesirable features in microscopic surface physics. For example, the normal component of the electric field is required to be discontinuous for the Maxwell equation $\nabla \cdot \vec{D} = 0$ to be satisfied. A more general *non-local* relation between $\vec{D}$ and $\vec{E}$ is

$$\vec{D}(\vec{r}) = \int \mathrm{d}\vec{r}\,' \varepsilon(\vec{r}, \vec{r}\,') \vec{E}(\vec{r}\,'). \tag{1.7}$$

Thus, the electric displacement now depends on the electric field at other points in space. One way to recover the conventional formula is to assume that the field is slowly varying in space,

$$\vec{E}(\vec{r}\,') \approx \vec{E}(\vec{r}). \tag{1.8}$$

This electric field can be inserted into (1.7) to yield

$$\vec{D}(\vec{r}) = \left(\int \mathrm{d}\vec{r}\,' \varepsilon(\vec{r}, \vec{r}\,') \right) \vec{E}(\vec{r}), \tag{1.9}$$

where the permittivity has emerged as a spatial average. Again the normal component of the electric field is required to be discontinuous, which contradicts the assumption of a slowly varying field.

In reflection anisotropy spectroscopy the wavevector of the field of the incident wave is perpendicular to the surface. Consequently, the normal component of the electric field vanishes identically, and (1.6) is adequate for use with microscopic fields. This means that the Fresnel theory of refraction is valid for RAS, for example the reflection formula (1.5).

Intraband transitions

The response of free electrons to the external field is characterised by their numbers per unit volume N, the elementary charge e, their effective mass m_e and the characteristic electron-

lattice collision time (relaxation) τ. The additive contribution to the permittivity is the Drude dielectric function [74],

$$\varepsilon_{Drude} = 1 - \frac{\omega_p^2}{\omega(\omega + i/\tau)}, \tag{1.10}$$

where the plasma frequency ω_p is defined from

$$\omega_p^2 \equiv \frac{Ne^2}{\varepsilon_0 m_e}. \tag{1.11}$$

In the noble metals the outermost *s-p* electrons are nearly free-electrons, and the dielectric function resembles the Drude form for small photon energies.

Interband transitions

The energy $\hbar\omega$ of an incoming photon can be used to excite a bound electron from an occupied electron band state ψ_v with energy $E_v(\vec{k}_v)$ to an empty conduction band state ψ_c with energy $E_c(\vec{k}_c)$. It can be shown [75] that the additive contribution $\varepsilon_{interband}$ to the imaginary part of the dielectric function from these interband transitions is

$$\varepsilon_{2,interband} = \frac{\hbar^2 e^2}{\varepsilon_0 \pi^2 m^2 \omega^2} \left| \vec{e}_f \cdot \vec{M}_{vc} \right|^2 J(E_c - E_v). \tag{1.12}$$

Here m is the electron mass, $\vec{e}_f$ is the unit vector of polarisation in the direction of the electric field and $\vec{M}_{vc}$ is the matrix element describing the transition from ψ_v to ψ_c. The joint density of states,

$$J(\omega) = \int_S \frac{dS}{\left| \nabla_{\vec{k}} (E_c - E_v) \right|_{E_C - E_v = \hbar\omega}}, \tag{1.13}$$

measures the product density of full and empty states of equal energy difference. This quantity is thus mainly determining the interband contribution to the dielectric function.
Of special interest are frequencies corresponding to transitions between energy bands with the same gradient, i.e.

$$\nabla_{\vec{k}} E_c(\vec{k}) = \nabla_{\vec{k}} E_v(\vec{k}). \tag{1.14}$$

The integral of (1.13) then contains singularities, and the resulting set of values of ω and $\vec{k}$ defines *critical points* where the joint density of states and ε_2 have slope discontinuities.

Example: bulk dielectric function for gold

Noble metals typically have *d*-bands 2-4 eV below the Fermi level [74], and the electrons in these bands can therefore be excited by photons with energies corresponding to visible or near ultraviolet wavelengths. This situation is illustrated with gold as an example in Figure 1.2. The measured dielectric function is close to the theoretical Drude dielectric function (free electron contribution) for energies below 2 eV, whereas above this energy the interband contribution from electron transitions ($d \rightarrow$ Fermi level) is important.

The dielectric function as shown in Figure 1.2 is for the bulk of the isotropic lattice of gold. When we approach the surface, there may be a small shift or change of the curve. If the change depends on the in-plane crystallographic axis, the result is a reflectivity difference that

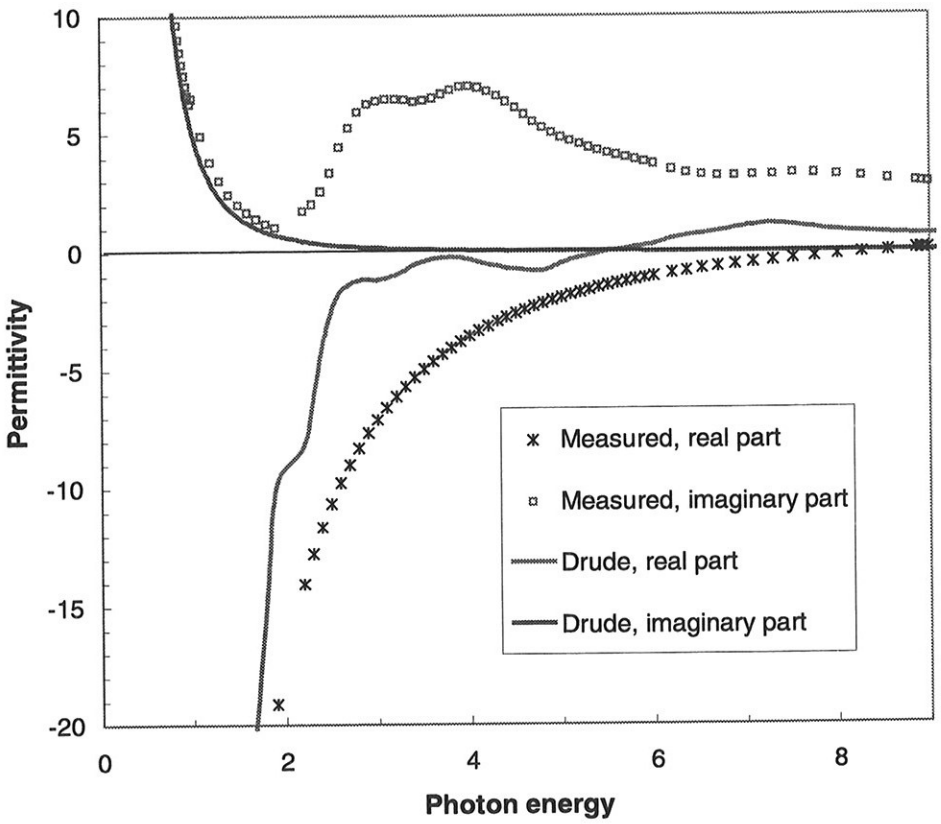

Figure 1.2 The dielectric function of gold. The theoretical Drude curves are calculated with $\hbar\omega_p = 8.5$ eV and $\tau = 9 \cdot 10^{-15}$ s.

can be measured by RAS.

Surface plasmons

The presence of a surface can influence the reflected light in additional ways, most notably by the excitations of surface plasmons. Consider a process where an incoming photon is absorbed and an electron in the crystal is excited from an occupied state to an unoccupied state above the Fermi level. In a metal, a superposition of electron-hole pairs can be formed that represent a wave-like perturbation of the charge density at the surface. This collective mode is called a **surface plasmon** (see for example [5]), and the electric field associated with it is

$$\vec{E} = \vec{E}_0 \exp(i\vec{k}_{\parallel} \cdot \vec{r}_{\parallel} - i\omega t)\exp(-k_{\perp}|r_{\perp}|) . \tag{1.15}$$

Here, $\vec{k}_{\parallel}$ and $\vec{k}_{\perp}$ is the parallel and normal components wave vector with respect to the surface. Note that the strength of the field decreases exponentially as we move away from the surface in both directions.

If the wave-like perturbation is excited by an incoming electric radiation, the resulting coupled mode of the radiation field and the surface plasmon is called a **surface plasmon polariton**. If the damping $1/\tau$ is small with respect to the oscillation frequency ω, as it is in the visible energy range for noble metals, we can use the Drude dielectric function as the response to the incoming electric wave,

$$\varepsilon(\omega) \approx 1 - \frac{\omega_p^2}{\omega^2} . \tag{1.16}$$

Applying the surface plasmon wave (1.15) to the boundary conditions at the surface, given by the Maxwell equation

$$\nabla \cdot \vec{D} = 0 , \tag{1.17}$$

and using (1.16), gives the following relation between q and ω for the polariton [5] (as long as $1 + \varepsilon(\omega) < 0$),

$$k_{\parallel}^2 = \left(\frac{\omega^2}{c^2}\right)\frac{\omega^2 - \omega_p^2}{2\omega^2 - \omega_p^2} . \tag{1.18}$$

This dispersion relation has two branches, as shown in Figure 1.3. In the same figure dispersion relations for photons for different values of $k_{\perp}$ is plotted. The lower branch goes asymptotically towards the *surface plasmon frequency* $\omega_s = \omega_p/\sqrt{2}$.

If an incoming photon of frequency ω and momentum $\vec{k} = \langle k_{\|}, k_{\perp} \rangle$ is absorbed and in the same process a surface plasmon is excited, conservation of energy and momentum require the surface plasmon wave to have an equal frequency ω and momentum $k_{\|}$. Therefore, this process takes place only at a crossing between photon and surface plasmon dispersion curves in Figure 1.3. No excitation of any kind exists in the frequency range between ω_s and ω_p. Above ω_p, incoming photons can couple to surface plasmons, but the energy immediately leaks into the degenerate bulk continuum. As the incident beam is tilted towards grazing incidence ($k_z \rightarrow 0$), the photon dispersion line tilts towards the lower branch. However, it never intersects the surface plasmon dispersion, and therefore there is apparently *no* angle of incidence for which the true plasmon surface polariton (lower branch) can be excited.

The above situation is changed for a surface with some roughness of period b. Then external light can couple to the polariton via an *umklapp* process that supplies the additional needed momentum $K = 2\pi n/b$ [6]. This is illustrated in Figure 1.3 as a 'dispersion' line shifted towards higher momentum values. An anisotropy in the surface roughness makes it possible

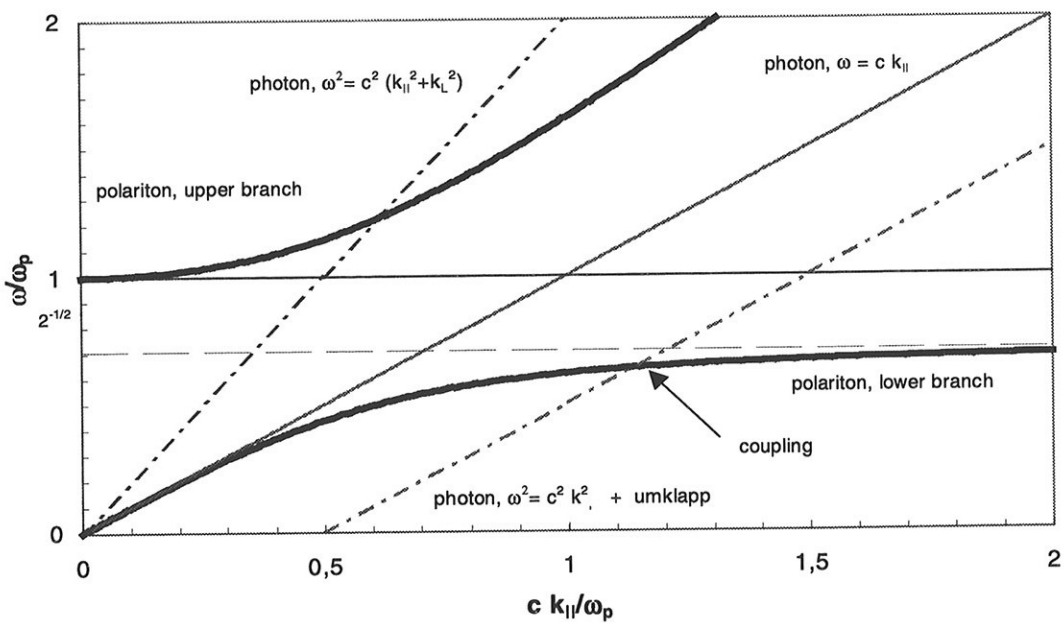

Figure 1.3. Dispersion for the surface plasmon polariton for long wavelengths for a Drude metal in air.

that surface plasmons can influence the reflection anisotropy spectrum.

At shorter wavelengths (larger $k_{||}$), when atomic dimensions are approached, we need to take into account the distribution of charge at the surface. When a crystal is cleaved, electrons will spill out from the new surface, creating a smooth, dipolar, transition between the crystal and vacuum. The jellium model therefore defines an effective surface $d_{||}$ at

$$d_{||} = \frac{1}{\bar{n}} \int_{-\infty}^{\infty} \mathrm{d}z \; z \frac{\mathrm{d}n(z)}{\mathrm{d}z}. \tag{1.19}$$

Here, n is the density distribution of the electron gas, $\bar{n}$ is equal to the positive background charge, the z-axis is normal to the surface and $z = 0$ defines the surface. Another definition of the surface is the *centroid* of the charge distortion $\delta n(z)$ induce by the presence of an electron outside the metal:

$$d_{\perp} = \frac{\int_{-\infty}^{\infty} \mathrm{d}z \; z \, \delta n(z)}{\int_{-\infty}^{\infty} \mathrm{d}z \; \delta n(z)}. \tag{1.20}$$

With $d_{||}$ and $d_{\perp}$ characterising the effective surface, it can be shown that the jellium surface plasmons dispersion then takes the Feibelman form [7],

$$\omega(k_{||}) = \frac{\omega_p}{\sqrt{2}} \left(1 + \frac{1}{2} k_{||} (d_{||} + d_{\perp}) + \ldots \right). \tag{1.21}$$

The slope of the plasmon dispersion in this wavelength range indicates whether the centroid and effective surface is above or below the mathematical surface ($z = 0$).

1.3 Outline of the thesis

The experimental and theoretical work described in this work deals mainly with reflection anisotropy spectroscopy data. In Chapter 2 the main optical principles and expressions used in reflection anisotropy spectroscopy are presented. There seems to be a lack of a standard reference showing how those expressions are calculated, resulting in a mixture of different definitions and erroneous terms. Therefore, a full development of the RAS intensity for our type of set-up is included, as well as a brief discussion on how different imperfections can affect the measured signal.

Chapter 3 is a reference on the design of our self-made RAS instrument, on the vacuum chamber, on the system control software, on how measurements and calibration are done and on the effect of instrument errors. Several design trade-offs are discussed, and details about components important for RAS is given.

The local-field effect of resonant surface dipoles is presented in Chapter 4. It is a rather thorough explanation of the theory. It shows the method and expressions we used to calculate all the plane-wise dipole-dipole interaction coefficients, and some of the numerical values are tabulated in Appendix B. Furthermore, new developments that include the variation of the effective surface height and approximation of the effect of sputtering are presented.

In Chapter 5, several results obtained from calculations and with the RAS system are presented. In addition to the noble metal surfaces Ag(110), Cu(110), Au(110), Au(100) and Pt(100), results from the Ni(110) surface is reported. Most of the sections are merely revised versions of published papers, whereas the others are papers to be published.

1.4 Suggestion for further research

Being at the end of a five-year research period on reflection anisotropy spectroscopy, it is time to reflect over possible future opportunities related to the work in this thesis. As far as the instrument is concerned, the new digital lock-in amplifiers introduce some interesting possibilities. In particular, the opportunity to measure higher harmonics of the reference ($n >$ 2) can give less noise in the spectra (with the same integration time).

A rather new technique is reflection anisotropy microscopy (μRDS) [4]. By inserting a lens between the polariser/PEM and the sample, it is possible to sharpen the focus of the rays, so that the surface can be scanned. The result is an image of reflection anisotropy of the sample surface. This map contains information on features in both the top layer as well as the underlying layers. The problem with this technique is that the extra lens influences the polarisation of the incoming and reflected beams.

If the RAS instrument is to be useful in industrial applications, miniaturisation of the standard set-up is needed, both regarding optical and electronic components. It is possible to get rid of the lock-in amplifier and the driver for the photoelastic modulator by using a standard analog-

to-digital converter. New converter cards are more than able to perform those tasks if used in the right way.

For the local-field effect theory, the next step to an improved theory is to reconsider the abrupt electronic surface. It should be replaced by a smooth transition to vacuum.

Regarding measurements, there are still a lot to be done. The recent results for silver stress the importance and the strength of being able to combine RAS with STM. And the discoveries for the Ag(110) surface raises the question how the step distortion on the surface affects the other noble metal surfaces as well.

Another area of interest is homoepitaxy on noble metals, for example silver growth on silver. This is what RAS was made for: time-dependent spectra of growth variations on the surface. Time dependent RAS can give a lot of information about time constants and activation energies for simple catalytic reactions on metal surfaces, for example platinum.

2 Theory of RAS measurements

2.1 The idea of reflection anisotropy spectroscopy

When an electromagnetic wave *E* arrives at a metal surface, a part of the wave is reflected, as shown in Figure 2.1. The reflection coefficient is the ratio between the amplitude of the incoming electric field and the electric field reflected by the surface,

$$r_x = \frac{E_x^{reflected}}{E_x^{incoming}}. \tag{2.1}$$

The reflection coefficient depends upon the dielectric function and other material properties. The typical penetration depth is of the order of the wavelength of the optical field. As stated earlier, one would expect that the reflection of light probe properties in the 100-1000 nm region closest to the surface. However, in surface physics, we are interested in information about the two or three topmost atom layers, a typical depth of 1 nm. If these layers are anisotropic, and the rest of the material (the *bulk*) is isotropic, the surface information can be obtained by taking the difference in reflection between two orthogonal directions in the surface. Reflection anisotropy spectroscopy (RAS) is a technique that measures this difference,

$$\frac{\Delta r}{r} \equiv \frac{r_x - r_y}{(r_x + r_y)/2}. \tag{2.2}$$

The difference is normalised to factor out the contribution from the isotropic bulk. Typically, the signal is of order 10^{-3} (1 nm / 1000 nm) of the reflectivity, and special measurement

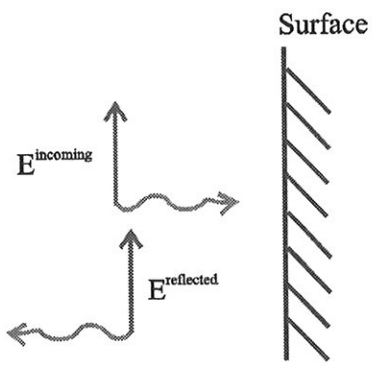

Figure 2.1. Reflection of an electromagnetic wave

techniques must be used to distinguish the signal from noise. In our case, this is accomplished by the combination of a photoelastic modulator, a lock-in amplifier and computer software. Since we mainly are searching for microscopic electronic properties of metal surfaces, we are interested in the difference in reflectivity as a function of frequency.

Face-centred cubic crystals

Noble metals are known to have atoms arranged in a face-centred cubic (fcc) lattice. The reflection coefficient and dielectric function in the bulk of this type of crystal is isotropic for

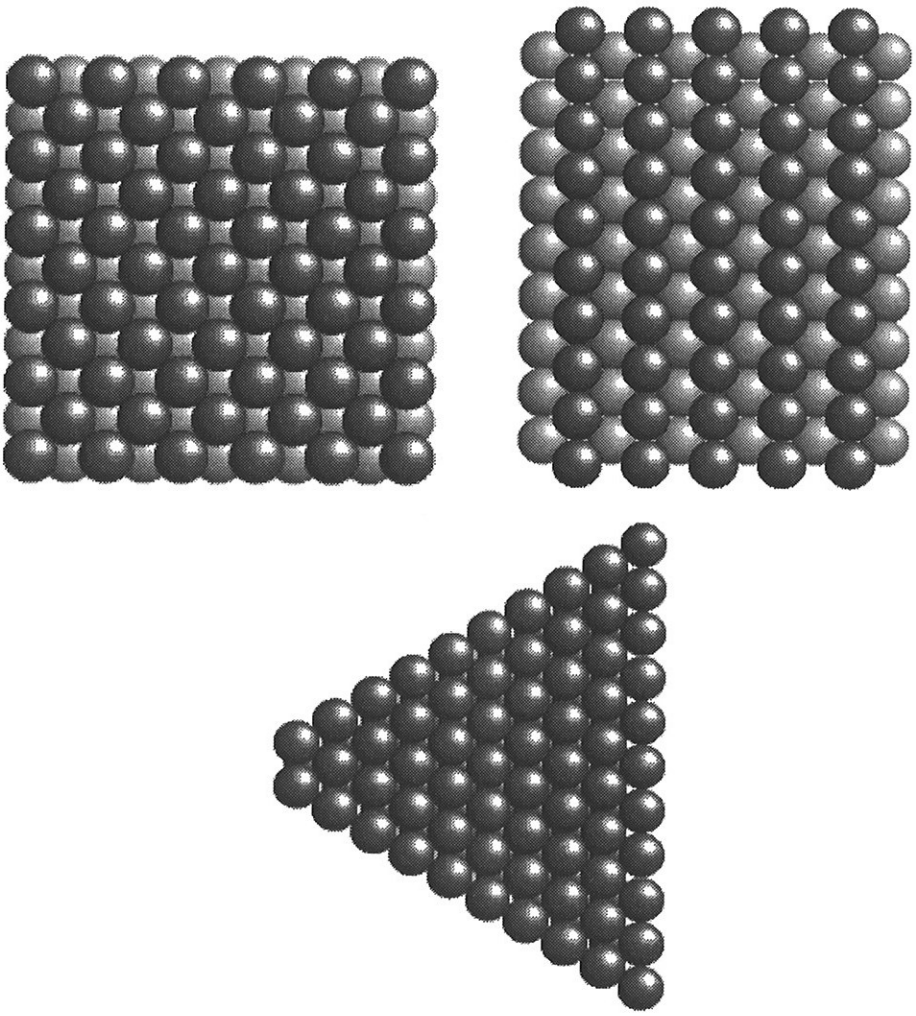

Figure 2.2. Surfaces of fcc crystals: (100) (left), (110) (right), and (111) (below).

optical wavelengths, i.e. it does not depend on direction in the crystal. Whether the surface is anisotropic or isotropic is determined by how the crystal is cut. The three most closely packed ideal surfaces of fcc crystals are shown in Figure 2.2. Of these, only the (110) surface is anisotropic when in a clean state. Consequently, only the (110) surface of an fcc crystal is suitable for RAS measurements, because i) the surface is anisotropic and ii) the bulk is isotropic.

Reconstructed surfaces

The cleavage of a crystal liberates a fixed amount of energy, and as a result, many surfaces reconstruct to a stable or metastable phase to lower the internal energy. Heating the surface can produce the same effect. A substantial part of these reconstructed surfaces are highly anisotropic, with an isotropic bulk, and are suitable for examination by RAS. For example, the Au(100) and Pt(100) surface form a wavelike pseudo-hexagonal reconstruction of the top atom layer [76]. Another example is the Au(110) surface, also reconstruced at room temperature, with a 2x1 missing row top layer. Heating the Au(110) crystal to 650 K removes the reconstruction in a reversible way [77].

Exposing a non-reconstructed surface to a certain amount of gas can initiate a phase reconstruction as well. For example, the clean Ni(110) surface reconstructs to a (2x1) phase after exposure to 4 Langmuirs (L) of O_2, with a subsequent heating to 600 K. In this case, the chemisorption of oxygen triggers the phase change. Subsequent exposure to oxygen produces a (3x1) reconstructed Ni(110) surface. This surface and its RAS spectra are discussed in more detail in Section 5.7.

2.2 RAS set-up

A frequently used reflection anisotropy set-up was first described by Aspnes [1]. Our spectrometer, based on the one used by Aspnes, is shown in Figure 2.3. Light from the xenon arc light source is sent trough a polariser so that the electric field is oriented along one transversal direction (0°). The light-rays hit the sample at normal incidence. The sample is arranged such that the incoming polarisation has a direction that is 45° with respect to the main crystallographic axes. In this way, the amount of light that probes the reflection along each crystallographic axis is equal.

When the light is reflected from the sample the polarisation may have changed. If the reflection coefficient of the sample is isotropic, the light will still be linearly polarised, otherwise, the light will be more or less elliptically polarised. The part of light that is polarised orthogonally to the original polarisation (90°) contains information about any difference in reflectivity between the two crystallographic axes, the reflection anisotropy (RA). In typical applications, this part accounts for less than 1 % of the total intensity.

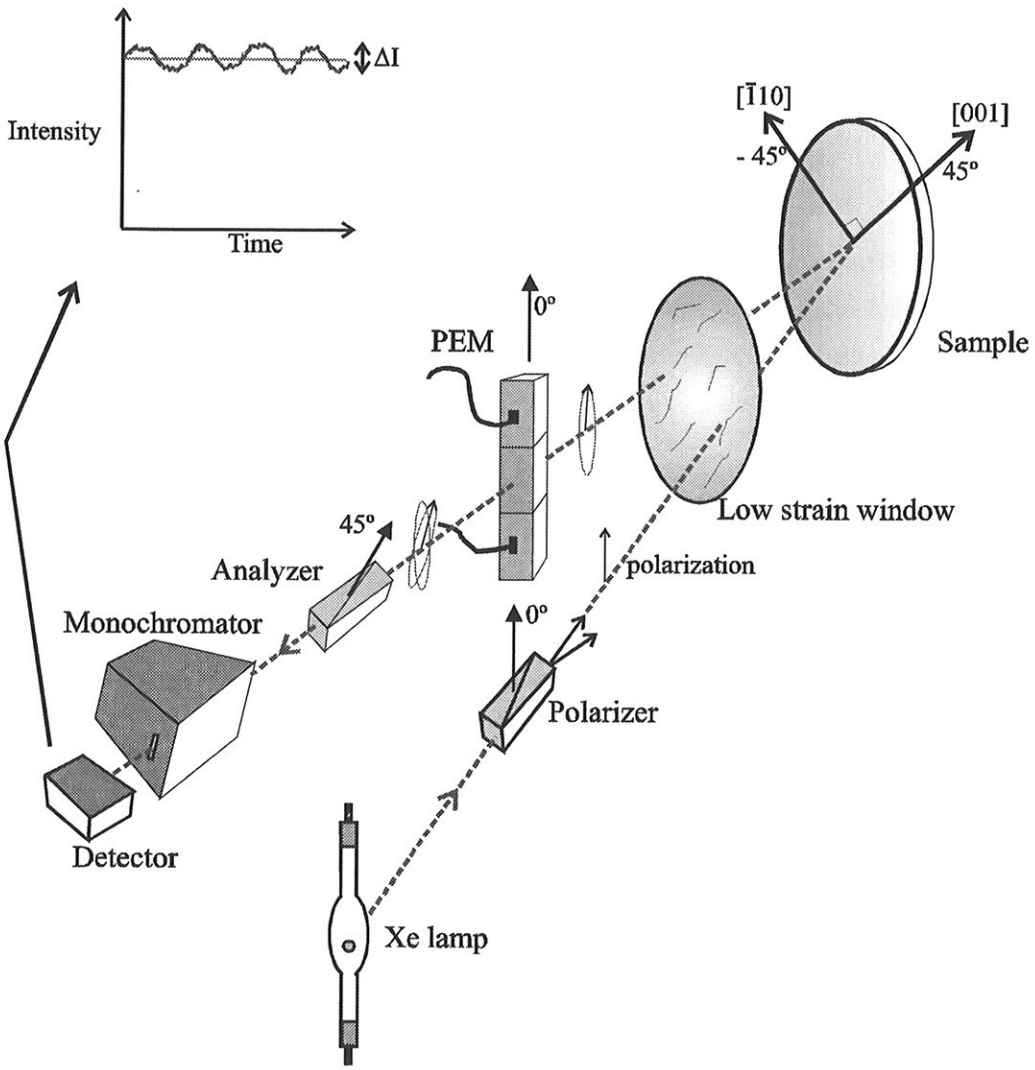

Figure 2.3. Principal set-up of the reflection anisotropy spectrometer

To investigate the RA we use a photoelastic modulator (PEM) and a polariser (analyser) in the path of the beam. The PEM modulates the index of refraction in one direction (90°) with a harmonic frequency close to 50 kHz. The analyser then ensures that the periodic variation of the electric field amplitude vector is translated into an intensity variation. To measure a small wavelength band the light has to go trough the monochromator. At the end of the optical path the detector measures the intensity.

We can calculate an explicit expression for the light intensity at the detector, and relate it to the reflection anisotropy. In agreement with Figure 2.3, we use a right-hand coordinate system with the z-axis pointing along the ray and the x-axis along the 0° direction.

2.3 Jones matrices

It is possible to represent all the optical elements of the RAS set-up by Jones matrices. To calculate the total effect of the system one just multiplies all these matrices. Given the incoming electric field one can then calculate the resulting intensity. By referring to Figure 2.3, we first define each matrix.

Polariser

The light-beam that reaches the polariser is unpolarised. Photons polarised along the x-axis is transmitted. On the other hand, only a very small part a_p of photons polarised along the y-axis passes the polariser. It is difficult to exactly align the axis of polarisation along the x-axis, so that in general a small rotation error ΔP is introduced. Therefore, the electrical field after the polariser is

$$\vec{E}_0 = R(-\Delta P)\begin{pmatrix} 1 \\ ia_p \end{pmatrix} \approx \begin{pmatrix} 1 \\ ia_P + \Delta P \end{pmatrix}. \tag{2.3}$$

Here, we have used the definition of the matrix for rotation of the coordinate system,

$$R(\alpha) \equiv \begin{pmatrix} \cos(\alpha) & \sin(\alpha) \\ -\sin(\alpha) & \cos(\alpha) \end{pmatrix}. \tag{2.4}$$

Note that rotating the Jones matrix an angle $-\alpha$ is equivalent to rotating the coordinate system an angle α.

Low-strain UHV window

In principle we want no other element between the polariser and the PEM than the sample, to avoid any change in polarisation. However, when the sample is situated in vacuum, light has to pass twice through the optical window at the chamber. A special type of low-strain window is therefore used to minimise the window effect. If we assume that we know the phase difference δ between two orthogonal axes, (x', y'), and the angle between x and x' is θ, then the Jones-matrix for each pass through the window is

$$J_{Window} = R(-\theta)\begin{pmatrix} e^{i\frac{\delta}{2}} & 0 \\ 0 & e^{-i\frac{\delta}{2}} \end{pmatrix} R(\theta)$$

$$\approx \begin{pmatrix} 1+i\frac{\delta}{2}\cos(2\theta) & i\frac{\delta}{2}\sin(2\theta) \\ i\frac{\delta}{2}\sin(2\theta) & 1+i\frac{\delta}{2}\cos(2\theta) \end{pmatrix}. \qquad (2.5)$$

If there is no window in the path of the beam, this matrix is reduced to unity.

Sample

The two orthogonal axes r_{45} and r_{-45} on the sample surface are rotated an angle $\gamma \approx -45°$ from the (x, y)-axes, and the matrix for the sample becomes

$$J_{Sample} = R(-\gamma)\begin{pmatrix} r_{-45} & 0 \\ 0 & r_{45} \end{pmatrix} R(\gamma)$$

$$= \begin{pmatrix} r_{-45}(\cos\gamma)^2 + r_{45}(\sin\gamma)^2 & r_{-45}\sin\gamma\cos\gamma - r_{45}\cos\gamma\sin\gamma \\ r_{-45}\cos\gamma\sin\gamma - r_{45}\sin\gamma\cos\gamma & r_{-45}(\sin\gamma)^2 + r_{45}(\cos\gamma)^2 \end{pmatrix} \qquad (2.6)$$

$$\approx \begin{pmatrix} \bar{r} & \frac{1}{2}\Delta r \\ \frac{1}{2}\Delta r & \bar{r} \end{pmatrix}$$

In addition, due to the nature of the reflection, the z-axis is reflected, and the component of the electric field along the y-axis changes sign. This is taken care of by the following Jones-matrix:

$$J_{Fold} = \begin{pmatrix} 1 & 0 \\ 0 & -1 \end{pmatrix} \qquad (2.7)$$

Note that this component enters only because of our definition of the coordinate system.

Photoelastic modulator

As for the polariser, the difficulty in exactly aligning the modulator so that the main axis is along the x-axis introduces an error in angle of ΔM. The modulator has a phase difference ϕ between the two orthogonal axes. The phase difference is modulated, so that

$$\phi = \delta_m \cos \omega_{PEM} t\,, \tag{2.8}$$

where $2\pi\ \omega_{PEM}$ amounts to 50 kHz, and δ_m is the amplitude of the phase difference. The resulting Jones matrix is:

$$\begin{aligned} J_{PEM} &= R(-90-\Delta M)\begin{pmatrix} e^{i\frac{\phi}{2}} & 0 \\ 0 & e^{-i\frac{\phi}{2}} \end{pmatrix} R(+90+\Delta M) \\ &\approx \begin{pmatrix} e^{-i\frac{\phi}{2}} & -\Delta M(e^{i\frac{\phi}{2}} - e^{-i\frac{\phi}{2}}) \\ -\Delta M(e^{i\frac{\phi}{2}} - e^{-i\frac{\phi}{2}}) & e^{i\frac{\phi}{2}} \end{pmatrix}. \end{aligned} \tag{2.9}$$

The above expression is valid for small angles ΔM.

Analyser

Since the analyser is a polariser, there will be a small error a_a similar to the error a_p for the polariser described earlier. The analyser is aligned an angle $\nu \approx 45°$. By setting $\nu = \pi/4 + \Delta A$ and approximate to the first order, we get

$$\begin{aligned} J_{Analyzer} &= \begin{pmatrix} 1 & 0 \\ 0 & ia_a \end{pmatrix} R(\nu) \\ &\approx \frac{1}{\sqrt{2}}\begin{pmatrix} 1-\Delta A & 1+\Delta A \\ -ia_a & ia_a \end{pmatrix}. \end{aligned} \tag{2.10}$$

There is no need to rotate the coordinate system back to its original state, as we will use only the intensity of the light at the detector.

2.4 Wave amplitude at the detector

The amplitude of the electric field at the detector is obtained by taking the field at the polariser, and multiply with the Jones matrices for the other optical components in the same order as they are passed by the light-beam,

$$\vec{E}_{Detector} = J_{Analyzer} \times J_{PEM} \times J_{Window2} \times J_{Fold} \times J_{Sample} \times J_{Window1} \times \vec{E}_0\,. \tag{2.11}$$

We define the window-strain factors

$$\begin{aligned} F_{1c} &= i\frac{\delta_1}{2}\cos 2\theta_1 \\ F_{1s} &= i\frac{\delta_1}{2}\sin 2\theta_1 \\ F_{2c} &= i\frac{\delta_2}{2}\cos 2\theta_2 \\ F_{2s} &= i\frac{\delta_2}{2}\sin 2\theta_2 \end{aligned} \quad . \tag{2.12}$$

The multiplication is performed by neglecting all second-order and higher terms,

$$\begin{aligned} \vec{E}_{detektor} \equiv \begin{pmatrix} E_1 \\ E_2 \end{pmatrix} &= \cdots\cdots \begin{pmatrix} 1+F_{1c} & F_{1s} \\ F_{1s} & 1+F_{1c} \end{pmatrix}\begin{pmatrix} 1 \\ ia_P + \Delta P \end{pmatrix} \\ &\approx \cdots\cdots \begin{pmatrix} 1 & 0 \\ 0 & -1 \end{pmatrix}\begin{pmatrix} \bar{r} & \frac{1}{2}\Delta r \\ \frac{1}{2}\Delta r & \bar{r} \end{pmatrix}\begin{pmatrix} 1+F_{1c} \\ ia_P + \Delta P + F_{1s} \end{pmatrix} \\ &\approx \cdots\cdots \bar{r}\begin{pmatrix} 1+F_{2c} & F_{2s} \\ F_{2s} & 1+F_{2c} \end{pmatrix}\begin{pmatrix} 1+F_{1c} \\ -\frac{1}{2}\frac{\Delta r}{\bar{r}} - ia_p - \Delta P - F_{1s} \end{pmatrix} \\ &\approx \cdots \bar{r}\begin{pmatrix} e^{-i\frac{\phi}{2}} & -\Delta M(e^{i\frac{\phi}{2}} - e^{-i\frac{\phi}{2}}) \\ -\Delta M(e^{i\frac{\phi}{2}} - e^{-i\frac{\phi}{2}}) & e^{i\frac{\phi}{2}} \end{pmatrix}\begin{pmatrix} 1+F_{1c}+F_{2c} \\ -\frac{1}{2}\frac{\Delta r}{\bar{r}} - ia_p - \Delta P - F_{1s} + F_{2s} \end{pmatrix} \\ &\approx \frac{\bar{r}}{\sqrt{2}}\begin{pmatrix} 1-\Delta A & 1+\Delta A \\ -ia_a & ia_a \end{pmatrix}\begin{pmatrix} e^{-i\frac{\phi}{2}}(1+F_{1c}+F_{2c}) \\ e^{i\frac{\phi}{2}}\left(-\frac{1}{2}\frac{\Delta r}{\bar{r}} - ia_p - \Delta P - \Delta M - F_{1s} + F_{2s}\right) + e^{-i\frac{\phi}{2}}\Delta M \end{pmatrix} \\ &\approx \frac{\bar{r}}{\sqrt{2}}\begin{pmatrix} e^{-i\frac{\phi}{2}}(1-\Delta A+\Delta M+F_{1c}+F_{2c}) + e^{i\frac{\phi}{2}}\left(-\frac{1}{2}\frac{\Delta r}{\bar{r}} - ia_p - \Delta P - \Delta M - F_{1s} + F_{2s}\right) \\ e^{-i\frac{\phi}{2}} ia_a \end{pmatrix} \end{aligned} \tag{2.13}$$

We have assumed that: i) $\Delta r/r$ is small (true for isotropic bulk samples), ii) δ_1 and δ_2 are small (true for low-strain windows), iii) ΔM, ΔA and ΔP are small (true if we do a reasonably good job when aligning the optics), iv) a_a and a_p are small (true if polarisers are of good quality).

2.5 Detector intensity

The Poynting vector $\vec{S}$ gives the instantaneous energy flux,

$$\vec{S} = \frac{1}{\mu_0}\left(\vec{E} \times \vec{B}\right) = I(t)\vec{s}\,. \tag{2.14}$$

This equation defines the instantaneous intensity of the electromagnetic wave as the absolute value of the energy flux along the ray direction unit $\vec{s}$. If the electric field is decomposed into complex valued plane waves of frequency ω, the intensity is

$$I = \frac{1}{2}\sqrt{\frac{\varepsilon}{\mu_0}}\vec{E}\cdot\vec{E}^*, \tag{2.15}$$

where the star denotes complex conjugate. The second component of $\vec{E}_{detector}$ in (2.13) contributes only to second order terms of the intensity, so that to the first order we have

$$\begin{aligned} I &= \frac{1}{2}\sqrt{\frac{\varepsilon}{\mu_0}}E_1E_1^* \\ &\approx \frac{1}{2}\sqrt{\frac{\varepsilon}{\mu_0}}\frac{|\bar{r}|^2}{2}(1-2\Delta A+2\Delta M) \\ &+\frac{1}{2}\sqrt{\frac{\varepsilon}{\mu_0}}\frac{|\bar{r}|^2}{2}(e^{i\phi}+e^{-i\phi})\left(-\frac{1}{2}\mathrm{Re}\frac{\Delta r}{\bar{r}}-\Delta P-\Delta M\right) \\ &+\frac{1}{2}\sqrt{\frac{\varepsilon}{\mu_0}}\frac{|\bar{r}|^2}{2}(e^{i\phi}-e^{-i\phi})\left(-i\frac{1}{2}\mathrm{Im}\frac{\Delta r}{\bar{r}}-ia_p-F_{1s}+F_{2s}\right) \end{aligned} \tag{2.16}$$

The exponentials can be rewritten as $\cos\phi$ and $\sin\phi$ respectively, and taking note from (2.8) that the phase ϕ of the photoelastic modulator is time-dependent, we develop these functions as series of Bessel-functions of the first kind:

$$\begin{aligned} \cos\phi &= \cos(\delta_m \sin\omega_{PEM}t) \\ &= J_0(\delta_m)+2J_2(\delta_m)\cos 2\omega_{PEM}t+2J_4(\delta_m)\cos 4\omega_{PEM}t+\dots \\ \sin\phi &= \sin(\delta_m \sin\omega_{PEM}t) \\ &= 2J_1(\delta_m)\sin\omega_{PEM}t+2J_3(\delta_m)\sin 3\omega_{PEM}t+\dots \end{aligned} \tag{2.17}$$

The intensity may then be expressed as

$$\begin{aligned} I &= \frac{1}{2}\sqrt{\frac{\varepsilon}{\mu_0}}\frac{|\bar{r}|^2}{2}(1-2\Delta A+2\Delta M+\left(-\mathrm{Re}\frac{\Delta r}{\bar{r}}-2\Delta P-2\Delta M\right)J_0(\delta_m)) \\ &+\frac{1}{2}\sqrt{\frac{\varepsilon}{\mu_0}}\frac{|\bar{r}|^2}{2}\left(-\mathrm{Im}\frac{\Delta r}{\bar{r}}-2a_p-\delta_1\sin 2\theta_1+\delta_2\sin 2\theta_2\right)2J_1(\delta_m)\sin\omega_{PEM}t \\ &+\frac{1}{2}\sqrt{\frac{\varepsilon}{\mu_0}}\frac{|\bar{r}|^2}{2}\left(-\mathrm{Re}\frac{\Delta r}{\bar{r}}-2\Delta P-2\Delta M\right)2J_2(\delta_m)\cos 2\omega_{PEM}t \\ &+ \text{ terms of higher harmonics} \end{aligned} \tag{2.18}$$

The first term is frequency independent, and can be denoted $\bar{I}$, as it is the time-averaged intensity. The other terms ΔI are time-dependent, and we write

$$I = \bar{I} + \Delta I \tag{2.19}$$

By taking the ration between the time-dependent and time-averaged part of the RAS intensity, we get to the first order

$$\begin{aligned}\frac{\Delta I}{\bar{I}} = & 2\left(-\mathrm{Im}\frac{\Delta r}{\bar{r}} - 2a_p - \delta_1 \sin 2\theta_1 + \delta_2 \sin 2\theta_2\right) J_1(\delta_m) \sin \omega_{PEM} t \\ & +2\left(-\mathrm{Re}\frac{\Delta r}{\bar{r}} - 2\Delta P - 2\Delta M\right) J_2(\delta_m) \cos 2\omega_{PEM} t\end{aligned} \tag{2.20}$$

To be able to measure the reflection anisotropy (RA), we need a detector that represents the intensity of the electromagnetic wave as a proportional voltage U, with a *bandwidth* of more than $2\omega_{PEM}\, t$. For the real and imaginary part we get respectively,

$$\begin{aligned}\mathrm{Re}\frac{\Delta r}{\bar{r}} &= -2\Delta P - 2\Delta M - \frac{1}{2J_2(\delta_m)} \frac{\Delta I|_{\cos 2\omega t}}{\bar{I}} \\ &= -2\Delta P - 2\Delta M - \frac{1}{\sqrt{2}J_2(\delta_m)} \frac{\Delta U_{2\omega}^{rms}}{\bar{U}}\end{aligned} \tag{2.21}$$

$$\mathrm{Im}\frac{\Delta r}{\bar{r}} = -2a_p - \delta_1 \sin 2\theta_1 + \delta_2 \sin 2\theta_2 - \frac{1}{\sqrt{2}J_1(\delta_m)} \frac{\Delta U_w^{rms}}{\bar{U}} \tag{2.22}$$

It is clear from the above expressions that the measurement of the real part of the reflection anisotropy is sensitive to the alignment of the polariser and the photoelastic modulator. It is the *relative* difference in misalignment that matters, as long as the misalignment is small. The imaginary part is sensitive to window strain and leaks in the polariser.

In the above calculation, *depolarisation* has been ignored completely as this effect cannot be included in the Jones matrices. However, a small part of the light will be unpolarised at the detector due to depolarisation as the light passes each optical element. The intensity from unpolarised photons will contribute to the total intensity, but not to the modulated intensity. Therefore, from (2.20) it is seen that depolarisation decreases the measured reflection anisotropy signal, but the structure of the spectra will be unchanged.

Comparison to Aspnes' expression

Aspnes *et al.* [8] give the following expression for the RAS intensity:

$$\frac{\Delta I}{\bar{I}} = 2\left(-\mathrm{Im}\frac{\Delta r}{\bar{r}} - 2a_p + \delta_1 \cos 2\theta_1 + \delta_2 \cos 2\theta_2\right) J_1(\delta_m)\sin\omega t + 2\left(\mathrm{Re}\frac{\Delta r}{\bar{r}} + 2\Delta P + 2\Delta M\right) J_2(\delta_m)\cos 2\omega t \tag{2.23}$$

The difference can be explained:

1) They refer θ_1 and θ_2 to 45° instead of 0° as we do here. By setting

$$\theta^{Aspnes} = \theta - 45°, \tag{2.24}$$

the window terms can be converted to

$$-\delta_1 \sin 2\theta_1 + \delta_2 \sin 2\theta_2 = -\delta_1 \cos 2\theta_1^{Aspnes} + \delta_2 \cos 2\theta_2^{Aspnes}. \tag{2.25}$$

2) The different signs are due to different definition of axes.

Higher order terms

Experience has shown that the first order approximation in the intensity calculation is acceptable with respect to describing the most important calibration errors, with perhaps one exception: The phase differences from window strain $\delta_1(\omega)$ and $\delta_2(\omega)$, give a background spectrum both in the real and the imaginary part of RAS measurements, although larger in the latter case. Further analysis has shown that the explanation is that the window strain terms appear in the second order terms of the real part of the RAS signal.

Measuring at higher harmonics

If higher order Bessel functions J_n from (2.17) are included in the expression for the intensity (2.18), one finds that it is possible to measure the real and imaginary part of the reflection anisotropy at higher harmonic frequencies. The imaginary part can be measured at odd harmonics ω_{PEM}, $3\omega_{PEM}$, $5\omega_{PEM}$, $7\omega_{PEM}$, ..., and the real part can be measured at even harmonics $2\omega_{PEM}$, $4\omega_{PEM}$, $6\omega_{PEM}$, $8\omega_{PEM}$, ... This is of increased interest because new electronic instruments (e.g. digital lock-in or fast analog-to-digital converters) are able to deal with several higher harmonics of the given frequency $2\pi\ \omega_{PEM}$ = 50 kHz *simultaneously*. From (2.17) and (2.18) it is seen that all even harmonics have the same prefactor, and the same is true for all odd harmonics. A spectrum of acceptable quality can thus be obtained faster by exploiting this feature. For example, measuring a time t_0 simultaneously at two harmonics with equal prefactors, will give a similar signal-to-noise ratio for the signal as a measurement at one harmonic a time $2 \cdot t_0$.

2.6 Azimuthal orientation of the sample

It is rather difficult to align the crystallographic axes of the sample to exactly ± 45°. Typically the error may be a few degrees. In this case the last approximation in (2.6) may not be valid, and by assuming that

$$r_{-45} \approx r_{45} \approx \bar{r} \ , \tag{2.26}$$

the Jones-matrix for the sample becomes

$$\begin{aligned} &= \begin{pmatrix} \bar{r}(\sin^2\gamma + \cos^2\gamma) & -\Delta r \sin\gamma\cos\gamma \\ -\Delta r \sin\gamma\cos\gamma & \bar{r}(\sin^2\gamma + \cos^2\gamma) \end{pmatrix} \\ &= \begin{pmatrix} \bar{r} & -(\sin 2\gamma)\dfrac{\Delta r}{2} \\ -(\sin 2\gamma)\dfrac{\Delta r}{2} & \bar{r} \end{pmatrix} . \end{aligned} \tag{2.27}$$

The rest of the calculation follows the same path as previously, and the RA intensity signal (2.20) takes the form

$$\begin{aligned} \frac{\Delta I}{\bar{I}} &= 2\left(-(\sin 2\gamma \,\mathrm{Im}\frac{\Delta r}{\bar{r}} - 2a_p - \delta_1 \sin 2\theta_1 + \delta_2 \sin 2\theta_2 \right) J_1(\delta_m)\sin\omega_{PEM} t \\ &+2\left(-(\sin 2\gamma)\,\mathrm{Re}\frac{\Delta r}{\bar{r}} - 2\Delta P - 2\Delta M \right) J_2(\delta_m)\cos 2\omega_{PEM} t \end{aligned} \ . \tag{2.28}$$

The resulting variation in the signal as a function of the azimuthal orientation follows a sinusoidal curve. Maximum values appear at –45° and 45°, and at 0° the pre-factor is zero. Rotating the sample 90° has the consequence that the RA signal changes sign. For small deviation $\Delta\gamma$ from 45° we obtain

$$\sin(2\gamma) \approx 1 - 2(\Delta\gamma)^2 , \tag{2.29}$$

and the misalignment is therefore a second order effect. For example, if the sample is oriented 5° away the optimal position, the resulting signal will be reduced to 98% of the actual value. Consequently, in a typical experiment, a small error in the azimuthal orientation is not crucial to the overall result.

2.7 Sample imperfections

Another potential error source is the effect of a partially damaged surface on the RAS signal. Scratches and damaged areas may arise as a consequence of imperfect polishing or handling the sample between polishing and measuring. The resulting contribution to the RAS signal may be divided into two categories:

i) Geometric: A corrugate surface scatters the light more than a smooth surface. If the outcome is an anisotropic reflection, it will influence the RAS signal. However, one would not expect this effect to depend on the wavelength in the optical wavelength band, and the net result will be an offset from zero for the complete spectrum.

ii) Microscopic: a defect may have destroyed the ideal arrangements of atoms in the lattice over a rather large area of the sample. As long as the aberrations are statistical, they will not contribute to the signal. Nevertheless, defects of this type can reduce the strength of the RAS signal, because the resulting statistically disordered area will have a RAS close to zero, while the reflected intensity might not be significantly reduced. For example, if 20% of the total sample area is damaged, then the RAS signal will be reduced by up to 20%.

It is generally difficult to attribute an offset in the RA spectrum to either the instrument or the sample. Therefore, signal offsets are often set to zero by instrument calibration. In conclusion, minor damaged areas of the sample will therefore most often not introduce significant errors to the RA spectra.

2.8 Polarisation dependency of the detector

It is known from other measurement techniques that detectors can have a polarisation dependency. If there are two principal axes at an angle α to the x-axis, where the electrical field is detected with factors 1-D_1 and 1-D_2, respectively, we must introduce an additional Jones-matrix in (2.11):

$$J_{Detector} = R(-\alpha)\begin{pmatrix} 1-D_1 & 0 \\ 0 & 1-D_2 \end{pmatrix} R(\alpha) \tag{2.30}$$

However, to first order as in (2.13) and (2.16), the intensity is given by only the first component of the electrical field, E_1. Therefore, in this case there is no net result on the RAS signal from polarisation dependent detectors.

2.9 Frequency dependency

In RAS, one measures the reflection anisotropy (2.20) as a function of frequency ω. Suppose that a finite frequency band $\Delta\omega$ passes the monochromator at a given setting of the monochromator. The measured value can be expressed as an integral,

$$\mathrm{Re}\frac{\Delta r}{r}(\omega)=\int_{-\infty}^{\infty}A(\omega-\omega_0)\,\mathrm{Re}\frac{\Delta r}{r}(\omega_0)\,\mathrm{d}\omega_0\ , \tag{2.31}$$

where the throughput function A depends on the monochromator (and its input and output slit) used in the experiment. The spectrum for a sample measured by different set-ups will therefore be different with respect to strengths and widths of peaks. This is important to have in mind when comparing spectra, for example when comparing the spectra of Ag(110) (see Section 5.1 and 5.2). In that case the strength of the main double resonance in the RA spectrum is highly dependent on the fast-varying intensity in the same region. Consequently, different throughput functions will give very different strength of the resonance.

2.10 Kramers-Kronig relations

From causal connection between polarisation and the electric field one can derive a pair of integrals relating the real and imaginary part of the reflection anisotropy [9],

$$\mathrm{Im}\frac{\Delta r}{r}(\omega)=-\frac{1}{\pi}\int_{-\infty}^{\infty}\mathrm{d}\beta\,\frac{\mathrm{Re}\frac{\Delta r}{r}(\beta)}{\beta-\omega}\ , \tag{2.32}$$

$$\mathrm{Re}\frac{\Delta r}{r}(\omega)=\frac{1}{\pi}\int_{-\infty}^{\infty}\mathrm{d}\beta\,\frac{\mathrm{Im}\frac{\Delta r}{r}(\beta)}{\beta-\omega}\ . \tag{2.33}$$

These Kramers-Kronig relations can be used to calculate the real part of the reflection anisotropy from the imaginary part and vice versa. In addition, if both the real and imaginary part is known, (2.32) and (2.33) can be used to validate the spectra, calculate background spectra or establish the correct zero-level of the spectra.

If the integrals (2.32) and (2.33) exist, both the real part and imaginary part will approach zero when the frequency ω gets sufficiently close to infinity. Therefore, the reflection anisotropy spectra should reach zero at both 'ends' when scanning a large enough wavelength window. This property can sometimes be used to remove offset errors from experimental spectra (see Section 3.8).

3 Instrumentation and measurement procedures

The constructed instrument consists of four separate parts: the reflection anisotropy spectroscopy optics, the ultrahigh vacuum (UHV) system, the signal processing electronics, and system control software (RASLab). The relation between them is schematically drawn in Figure 3.1. Most parts of the equipment is designed and built on-site, with the help of mechanical and electronic workshops.

3.1 RAS systems

Three different realisations of RAS systems have been constructed:

The main RAS system: This is of the type schematically shown in Figure 2.3. It has a dedicated UHV system for in-situ measurements of prepared samples. The main RAS system has been used for most of the measurements presented in this thesis. The available energy range is 1.0 – 6.0 eV.

The mobile RAS system: This system is also of the type schematically shown in Figure 2.3, and it is a supplement at a UHV system dedicated to STM measurements. The design is more compact; with all the optics taking no more space than 40x 30x10 cm. Electronic components

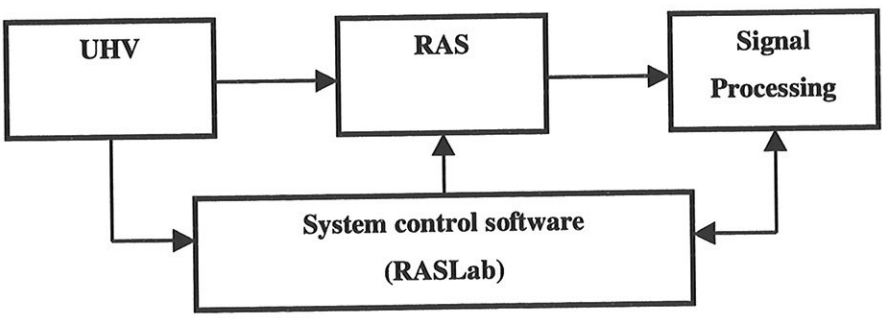

Figure 3.1. Schematic RAS measurement set-up.

are placed in a mobile rack, and with optics mounted on a flexible arm connected to the rack, the system is easy to position with respect to the sample. The compact design with only two mirrors results in lower intensity throughput and less energy resolution than the main set-up. However, measurements of acceptable quality can still be performed in most cases [10]. The effective energy range for measurements is 1.5 - 5.5 eV.

The Wollaston RAS system: This system differs from the two above in that it uses a Wollaston-prism and a rotating (~100 – 400 Hz) chopper as analysing elements instead of photoelastic modulator and analyser. In addition, it uses lenses instead of mirrors, and the monochromator is positioned just after the light source. The Wollaston prism divides the light into two orthogonally polarised beams, and the chopper blocks each beam in turn. Both beams are focused on the detector, and a lock-in amplifier detects the modulation of the incoming light. Electronic circuits were developed to ensure that the rays got equal amount of time on the detector. However, thorough calibration, fine-tuning and testing did not make the quality of the measured spectra comparable to the main RAS system [11].

The rest of this chapter is mainly devoted to the main RAS system.

3.2 Optical set-up

When constructing the optics our main goal was to increase the signal to noise ratio by getting as much light through the system as possible. We wanted to realise the principal set-up shown in Figure 2.3, and combine it with the self-designed UHV system. Several constraining factors existed, for example:

- The size of the sample (standard diameter Ø=10 mm).
- The aperture of polariser (diameter Ø=10 mm chosen for economical reasons).
- The aperture of the photoelastic modulator (diameter Ø=10).
- The size of the UHV window and the window flange.
- No elements (mirrors, etc.) between polariser and PEM, to avoid a possible change in polarisation of the beam.
- It was important to be close to normal incidence, therefore the physical size of the holders for the polariser and PEM were constrained.
- The relative aperture of the monochromator (f/4).

The final selected set-up is shown schematically in Figure 3.2.

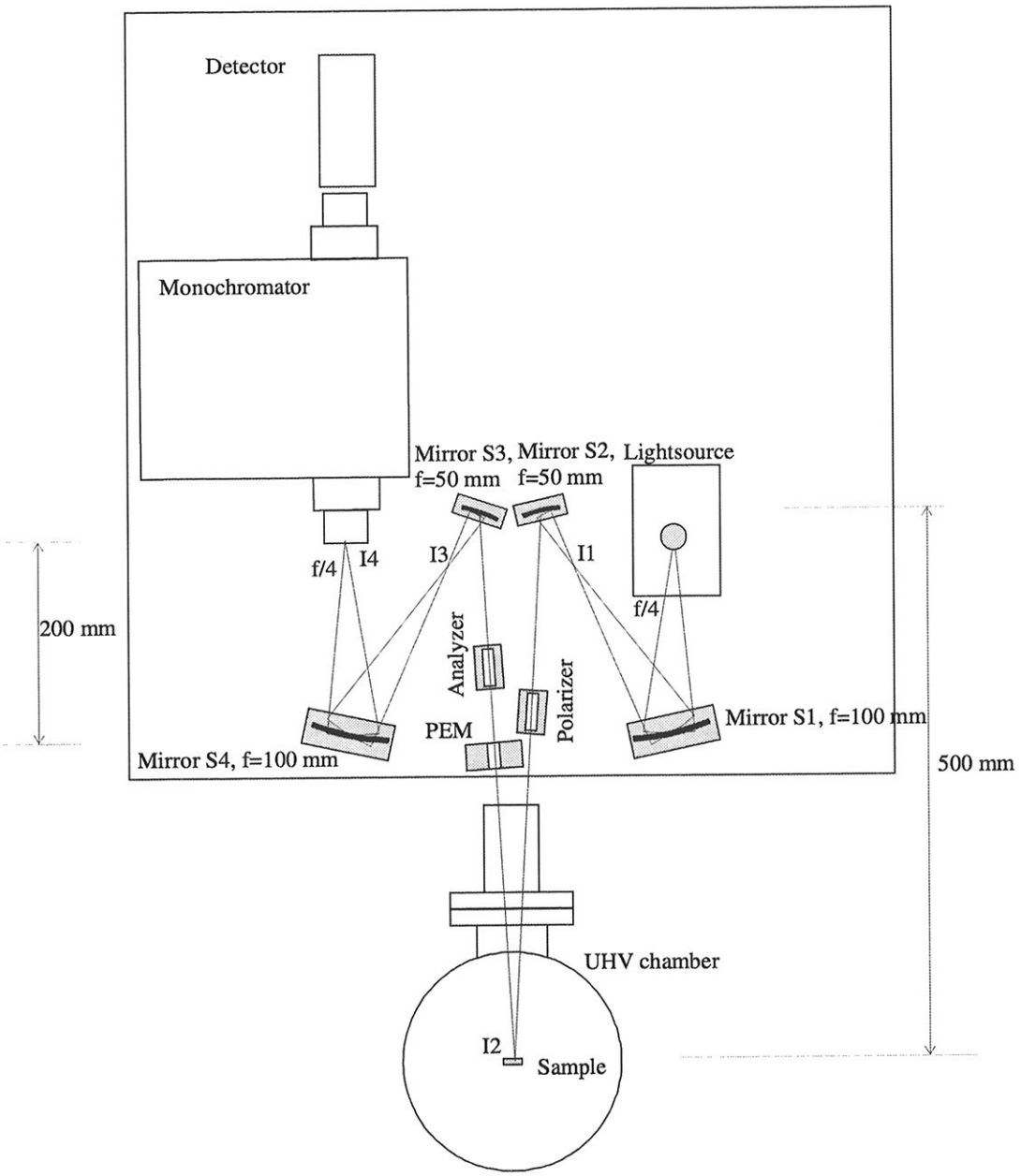

Figure 3.2 The schematics of the main RAS system set-up. I1-I4 are the positions of images of the light-source and S1-S4 are mirrors.

Optical table

The optical components are placed on at a 70x70 cm table. The four table legs were made height adjustable. Due to lack of space the optical table had to be situated close to the UHV window.

Light-source

Two different types of light-source are used: a xenon arc lamp and a halogen projector lamp. The xenon arc lamp is positioned in a custom made lamp housing with special care taken to avoid short-circuits when the lamp is ignited. A pipe and a fan are connected to the back of the lamp housing to cool the lamp and to remove any ozone produced by the UV radiation. We use a 150 W arc lamp with a spot size 0.5 x 2.5 mm. Most of the intensity (> 60%) is radiated from the part closest to the anode (upper part) of size 0.5x0.5 mm, and this is the area we imaged to the sample surface, and subsequently to the detector.

The spectral irradiance for the xenon arc lamp is shown in Figure 3.3. The output from the arc lamp covers wavelengths from 200 nm to infrared, and it is therefore well suited for our near-infrared, visible and ultra-violet RAS measurements.

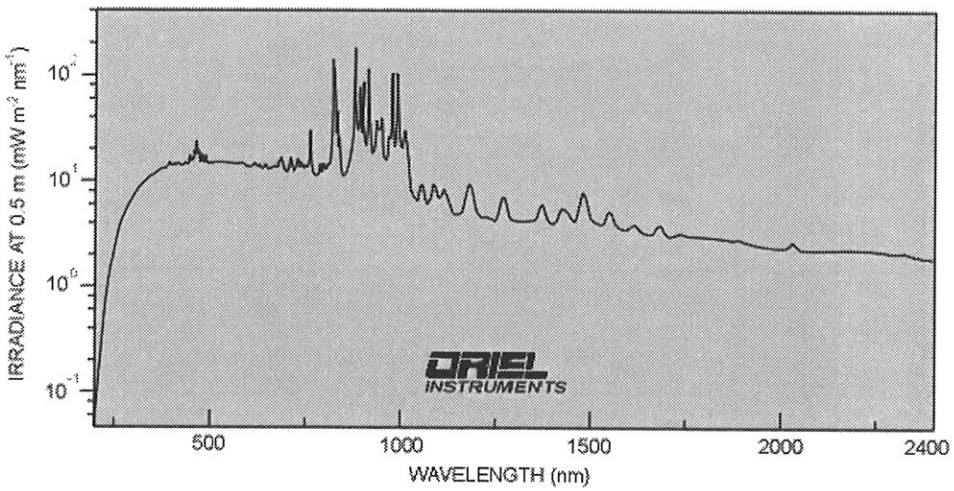

Figure 3.3. Spectral irradiance for the xenon 150 W arc lamp. Data from Oriel Instruments (www.oriel.com).

A special power supply is needed to use the xenon arc lamp, because the arc needs to be ignited with a voltage pulse of about 25 kV. After the lamp has started, the 150 W lamp runs on 20 V DC. The ignition poses problem to the design of the system, because the electromagnetic field induces voltage spikes on nearby electronic wires. A couple of times this has lead to minor damages on other electronic parts in the RAS system.

The nominal effect of the halogen projector lamp is 100 W. The filament size is considerably larger than the xenon arc spot, about 4x5 mm. Only a small part of the filament (0.5x0.5 mm) is actually imaged on the sample surface, and the intensity throughput is therefore substantially lower. The lamp radiates energy in the range from about 330 nm to infrared. The projector lamp uses only a standard 12 V (10 A) power supply, with no special ignition voltage.

Mirrors

The mirrors are made of glass coated with aluminium. The glass was polished and prepared by a spectacle lens manufacturer (Essilor, Oslo). The positioning of mirrors was mainly

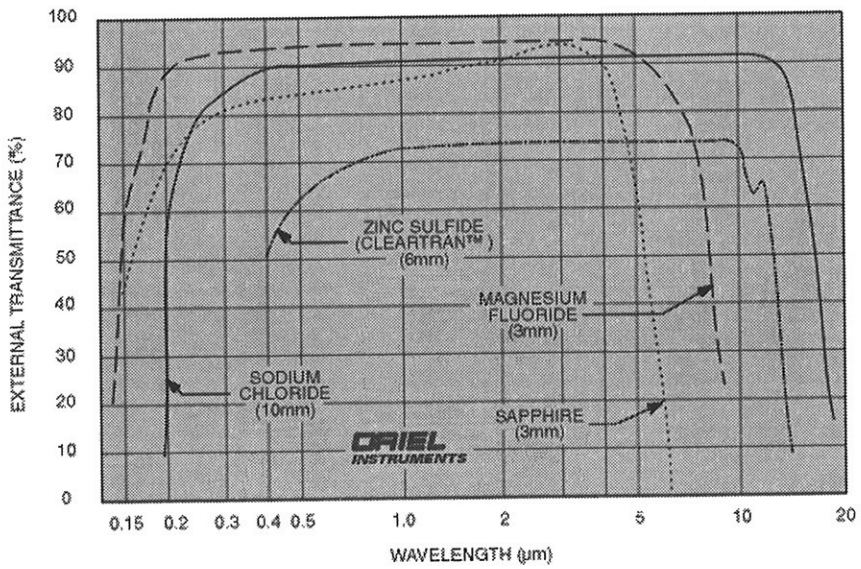

Figure 3.4. External transmittance of UV-IR optical materials (From Oriel Instruments, www.oriel.com).

determined by two factors: i) the relative aperture of the monochromator (f/4) and ii) the Ø10 mm aperture of the polariser and PEM. The latter was important because the minimum distance between these components and the sample were approximately 30 cm, giving a relative aperture of f/30. A symmetrical set-up with respect to the surface normal of the sample was selected.

Mirror S1 and S4 was positioned 20 cm from the light-source and monochromator, respectively. These positions are a trade-off between being as close as possible to the light source (to reduce the size of the mirror while keeping the relative aperture equal to f/4), and keeping the incidence angle at the mirror reasonable small (to prevent aberration).

To get as much as possible of the light-beam through the polariser, we chose to use a second mirror (S2) between the S1 and the sample surface, to effectively reduce the size of the beam. The chosen combination have a focal length $f = 100$ mm of mirror S1, a focal length $f = 50$ mm of mirror S2, and mirror S2 positioned 55 mm from image I1. This set-up gives a beam-diameter of 12.5 mm on S2 and a distance from S2 to image I2 on the sample surface of 500 mm. From these numbers we can find the beam diameter at the polariser,

$$D_{beam} = \frac{(500-200)}{500} 12.5 \text{ mm} = 7.5 \text{ mm}, \tag{3.1}$$

which is well below the aperture of the polariser. This is calculated for the beam from the on-axis focal point. Off-axis parts of the spot will increase the diameter of the light beam. However, the size of the spot is small, so the difference is not substantial.

The magnification between the light source and image I1 is η=200/200=1, while the magnification from I1 to I2 is η=500/55≈9. A light-source spot of 0.5x0.5 mm will therefore ideally create an image on the sample of size 4.5x4.5 mm, which is well below the typical sample diameter of 10 mm.

The mirrors S3 and S4 have the same specification as S2 and S1, respectively. Because of the symmetrical positioning of the mirrors, the magnification of the image I4 on the monochromator with respect to the light-source is η=1. The mirror S4 was included in the set-up mainly because positioning the monochromator input slit at image I3 was difficult.

Because the four mirrors S1-S4 each reflects a light ray with incidence angle significantly different from zero, the image I4 has considerable astigmatism (the third Seidel aberration). The monochromator has a vertical input slit, and therefore we use the tangential focus (a vertical line) as the image at the input slit. This is actually an advantage, since the extraordinary ray from the analyser creates an image close to the ordinary ray image, but shifted horizontally. This means that the tangential focus makes it possible to separate the images and only let the ordinary ray get through the monochromator. Of course, it is also possible to block the extraordinary ray at I3.

Polariser and analyser

The polariser and analyser are of the Rochon type, made by Bernard Halle Nachfl. GmBH, and have an aperture of Ø=10 mm. The prisms are made of magnesium fluoride (MgF_2), which has excellent UV transmission, as illustrated in Figure 3.4. The transmittance in the infrared is poor above 100 nm, constraining to the overall intensity throughput of the system in this energy range. The incoming ray is divided into two outgoing rays of different polarisation (ordinary and extraordinary ray). The extraordinary ray is offset by a small angle of typically 2.24° at 400 nm. It is important not to let this ray propagate through the optical system. Therefore, the extraordinary ray from the polariser is blocked by the photoelastic modulator and the extraordinary ray from the analyser is blocked at the input slit of the monochromator.

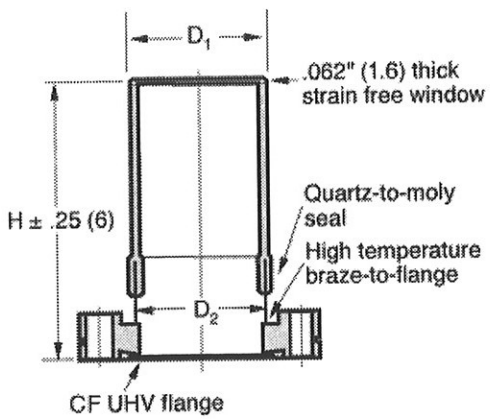

Figure 3.5. The Bomco low-strain window (www.bomco.com).

Both the polariser and the analyser are placed in a custom made rotatable holder, where the polarisation angle can be adjusted very accurately (0.01°) either by hand or by a computer-controlled stepmotor. The holders are small to allow a close to normal incidence angle at the sample.

Low-strain UHV window

In a traditional window inhomogeneous strain introduces variable optical phase shifts both with respect to position on the window and with respect to polarisation of the incoming photons. This introduces a large background in the reflection anisotropy spectra. To minimise the effect a special low-strain window is used (see Figure 3.5), made by fusing a thick synthetic quartz disc to a quartz tube, which in turn is fused to a quartz-to-molybdenum seal that is brazed to the UHV flange. Bomco, Inc. manufactured the low-strain windows.

Photoelastic modulator

To simplify the detection of the reflection difference the signal is modulated by a photoelastic modulator. Figure 3.6 shows the schematic set-up of the Beaglehole PEM used in our measurements. A controlled sinusoidal strain is applied to a fused quarts block to produce an oscillating phase velocity along one axis at a frequency close to an acoustic resonance of quartz. Standing waves at the resonance frequency of 50 kHz arise in the quartz block. The strain is produced by a piezoelectric transducer made of crystal quartz glued to one face of the fused quarts block. By using the same material for transducer and optical element, both components have the same resonance frequency and can be weakly bounded at a wave node that is almost strain free. In addition, a second quartz crystal piezoelectric transducer "gauge"

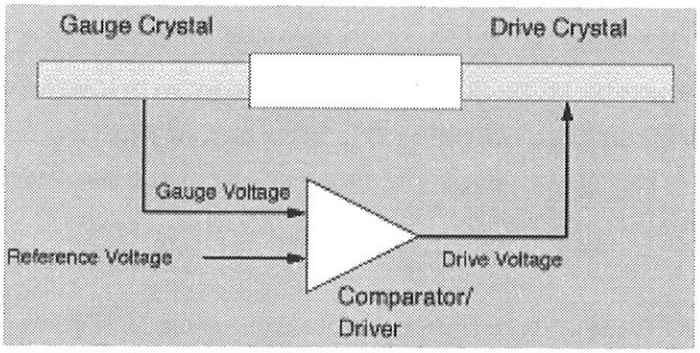

Figure 3.6. Principal sketch of the Beaglehole Instruments PEM (From www.beaglehole.com).

of the same size is mounted on the opposite face of the fused quarts block to monitor the peak phase retardation.

The change in refraction is a linear function of the strain, which, in turn, is a sinusoidal function of time. Thus the relative phase difference between the two orthogonal directions of the PEM is

$$\delta = \left(\frac{2\pi d}{\lambda}\right) P(V, C) \sin \omega t \ , \tag{3.2}$$

where λ is the wavelength, d is the thickness of the block, and P is proportional to the strain amplitude. For the Beaglehole PEM, P depends on the amplitude of the voltage V applied and the capacitance C of the gauge circuit. In general, different wavelengths require different voltages to obtain the same phase difference of the PEM. In RAS measurements one typically uses the same phase shift for every wavelength, for example corresponding to a maximum of the Bessel functions J_1 and J_2 in the expression for the RAS signal, see (2.20). Therefore, the applied voltage is varied with respect to the wavelength, according to calibrated values.

An electronic drive unit controls the PEM. Voltage it applied to the strain-generating quartz crystal, and the gauge signal is maintained constant by a high-gain electronic feedback circuit to the drive voltage. The desired rms-value for the gauss voltage is set from the system control software. In addition, a buffered version of the actual gauge voltage is available as a reference for the lock-in amplifier (see below).

The voltage that can be applied to the crystal is in a limited range, which for the Beaglehole PEM is 0-200 V (rms). Therefore, for increasing wavelengths, the maximum available phase shift decreases. If we increase the capacitance, this maximum will increase, thus allowing measurements at larger wavelengths. The capacitance can be varied by inserting an extra capacitor in parallel at the gauge side of the PEM. In our case, we found that an extra capacitance of about 800 pF was optimal with respect to energy range and desired peak phase retardations.

The aperture of the PEM is a 10 mm circle around the centre of the fused quarts block. The birefringence is caused by a standing wave that varies as $\cos(2x/L)$ along the element, with L the element length and x measured from centre. Therefore, the shift in phase over the disk is within 2% of the centre value.

The PEM is positioned at the same distance from the sample as the polariser (see Figure 3.2). The aperture of these elements are identical, and due to the symmetric set-up it is clear that most part of light ray hitting the PEM will pass through the PEM.

Monochromator

In principle, the monochromator could be placed anywhere in the set-up between the light source and the photodetector. In our RAS set-up, the monochromator is located just before the detector. The advantages of this position are

i) It is easier to align the optical components because the complete spectrum of light is available.

ii) The noise from stray light at the detector is reduced compared to having the monochromator elsewhere in the set-up.

Two types of monochromators are used in the main RAS system. In the energy range 1.7-6.0 eV (visible and UV), the system is equipped with an ISA Jobin-Yvon H.25 monochromator with a single grating (1200 groves per mm). The half intensity bandwidth (HIBW) of the wavelength of photons at the output slit is typically 5-15 nm in our measurements.

In the energy range 1.0-2.5 eV a Schoeffel QPM 30 quartz prism monochromator. The input of this monochromator should exist of parallel rays, and this was accomplished by moving mirror S4 in Figure 3.2 closer to mirror S3 until the image I3 is at the focal point of S4. The rays will then be parallel at the monochromator. In our measurements, HIBW for this monochromator is 5-50 nm.

The wavelength adjustment is controlled by a stepmotor connected to the control software. An automatic RAS measurement consists of stepping the motor so that the wavelength varies.

Detector

A custom made Si pin-diode photo-detector from EMM in Germany is mounted on the output slit of the monochromator. Intensity in the wavelength range 200-1100 nm is converted to a voltage, which is then amplified to a readable output of 0-8V. The detector and its amplifier has a usable frequency range of 0 - 150 kHz. Light intensity as low as 1 nW is measurable

(1 pW if used in combination with a lock-in amplifier). The diameter of the detecting diode is 4 mm.

3.3 Intensity throughput

The intensity throughput of the complete RAS system depends on the reflectivity properties of the sample. Figure 3.7 shows the throughput function for three samples Si(100), Au(100) and Cu(780). The signal is measured before amplification by the external amplifier. The Au and Cu samples were inside the vacuum chamber at the time of the measurement, while the Si spectra was measured in air. When the sample is positioned in the vacuum, the intensity throughput is generally lower because of the window. In addition, it is generally more difficult to align the optics in an optimal position when the sample is in the chamber. It is seen from the figure that above 5 eV the unamplified signal is very low, while at the other end of the spectrum, close to 1.5 eV, the throughput is still good.

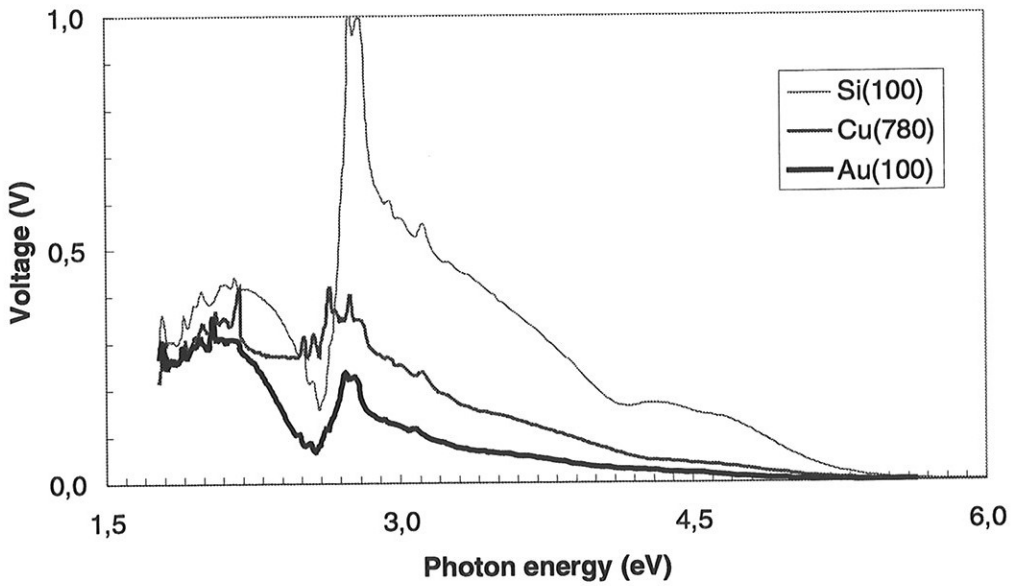

Figure 3.7 Unamplified intensity throughput spectra for three different samples: Si(100) (thin line), Cu(780) (medium line) and Au(100) thick line. The Cu and Au samples were measured in the UHV chamber.

3.4 Improvement of the electronic signal

The set-up of electronic components is illustrated in Figure 3.8. A closer description of each part is given below.

Amplifier

The amplifier module consists of three separate amplifiers with amplification F=2x, F=5x and F=10x respectively. Each of them can be controlled separately, giving a total of eight possible signal amplificatio settings (1, 2, 5, 10 (5x and 2x, or 10x), 20, 50, 100). The system control software via TTL logic on the ADC card controls the state of each amplifier, thereby making it possible to optimise the amplification and measurement at each measured wavelength.

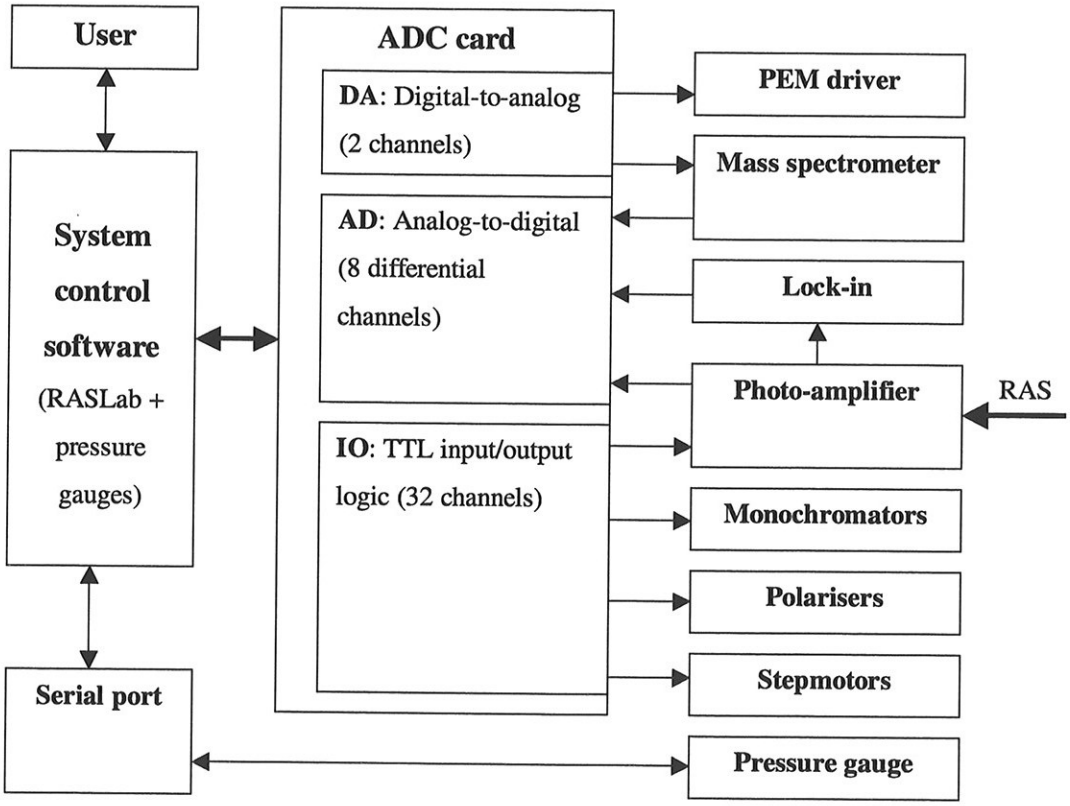

Figure 3.8. The set-up of electronic components in the RAS system

The white noise level at F=1 is about 5 mV peak-to-peak. A more serious problem is the offset errors of each of the three amplifiers, which leads to different offset errors for each of the eight amplification levels. A table of values in the system control software corrects this.

There are two outputs from the amplifier: i) a DC-output corresponding to the amplified intensity, and ii) an AC-output, with 50 kHz and 100 kHz components corresponding to the first and second term of (2.20), respectively. In general, a complete spectrum of noise at other frequencies degrade the AC component, so to get the rms voltage of the n·50 kHz components the signal is fed through a lock-in amplifier.

Lock-in amplifier

In the lock-in amplifier, the AC part of the signal is amplified, multiplied with the reference and then a low-pass filter is applied. Assuming that the noise-free signal is $A(\omega_0)$, the total signal S can be written as a Fourier integral,

$$S(t) = \int_0^\infty (A(\omega)\cos\omega t + B(\omega)\sin\omega t)\,\mathrm{d}\omega\,. \tag{3.3}$$

We multiply S by the reference signal of frequency ω_0 with a phase φ, and averages from time $t=t_0-\Delta$ to $t=t_0+\Delta$. The signal S_L at the lock-in output is then

$$\begin{aligned} S_L(\omega,t_0,\Delta) &= \int_{t_0-\Delta}^{t_0+\Delta} \frac{1}{2\Delta}\cos(\omega_0 t+\varphi)\int_0^\infty (A(\omega)\cos\omega t + B(\omega)\sin\omega t)\,\mathrm{d}\omega\,\mathrm{d}t \\ &= \int_0^\infty (A(\omega)\int_{t_0-\Delta}^{t_0+\Delta}\frac{1}{2\Delta}\cos(\omega_0 t+\varphi)\cos\omega t\,\mathrm{d}t + B(\omega)\int_{t_0-\Delta}^{t_0+\Delta}\frac{1}{2\Delta}\cos(\omega_0 t+\varphi)\sin\omega t\,\mathrm{d}t)\,\mathrm{d}\omega \end{aligned} \tag{3.4}$$

As the low-pass time constant Δ increases, the inner integrals goes rapidly towards zero for all frequencies not equal to the reference frequency ($\omega\neq\omega_0$),

$$S_L(\omega,t_0,\Delta)\xrightarrow[\Delta\to\infty]{} \frac{1}{2}(A(\omega_0)\cos\varphi - B(\omega_0)\sin\varphi)\,. \tag{3.5}$$

The lock-in therefore picks out the frequency component $A(\omega_0)$ of the signal $S(t)$ corresponding to the reference frequency, the gauge monitor signal from the PEM. Electronic components, for example the detector, introduce a phase shift φ in the signal with respect to the reference, and this can be compensated for in the lock-in. By multiplying the reference frequency with a number n, the lock-in is able to output the n'th harmonic part of the signal ($n\cdot\omega_0$).

Most of the spectra presented in this thesis are measured with the use of Princeton Applied Research Lock-in model 124A, while an EG&G model 7265 DSP lock-in amplifier is used in the most recent measurements. The latter digitises the signal before the multiplication with the (digitised) reference, and the signal-to-noise ratio is therefore improved.

Analog-to-digital converter

The output of the lock-in is fed into an analog-to-digital converter (ADC) card. The ADC is a Computerboards CIO-DAS1602 with an input range from –10 V to 10 V and a resolution of 16 bits. As shown in Figure 3.8, there are 8 differential input channels so that both the DC intensity from the amplifier and the signal from the lock in can be measured simultaneously. In addition, the ADC has two analog outputs, and one of those is used to software control the gauge voltage of the photoelastic modulator.

Special care had to be taken to ensure that each input channel of the ADC is independent of the others:

1. A special designed cable with extra screening was used to connect the AD to the lock-in and photoamplifier.
2. The ADC board uses two multiplexers (MUX), and the two input channels in concurrent use have been connected to separate MUX's.
3. The ADC input buffers are cleared by reading them five times before values are used.

The ADC also has several TTL outputs which is used to control stepmotors (monochromator, polariser) and the amplification of the amplifier.

3.5 Ultra-high vacuum system

In order to perform RAS on clean surfaces, it is necessary to clean and measure the samples in ultra high vacuum. We have built a dedicated UHV chamber for RAS measurements, with the additional future possibilities to do infrared ellipsometry and the '45 degrees'-technique [12]. A photo of the chamber together with the main RAS system is shown in Figure 3.9. Following is a brief description of the UHV system while details such as brand and model of some of the components are given in Appendix B.

The 20 l chamber is equipped with three **vacuum pumping units** suitable for different pressure ranges. The turbomolecular pump operates at all pressures, and has capacity to reach a pressure level of $2 \cdot 10^{-10}$ mbar on its own. The ion pump is used in the pressure range 10^{-6} - 10^{-11} mbar as a supplement to the turbomolecular pump. The titanium-sublimation pump (TSP) is used only rarely and only at low pressures (10^{-9} - 10^{-11} mbar), to reduce the pressure to below $1 \cdot 10^{-10}$ mbar for a limited time, for example during a measurement.

The **mass spectrometer** is used to check for leaks and impurities in the chamber. It is possible to search manually for different gas remnants, or use the system control software to

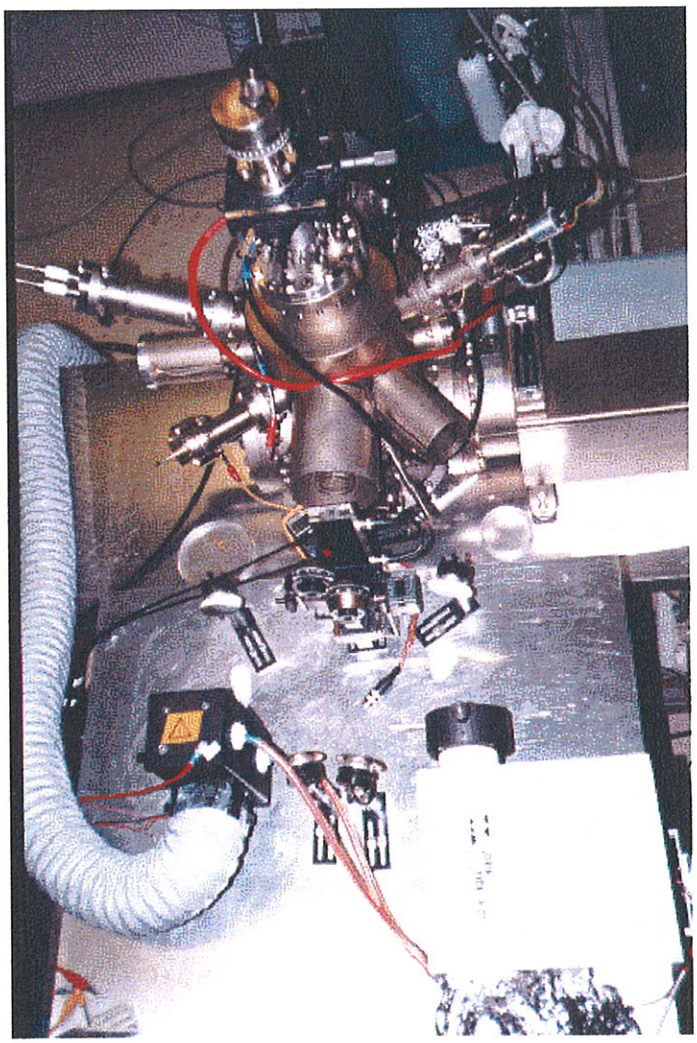

Figure 3.9. The UHV chamber and the main RAS set-up.

scan the range from 0 to 80 mass units.

Three different **manometers** measure the pressure level in the chamber. An ionisation gauge is mounted in the chamber to be used in the range 10^{-4} - 10^{-12} mbar. A Pirani gauge measures pressures in the range 10^{+3} - 10^{-4} mbar. In addition, a thermocouple-based manometer is connected to the outlet of the turbo-molecular pump, to indicate pressure levels from 10^{+3} -

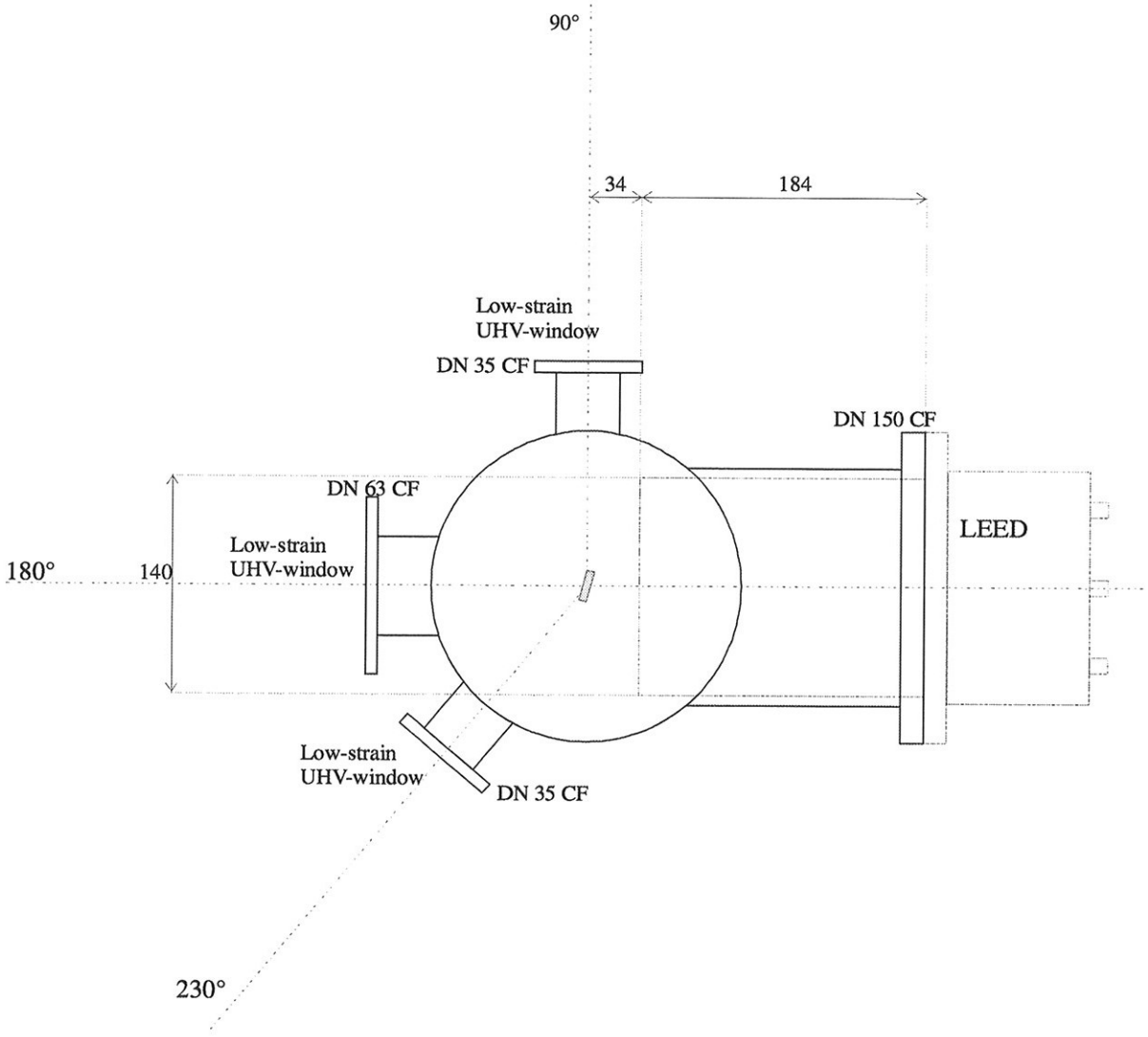

Figure 3.10. Cross section at the RAS level of the UHV chamber (reduced scale, lengths in mm).

10^{-3} mbar.

The sample is mounted on a **manipulator arm** that can translate the sample 50 mm in the vertical direction and 25 mm in both orthogonal horizontal directions. It is possible to rotate the sample both azimuthally and around its vertical axis (see Figure 3.14).

A horizontal cross-section of the UHV chamber in the plane of the incoming and outgoing RAS beams is drawn in Figure 3.10. In this plane, one large and two small **low-strain windows** allows for RAS measurements through three different ports. In some cases this feature has helped to determine the background in the RA spectra. However, the largest window is mostly used, because the alignment of the sample with respect to the RAS is easiest there. The angles between the windows make the chamber suitable also for standard ellipsometry (140°) and the 45 degrees technique (90°). The ion gun for sputtering, the LEED, the epitaxy cell and the temperature monitoring and heating system are situated with focus close to the centre of this horizontal plane. Therefore, complete cleaning cycles and measurements can be performed without any additional movements of the sample than a rather simple in-plane rotation with the manipulator arm. This is a big advantage, and is preventing a lot of problems related to translation and refocusing of the sample. In addition, several operations can be performed at the same time, for example sputtering and heating, sputtering and RAS, heating and RAS, and heating and LEED.

The **ion gun** used for sputtering is situated at an angle 30 degrees with respect to the horizontal plane shown in Figure 3.10. A high purity (99.9999%) argon gas source is connected to the ion gun, and the ion bombardment takes place with an argon pressure of 10^{-5} mbar in the chamber. The kinetic energy of the sputtering ions is 500 eV.

Heating the sample is accomplished by the design of the sample-holder (see Figure 3.14). This particular set-up has allowed us to reach sample temperatures of 1000 K without any problems. The sample is mounted in a bent tungsten wire (0.75 mm), and current is sent through the wire and the sample from a high-current power supply. The temperature is monitored by a **thermocouple** glued into a drilled hole in the sample.

The chamber is equipped with a front-view low-energy electron diffraction unit (**LEED**). The surface is positioned at the focus of the electron beam, and the reflected electrons form a diffraction pattern at a fluorescent screen.

To carry out metal-on-metal growth an **epitaxial cell** is connected to the chamber. It is positioned above the low-strain window at 90° (see Figure 3.10), in a 30° degrees angle to the horizontal plane, and RAS measurements of the growth can therefore be performed. A high-current power supply is attached to the cell, and cooling is accomplished by circulation of water.

Several leak-valve **gas inlets** are available for the study of for example catalytic reactions. These include high purity (>99.999 %) sources for nitrogen, xenon, carbon monoxide, and oxygen.

3.6 System control software

Apart from two separate programs connected to the manometers and the mass spectrometer, the main software program, RASLab, controls all the electronic and optical components. The control paths are shown in Figure 3.8. RASLab, currently in version 3, has an object-oriented design, where each connected instrument (ADC, PEM, lock-in, polariser, photo-amplifier, etc.) or measurement is completely encapsulated by a C++ class. This makes it easy to change the type of an instrument, for example to exchange monochromators. Each instrument can be controlled, read or calibrated by selecting the appropriate menu item. In addition, an options page represents each instrument, where detailed settings for the instrument can be adjusted.

Every measurement creates an instance of the data-set class. Data sets can be saved to and loaded from disk, viewed and edited, filtered and cleared, and plotted to the screen or to the printer. All the parameters for the measurement are in the data-set, including date and time, all instrument settings, and for every recorded data point the photon energy, RA signal, lock-in signal, intensity, standard deviation and amplification. The contents are similar to the content in the measurement log-file printed in Appendix C.

The main program window is captured in Figure 3.11. Several data-sets can be displayed at the same time, thus making comparison between measurements possible. In this case, the single peak RAS Ag(110) spectrum is compared to the double peak RAS of Ag(110). It is possible to choose between several recorded parameters to be displayed. In Figure 3.11 the view includes the RAS signal, amplified intensity, standard deviation and amplification.

From the measurement menu it is possible to start an automatic RAS versus energy measurement. The window for selecting spectrum parameters is shown in Figure 3.12. These include start and end wavelengths, wavelength step, number of samples per wavelength to

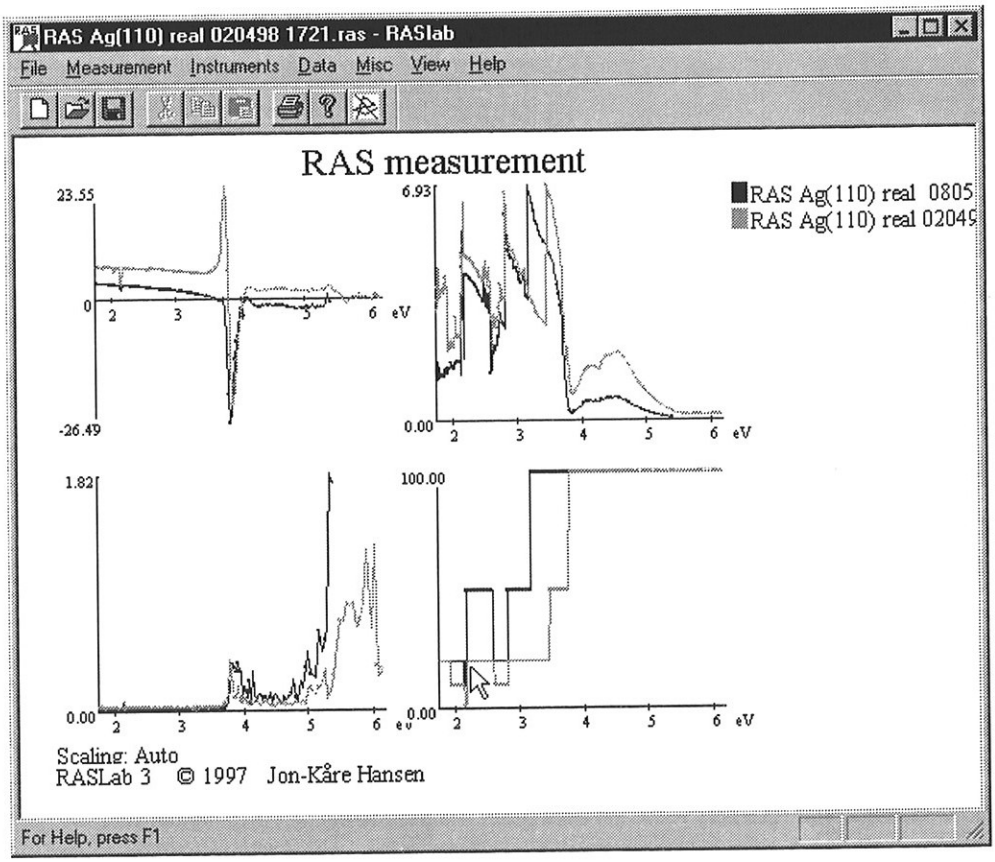

Figure 3.11. The RASLab software: main window in multispectra view for two different Ag(110) spectra. RAS spectrum (top left), amplified intensity (top right), standard deviation (bottom left) and photoamplifier amplification (bottom right).

average, number of complete spectrum scans, lock-in sensitivity, PEM phase, and real or imaginary parts of the spectrum. During the measurement, the software automatically adjusts the amplification of the photoamplifiers, so that the inputs from lock-in and the photoamplifier are in the optimal range, if possible. The measurement are saved to a log-file of the type illustrated in Appendix C, and in a binary data file. The date and time of the measurement is automatically added to the selected file name.

It is also possible with the software to do time-dependent measurements at one particular wavelength, and adjustable parameters in this case include the wavelength, time resolution, maximum time, lock-in sensitivity, PEM phase, and real or imaginary parts of the spectrum.

3.7 Noise

A throughout treatment of noise-related errors in RAS measurements is given elsewhere [13].

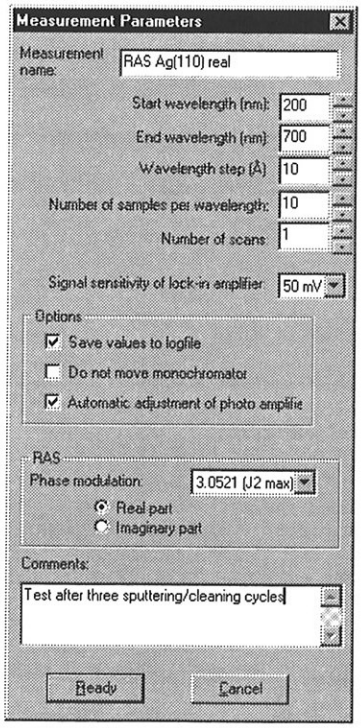

Figure 3.12. Setting the starting parameters of an RAS vs. energy measurement in RASLab.

Only a brief discussion is given here.

The difference between the measured RAS signal $(\Delta r/r)_M$ and the real RAS signal $(\Delta r/r)_{RAS}$ is due to systematic calibration errors ε_{CAL} and random noise ε_N, that is

$$\left(\frac{\Delta r}{r}\right)_M = \left(\frac{\Delta r}{r}\right)_{RAS} + \varepsilon_{CAL} + \varepsilon_N . \tag{3.6}$$

The calibration errors includes:

- UHV-window background spectrum.
- PEM voltage calibration errors.
- Photoamplifier offsets.
- Lock-in phase error.
- Error in value of step-length of stepmotors connected to monochromator and polariser.
- Incorrect polariser and analyser polar angle.
- ADC offset errors.
- Azimuthal sample alignment is not correct with respect to the polariser.

The last of these errors is discussed in Section 2.6. The other errors can be significantly reduced by tuning and calibrating the instrument, as explained in Section 3.3, Section 3.4 and Section 3.8, and/or corrected in software. Software correction is used for analog to digital conversion offsets and photoamplifier offset where a table of correction values are used.

The random noise errors includes:

- High frequency noise of xenon lamp.
- Mechanical vibrations of low-strain windows.
- Transients in the grounding circuit.
- Dark current of photodetector.
- Bit resolution errors of the analog-to-digital conversion.

The latter two is the most important sources for random noise at our set-up.

At each wavelength, the software asks for both the lock-in voltage and DC-voltage of the photoamplifier from the ADC card. The ADC software object returns a voltage that is an average of several readings (the number of primary AD readings, set by calibration, typically 5-10). The RAS signal $(\Delta r/r)_i$ is formed by dividing the lock-in voltage by the DC-voltage. This is repeated n times, where n is the "Number of samples per wavelength" discussed in

Section 3.6 and shown in Figure 3.12. The mean value (Δr/r) of these n values is then stored as the RAS signal at the particular wavelength. At the same time the standard deviation s is computed,

$$s = \sqrt{\frac{1}{n-1}\sum_{i=1}^{n}\left(\left(\frac{\Delta r}{r}\right)_i - \left(\frac{\Delta r}{r}\right)\right)^2} \quad . \tag{3.7}$$

The standard deviation gives the spread of the sampled RAS values. A spectrum for a typical double-peak measurement on silver is plotted in Figure 3.13. Although the standard deviation must be compared to the mean RAS value to get the best impression of the noise, the figure illustrates some important points:

i) In the energy range 1.7-3.6 eV, where the reflected intensity is high for a silver sample, the standard deviation is low, indicating that random noise is not affecting the measured signal significantly.

ii) In the energy range 3.6-4.0 eV, the double peak creates large and fast changing

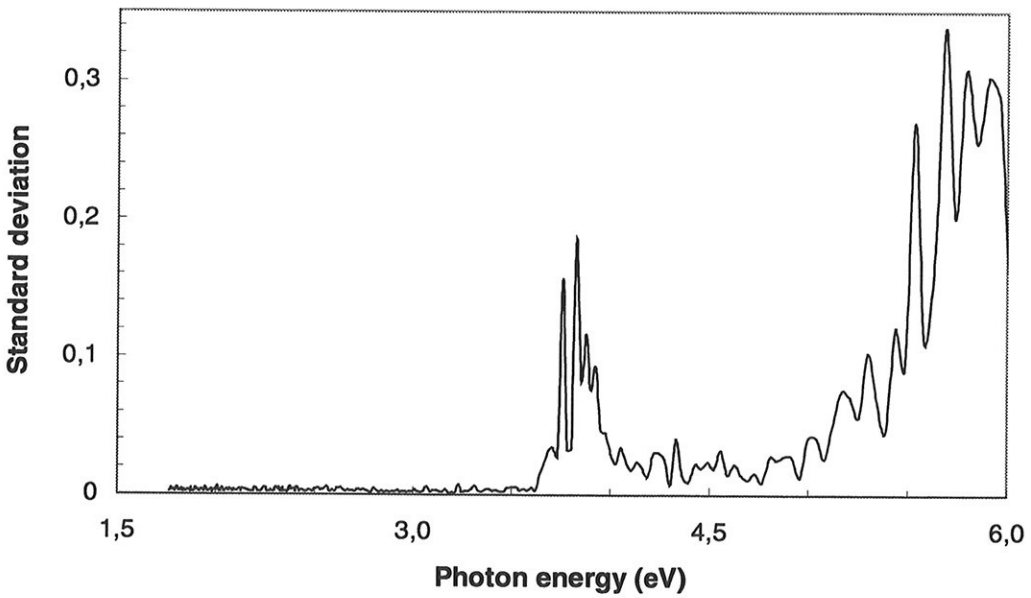

Figure 3.13. Standard deviation spectrum for a double-peak RAS Ag(110) measurement.

values of ($\Delta r/r$) and the standard deviation increases. However the relative error decreases.

iii) In the energy range 4.0-6.0 eV the intensity in the signal drops, and the signal needs to be more amplified. Thus a larger part of the signal will be caused by random noise, since the dark current is also amplified.

From the discussion above it is clear that random noise is most often a problem in the energy range above 4.5 eV, where the intensity is low. To minimise the problem, one can increase the integration time for the measurement, increase the number of samples at each wavelength, and increase the time-constant of the lock-in amplifier.

3.8 Measurement procedures

Sample preparation

The typical sample used in our measurements was a single-crystal metal (Ag, Cu, Ni, Pt, Au), circular with diameter 10 mm and thickness 1.5 mm. Polishing was done by the manufacturers SPL in Holland and MaTeck in Germany, to a corrugation less than 0.03 μm and with an orientation accuracy less than one degree. A sketch of the sample configuration is shown in the left part Figure 3.14. To fix the sample to the sample holder, a notch was prepared at each side of the sample, both of width 0.8 mm and depth 1 mm. In addition, centred (± 5°) between the two crystallographic axes, a small hole of width 0.4 mm and depth 5 mm was made by drilling. This hole was used for mounting the thermocouple to the sample.

Sample mounting

The sample was mounted onto a holder by a bent tungsten wire (Figure 3.14, right part). The wire was isolated from the manipulator arm by small blocks of aluminium oxide. The notches on the side of the samples keep the sample in place. A K-type thermocouple was inserted into the hole at the top of the sample and silver-glue added. If the sample was positioned correctly, it could be rotated around an axis normal to the surface. This was used for error correction. There have been several problems getting the rotation to work seamlessly, and instead a Si(100) sample glued to the back of the sample holder has been used for error correction. In order to easily align the optical components of the external RAS system, a helium-neon laser was used to check the vertical orientation of the sample.

Baking

To speed up the process of reaching the necessary low pressure, the UHV system, including main valve and turbo pump, was heated to about 180°C for 8-24 hours. This was accomplished by encapsulating the chamber with a special box with two 2 kW heat elements and a fan. Two thermostats monitored the temperature, each controlling one heater. After the process of baking, the pressure typically reached $2 \cdot 10^{-10}$ mbar within 24 hours. The titanium-sublimation pump typically reduced the pressure further to below $1 \cdot 10^{-10}$ mbar.

Sample cleaning

Usually, repeating cycles of sputtering and heating was applied to the sample to prepare a clean surface. The noble metal surfaces are rather inert, so only a few cycles (5-10) are required before the characteristic RA spectra can be measured. The LEED was used between cycles to check the improvement of the quality of the surface.

Starting the equipment and alignment of the system

Special care was taken when starting the xenon lamp, due to the 25 keV ignition voltage pulse. Several signal cables were removed to stop transient pulses from propagating through the system and possibly destroy sensitive electronic components.

To reduce noise and offset errors, the electronic components such as the lock-in amplifier, PEM, ADC and amplifier should reach a stable temperature before use. This was

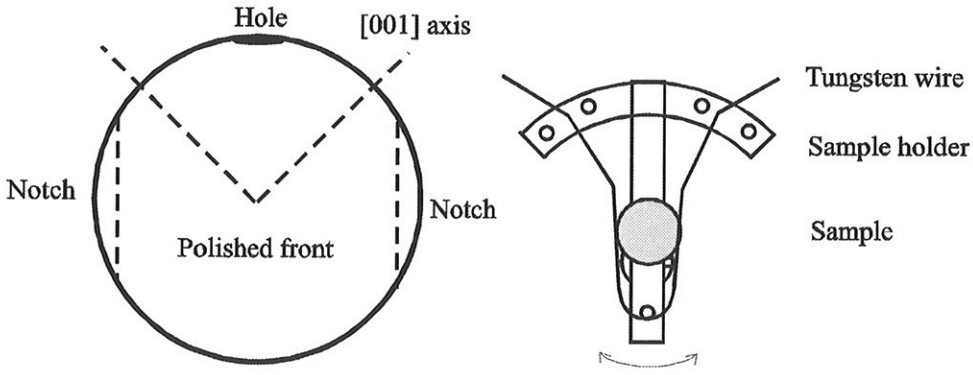

Figure 3.14 Prepared sample (left) and sample holder (right)

accomplished by turning them on at least 30 minutes before measurements.

When the optical system is aligned with respect to the sample, it is important to ensure that the ordinary ray from the polariser hits the sample, not the extraordinary. This was checked by using the fact that the extraordinary ray will rotate when the (Rochon-) polariser is rotated, while the ordinary ray is unchanged. Mirror S3 and S4 was used to optimise the image I4 on the monochromator (see Figure 3.2).

PEM voltage calibration

The prefactor A of the second harmonic of the signal in (2.20) is proportional to the Bessel function J_2 of the amplitude of the phase shift in the PEM,

$$A = 2\left(-\mathrm{Re}\frac{\Delta r}{\bar{r}} - 2\Delta P - 2\Delta M\right) J_2(\delta_m) \ . \tag{3.8}$$

It is necessary to determine the applied phase shift. From (3.2) we know that δ_m depends upon the wavelength and applied gauge voltage as $P(V,C)/\lambda$. If we vary the PEM gauge voltage at a specific wavelength, where the terms in the parenthesis are not zero, the resulting RAS signal varies as a Bessel function, as shown in Figure 3.15. A best fit of the measured curve as a function of voltage with respect to the Bessel function as a function of phase can therefore be used to determine $P(V)$.

Usually, we applied an alternative calibration method. The procedure above was repeated for several different wavelengths, each time we noted the applied voltage V_{J2max} at the first maximum of curve. This corresponds to a phase shift $\delta_M = 3.0521$. The voltage V_{J2max} was then plotted as a function the wavelength, as shown in Figure 3.16. V_{J2max} at other wavelengths could then be approximated by a linear fit to the measured points. An arbitrary retardation δ of the PEM was then accomplished by applying a control voltage

$$V(\delta,\lambda) = \frac{\delta}{\delta_{J2\max}} V_{J2\max}(\lambda) \, . \tag{3.9}$$

In practice, the coefficients in the linear fit in Figure 3.16 are stored in the RASLab software.

It has been argued that the best fit for $V_{J2max}(\lambda)$ is a second-degree polynomial [14]. Figure 3.16 shows the resulting curve, which is a better fit than the line. The difference is very small, however, and in our opinion, a linear fit is sufficient for our system.

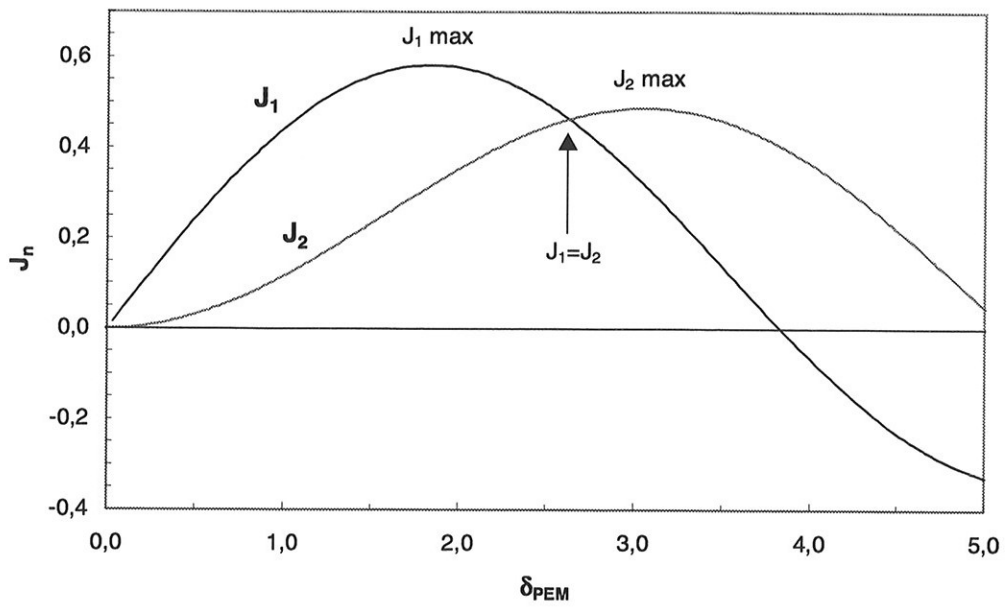

Figure 3.15. The first and second order Bessel functions as a function of the phase amplitude

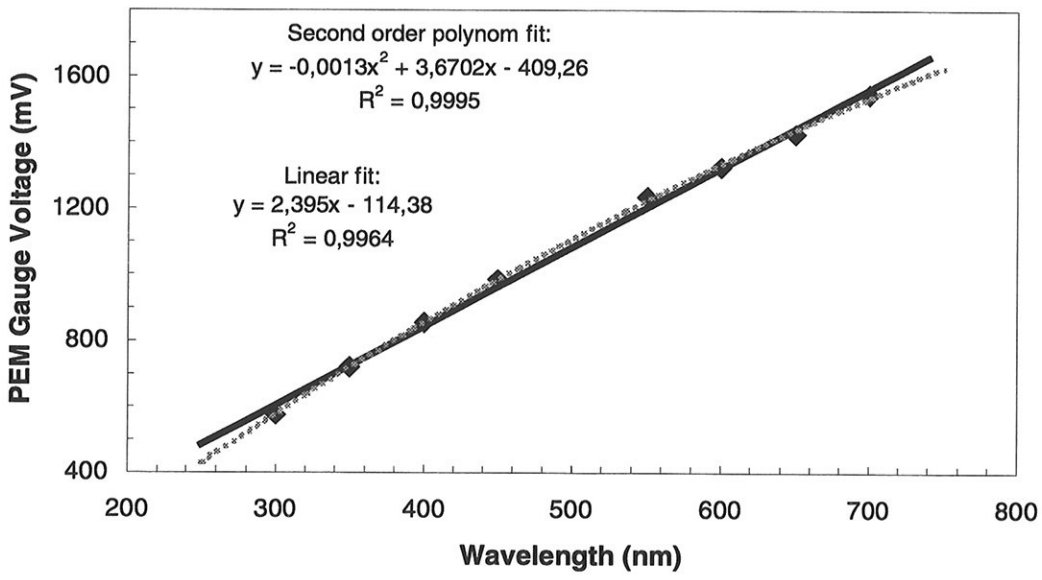

Figure 3.16. PEM calibration for δ_{PEM}=3.0521 (J_2 max) with 8 calibrated wavelengths. Linear fit (solid line) and second order fit (broken line).

If the temperature is stable in the laboratory, the PEM needs to be recalibrated only a few times a year. However, it is good practice to check the calibration from time to time by varying the gauge voltage at a wavelength and check whether the maximum value is as calibrated previously.

Lock-In phase calibration

Electronic components introduce a phase shift φ, in the signal with respect to the reference, as explained in Section 3.4. The lock-in compensates for this by adding an adjustable phase shift. This phase was calibrated using the following method. First, we ensured that the sum of terms in the parenthesis in (3.8) was non-zero. A reference spectrum was used, for example Si(110) in Figure 1.1, and the monochromator was moved to the wavelength of one of the peaks. Alternatively a false signal was produce by rotation of the polariser by a small amount, so that ΔP in (3.8) became different from zero. Either way, the PEM could then be adjusted to V_{J2max} for the given wavelength, and the lock-in output was set to the second harmonic. Now, from (3.5), the phase was adjusted to find the maximum output of the lock-in amplifier. The calibrated phase is suitable for measurements of the real part of RAS, for the imaginary part we added 90°. If the electronic components of the set-up were unchanged, then the calibrated phase was rather stable.

Fine-tuning the polariser angle

If $\Delta P + \Delta M$ in (3.8) is not equal to zero, the measured real part of the RAS spectrum will contain an offset. Therefore, we calibrated those parameters using the following recipe:

1. Align both optical elements as close as possible to the 0° direction defined by Figure 2.3.
2. Use a reference sample that gives zero RAS signal (for example Si(100)).
3. Check that the lock-in outputs the second harmonic signal, and that the PEM is adjusted to the correct phase shift.
4. Adjust the output of the lock-in amplifier to zero by rotating the polariser manually or by the stepmotor.

This procedure had to be repeated quite often, due to vibrations in the complete RAS-UHV system.

ADC offset errors.

These errors are stored in a table in the ADC software component, and are usually not calibrated, due to the small effect on the measured spectrum.

Monochromator and amplifier calibration

The monochromator wavelength setting was calibrated using spectral lamps. A few times a year we checked that the stepmotor-constant (steps/nanometer) was correct.

As mentioned in Section 3.4, the RASLab software stores a table of offset errors for different amplification of the photoamplifier. The standard way to calibrate this table is to block the ray, adjust the amplification to F=100, and use the offset compensation knob of the photoamplifier to adjust the offset at this amplification to zero. Then read the offsets (typically 0-10 mV) at the other amplifications, and input the resulting table to the RASLab software.

Measurement

A detailed procedure for doing a measurement is given in Appendix D as a reference for future users of the RAS system.

To start a measurement it is necessary to select an appropriate PEM phase difference. To minimise noise, the phase giving the maximum of the Besselfunction J_n was usually chosen, where $n = 2$ for the real part of the RA spectrum and $n = 1$ for the imaginary part (see Figure 3.15). For simultaneous measurement of both the real and imaginary RA, the phase giving $J_1 = J_2$ was used. The voltage needed to produce a particular value for the phase retardation is increasing as a function of the wavelength, as shown in Figure 3.16. Therefore, at infrared wavelengths it was occasionally necessary to use a phase shift less than the optimal one.

Subtracting the background spectrum

The real part of the measured reflection anisotropy signal $(\Delta r/r)_M$ is to first order a sum of the real part of the actual reflection anisotropy $(\Delta r/r)_{RAS}$, the real part of the background window spectrum $(\Delta r/r)_{Window}$, and the calibration offset errors ΔP and ΔM (compare with the prefactor in (3.8)):

$$\left(\frac{\Delta r}{r}\right)_M = \left(\frac{\Delta r}{r}\right)_{RAS} + \left(\frac{\Delta r}{r}\right)_{Window} + \Delta P + \Delta M \,. \tag{3.10}$$

The background spectrum disturb the measured RAS curve substantially, hence we needed a way to remove it. We have applied two methods to remove the background and calibration offset errors: i) rotation of the sample and ii) subtraction against the spectrum of Si(100).

If the sample is rotated 90° with respect to the original alignment, the axes on the sample are exchanged, and from the definition (2.2), the reflection anisotropy from the sample change sign. In addition, if everything else in the system is unchanged, the new real part reflection anisotropy signal $(\Delta r/r)_{M90}$,

$$\left(\mathrm{Re}\frac{\Delta r}{r}\right)_{M90} = -\left(\mathrm{Re}\frac{\Delta r}{r}\right)_{RAS} + \left(\mathrm{Re}\frac{\Delta r}{r}\right)_{Window90} + \Delta P + \Delta M \tag{3.11}$$

can be subtracted from the original one to give the correct RAS for the sample,

$$\frac{1}{2}\left(\left(\mathrm{Re}\frac{\Delta r}{r}\right)_{M90} - \left(\mathrm{Re}\frac{\Delta r}{r}\right)_{M90}\right) = \left(\mathrm{Re}\frac{\Delta r}{r}\right)_{RAS}. \tag{3.12}$$

In this way both the spectrum from the window and calibration offset levels can be removed. However, there are at least two problems with this method. First of all the sample in most cases cannot be rotated without wobbling, and the two spectra $(\Delta r/r)_{Window}$ and $(\Delta r/r)_{Window90}$ are therefore unequal. When using a strain-free window, the difference is usually not large, however, but the error reduces the accuracy of the measurement, especially in the imaginary part. The other problem is that in many *in-situ* measurements, the rotation cannot be done, and another type of correction must therefore be applied.

Any sample with an isotropic surface and bulk, for example Si(100), can be used as a zero reference. After measuring the original sample, the RA spectrum of Si(100) is recorded, and this spectrum is subtracted from the spectrum of the sample. This method suffer from the same problem as the rotational correction, because the Si(100) sample must replace the original sample without any wobbling for the two spectra from the window to be equal. Figure 3.17 illustrates this method applied to the Ni(110) surface. The surface was cleaned with several cycles of sputtering and annealing in vacuum. After that, the UHV chamber was filled with air to 1 bar. We measured the nickel surface in the vacuum chamber with air through the low-strain window. The lower broken line in the figure is the resulting spectrum. A Si(100) reference sample in the chamber with air was subsequently measured. The upper broken line is the reference spectrum. The background-corrected spectrum is plotted as a thin solid line. Finally, the Ni sample was removed from the chamber, and measured in air without

any interfering window. The resulting spectrum is represented by a thick solid line in Figure 3.17. It can be seen that the curve closely matches the window-corrected spectrum. The small discrepancies are probably due to the rather low integration time used in this particular measurement. This proves that the method of subtracting a zero spectrum works rather well, and the resulting spectra can be trusted.

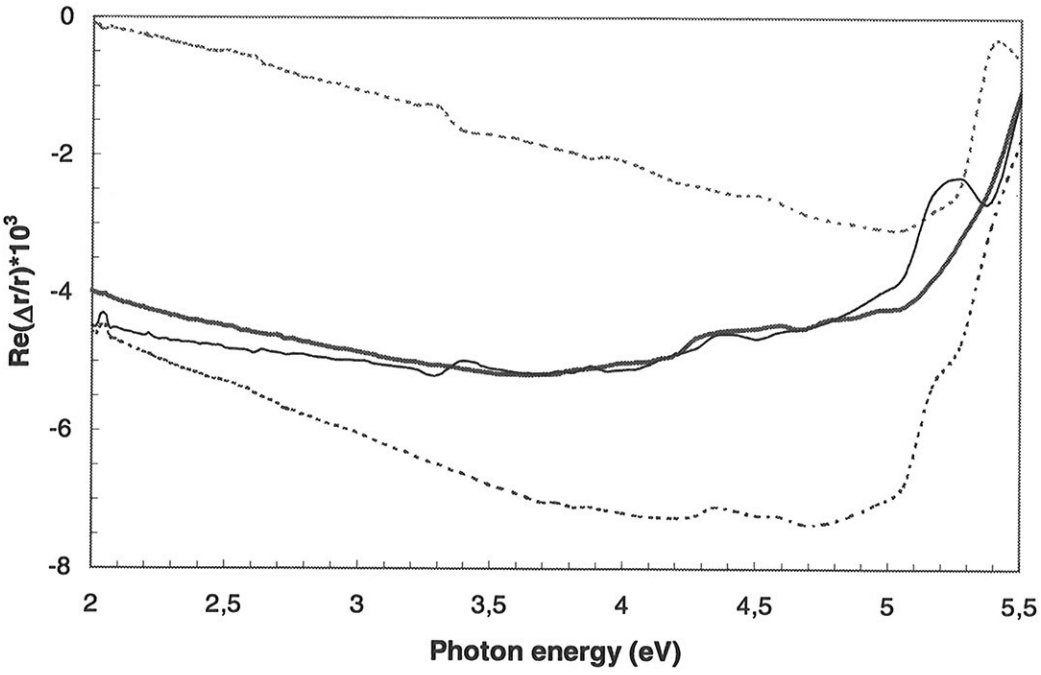

Figure 3.17. Real part of RAS of Ni(110) in air. Spectrum with no window (thick line), spectrum with window (lower broken line), window-correction spectrum (upper broken line) and window-corrected spectrum in UHV (thin solid line).

4 Local-field effect theory

A reflection difference between the principal axes on the surface can be attributed to several different sources, geometrical as well as electronic, and macroscopic as well as microscopic. As our goal is to obtain knowledge about surface optical properties and electronic states, we constrain our interest to those effects that show energy dependence in the spectra, preferably in the optical wavelength area.

It is possible to calculate the reflectivity of electromagnetic radiation by solving the complete Schrödinger equation for the system. Because of the complexity of the problem, the equation must be simplified by approximations, for example by replacing the energy density of the inhomogeneous electron gas with the value for a homogeneous electron gas, as in local density approximation theory (LDA). However, we have to solve the equation by complex and time consuming numerical methods, often to discover that the resulting reflection anisotropy spectra may be very different from the measured curve.

It is therefore of interest to examine to what degree the local electromagnetic model introduced by Tarriba and Mochan [15] can explain the measured signal. The reflection anisotropy is determined by difference in surface conductivity along the two main crystallographic axes,

$$\frac{\Delta r}{r} = \frac{2(\sigma_x - \sigma_y)}{c\varepsilon_0(\varepsilon - 1)}. \tag{4.1}$$

The internal electric field produced by electric dipoles located at the lattice points in a crystal is of central importance in the theory of dielectric phenomena. We start by calculating the self-consistent electric field near the surface under the influence of an external field. Given the polarisability α, it is then possible to calculate deviation from bulk values for the atomic dipole moments $\vec{p}$ as we approach the surface. The surface current density can be expressed as

$$\sigma = -i a \varepsilon_0 \, 2^{-3/2} \, \omega(\varepsilon - \varepsilon_{Drude}) \sum_n \frac{p_n - p_B}{p_B}, \tag{4.2}$$

and using (4.1), it is possible to calculate the reflection anisotropy spectra [15].

4.1 Dipole moments at the surface

Model

We look at the geometry of an fcc lattice, with ion cores at each lattice point surrounded by electrons. For example, a copper atom contains 29 electrons in neutral state, distributed as $1s^2 2s^2 2p^6 3s^2 3p^6 3d^{10} 4s^1$. The calculations are based on the fact that the outermost *d* electrons tend to be *localised* around the ionic core of the atoms in the fcc lattice, whereas the outermost *s (p)* electrons are *delocalised.* Since the 3d orbital is fully occupied, one can assume that there is a small imaginary sphere containing the distributed electron density of the *d*-electrons at each lattice point. The space between the spheres contains the conducting *s* electrons. This is included in the model by positioning a dipole at the centre of each sphere. The result is called the *Swiss cheese model,* schematically shown in Figure 4.1. The electron distribution close to the surface rearranges to give an electric field as if there were mirror dipoles induced above the surface. The absolute value and parallel components of the mirror

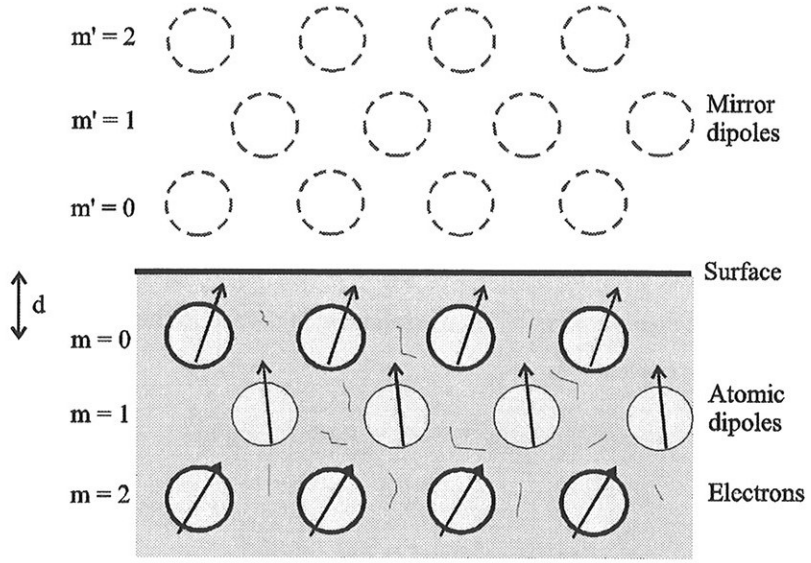

Figure 4.1. The Swiss cheese model.

dipole moments are equal to the real dipoles, but the normal component has the opposite direction.

Local Field

The electric field at lattice point i can be expressed as

$$\vec{E}_{total} = \vec{E}_0 + \vec{E}_d + \vec{E}_m + \vec{E}_e + \vec{E}_s \quad , \tag{4.3}$$

where	**is the**
$\vec{E}_0$	external applied field,
$\vec{E}_d$	field from all dipoles j $\neq i$,
$\vec{E}_m$	field from all mirror dipoles j',
$\vec{E}_e$	field from the surrounding electron gas,
$\vec{E}_s$	field from induced mirror charges outside the sphere.

The latter two terms can be included in the polarisability α, so that the dipole moment at each lattice point i is

$$\vec{p}_i = \alpha\left[E_0 + \sum_{j\neq i}\frac{3\vec{r}_{ij}(\vec{p}_j\cdot\vec{r}_{ij}) - \vec{p}_j\left|\vec{r}_{ij}\right|^2}{4\pi\varepsilon_0\left|\vec{r}_{ij}\right|^5} + \sum_{j'}\frac{3\vec{r}_{ij'}(\vec{p}_{j'}\cdot\vec{r}_{ij'}) - \vec{p}_{j'}\left|\vec{r}_{ij'}\right|^2}{4\pi\varepsilon_0\left|\vec{r}_{ij'}\right|^5}\right], \tag{4.4}$$

where r_{ij} defines the lattice vector between dipole i and dipole j [16]. The above terms are the familiar dipole-dipole interaction. The first (infinite) summation runs over all lattice points. The last term is a summation over all the contributions from the mirror dipoles induced above the surface by the screening semi-infinite electron gas. We now define the x and y component to be orthogonal in-plane directions, while the z component is normal to the plane. The above expression can be written explicitly as

$$\begin{aligned}\vec{p}_i = \alpha\vec{E}_0 &+ \frac{\alpha}{4\pi\varepsilon_0}\sum_{j\neq i}\frac{3\vec{r}_{ij}(p_{jx}r_{ijx} + p_{jy}r_{ijy} + p_{jz}r_{ijz}) - \vec{p}_j\left|\vec{r}_{ij}\right|^2}{\left|\vec{r}_{ij}\right|^5} \\ &+ \frac{\alpha}{4\pi\varepsilon_0}\sum_{j'}\frac{3\vec{r}_{ij'}(p_{j'x}r_{ij'x} + p_{j'y}r_{ij'y} + p_{j'z}r_{ij'z}) - \vec{p}_{j'}\left|\vec{r}_{ij'}\right|^2}{\left|\vec{r}_{ij'}\right|^5}\end{aligned} \quad . \tag{4.5}$$

There are three equations, one for each component (x, y, z). The x-component is

$$p_{ix} = \alpha \vec{E}_0 + \frac{\alpha}{4\pi\varepsilon_0} \sum_{j\neq i} \frac{3r_{ijx}(p_{jx}r_{ijx} + p_{jy}r_{ijy} + p_{jz}r_{ijz}) - p_{jx}\left(r_{ijx}^2 + r_{ijy}^2 + r_{ijy}^2\right)^2}{\left|\vec{r}_{ij}\right|^5}$$
$$+ \frac{\alpha}{4\pi\varepsilon_0} \sum_{j'} \frac{3r_{ij'x}(p_{j'x}r_{ij'x} + p_{j'y}r_{ij'y} + p_{j'z}r_{ij'z}) - p_{j'x}\left(r_{ij'x}^2 + r_{ij'y}^2 + r_{ij'y}^2\right)^2}{\left|\vec{r}_{ij'}\right|^5} \quad . \tag{4.6}$$

In general, there is a coupling between the dipole moments in the three different directions. That is, the x-component of a dipole depends on all three components (p_x, p_y, p_z) of a neighbouring dipole. The three equations can also be written in matrix form:

$$\vec{p}_i = \alpha \vec{E}_0 + \frac{\alpha}{4\pi\varepsilon_0} \sum_{j\neq i} \frac{1}{\left|\vec{r}_{ij}\right|^5} \begin{pmatrix} 3r_{ijx}^2 - \vec{r}_{ij}^2 & 3r_{ijx}r_{ijy} & 3r_{ijx}r_{ijz} \\ 3r_{ijy}r_{ijx} & 3r_{ijy}^2 - \vec{r}_{ij}^2 & 3r_{ijy}r_{ijz} \\ 3r_{ijz}r_{ijz} & 3r_{ijz}r_{ijy} & 3r_{ijz}^2 - \vec{r}_{ij}^2 \end{pmatrix} \begin{pmatrix} p_{jx} \\ p_{jy} \\ p_{jz} \end{pmatrix}$$
$$+ \frac{\alpha}{4\pi\varepsilon_0} \sum_{j'} \frac{1}{\left|\vec{r}_{ij'}\right|^5} \begin{pmatrix} 3r_{ij'x}^2 - \vec{r}_{ij'}^2 & 3r_{ij'x}r_{ij'y} & 3r_{ij'x}r_{ij'z} \\ 3r_{ijy}r_{ijx} & 3r_{ij'y}^2 - \vec{r}_{ij'}^2 & 3r_{ij'y}r_{ij'z} \\ 3r_{ij'z}r_{ij'z} & 3r_{ij'z}r_{ij'y} & 3r_{ij'z}^2 - \vec{r}_{ij'}^2 \end{pmatrix} \begin{pmatrix} p_{j'x} \\ p_{j'y} \\ p_{j'z} \end{pmatrix} \quad . \tag{4.7}$$

For an incoming plane electromagnetic wave, the symmetry ensures that the dipoles in plane m are identical. The sum is split into two contributions, first a summation over all planes m, and second a summation over all in-plane dipoles,

$$\vec{p}_n = \alpha \vec{E}_0 + \frac{\alpha}{4\pi\varepsilon_0} \sum_m \left\{ \sum_j \frac{1}{\left|\vec{r}_{ij}\right|^5} \begin{pmatrix} 3r_{ijx}^2 - \vec{r}_{ij}^2 & 3r_{ijx}r_{ijy} & 3r_{ijx}r_{ijz} \\ 3r_{ijy}r_{ijx} & 3r_{ijy}^2 - \vec{r}_{ij}^2 & 3r_{ijy}r_{ijz} \\ 3r_{ijz}r_{ijz} & 3r_{ijz}r_{ijy} & 3r_{ijz}^2 - \vec{r}_{ij}^2 \end{pmatrix} \right\} \begin{pmatrix} p_{mx} \\ p_{my} \\ p_{mz} \end{pmatrix} +$$
$$+ \frac{\alpha}{4\pi\varepsilon_0} \sum_{m'} \left\{ \sum_{j'} \frac{1}{\left|\vec{r}_{ij'}\right|^5} \begin{pmatrix} 3r_{ij'x}^2 - \vec{r}_{ij'}^2 & 3r_{ij'x}r_{ij'y} & 3r_{ij'x}r_{ij'z} \\ 3r_{ijy}r_{ijx} & 3r_{ij'y}^2 - \vec{r}_{ij'}^2 & 3r_{ij'y}r_{ij'z} \\ 3r_{ij'z}r_{ij'z} & 3r_{ij'z}r_{ij'y} & 3r_{ij'z}^2 - \vec{r}_{ij'}^2 \end{pmatrix} \right\} \begin{pmatrix} p_{m'x} \\ p_{m'y} \\ p_{m'z} \end{pmatrix} \quad . \tag{4.8}$$

The terms in the brackets are independent of material properties other than pure geometrical, as they are summations over lattice points only. We therefore write

$$\vec{p}_n = \frac{\alpha}{4\pi\varepsilon_0} \left[4\pi\varepsilon_0 \vec{E}_0 + \sum_m \begin{pmatrix} U_{11}^{nm} & U_{12}^{nm} & U_{13}^{nm} \\ U_{21}^{nm} & U_{22}^{nm} & U_{23}^{nm} \\ U_{31}^{nm} & U_{32}^{nm} & U_{33}^{nm} \end{pmatrix} \begin{pmatrix} p_{mx} \\ p_{my} \\ p_{mz} \end{pmatrix} + \sum_{m'} \begin{pmatrix} U_{11}^{nm'} & U_{12}^{nm'} & U_{13}^{nm'} \\ U_{21}^{nm'} & U_{22}^{nm'} & U_{23}^{nm'} \\ U_{31}^{nm'} & U_{32}^{nm'} & U_{33}^{nm'} \end{pmatrix} \begin{pmatrix} p_{m'x} \\ p_{m'y} \\ p_{m'z} \end{pmatrix} \right], \tag{4.9}$$

where the plane interaction coefficient U_{xy}^{nm} is the contribution to the x-component of a dipole in plane n from the y-components of all dipoles in plane m (m' for mirror planes). This matrix is calculated for different combinations of (m-n). Note that the sum of the diagonal elements is zero, i.e.

$$\vec{U}_{11}^{nm} + \vec{U}_{22}^{nm} + \vec{U}_{33}^{nm} = 0 \,. \tag{4.10}$$

For a specific surface type of a given lattice, for example the (110) surface of a face-centred cubic lattice, the coefficients U/a^3 (a= lattice constant), are independent of the atom type. Therefore, once calculated, they can be applied to all metals satisfying the assumptions behind the model.

Face-centred cubic (110) surface

To make an explicit calculation of the plane interaction matrix U, we need to specify some parameters:

- The lattice is face-centred cubic.
- The surface is (110) (see Figure 2.2).
- m=0 defines the plane closest to the surface (see Figure 4.1).
- The distance from the plane m=0 to the mirror surface is d.

It is important to note that the plane-plane interaction only depends on the absolute value of the difference in plane indicies $|m-n|$. For example, the interaction between a dipole in plane n=1 and all dipoles in plane m = 3 is the same as the interaction between a dipole in n = 4 and all dipoles in plane m = 2. We have assumed that there is no relaxation of the atomic layers. The atoms in the first mirror plane (m = 0) is situated above the topmost surface plane, all other neighbouring planes are shifted with half a surface unit cell with respect to each other. The effect of mirror dipoles depends on the distance d from the topmost surface plane to the

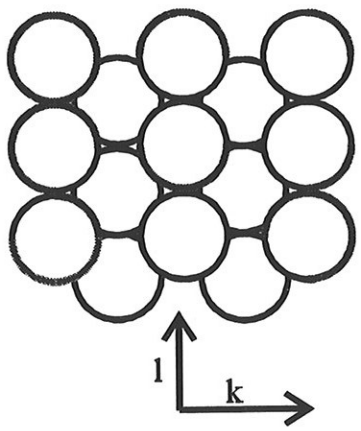

Figure 4.2. Definition of axes on the (110) surface. The l parameter corresponds to the $[\bar{1}10]$ axis and the k parameter to the [001] axis.

electronic surface. If the cutting of the surface is perfect, and if there is no spill-out of the electrons, the effective surface is defined by the step in electron density at a distance half the interplanar length from the topmost plane of the ion cores,

$$d = \frac{1}{2}\frac{a}{2\sqrt{2}} = 2^{-\frac{5}{2}} a \ . \tag{4.11}$$

The lattice vectors r_{ij} are defined with the help of Figure 4.2, and we need to distinguish between four different cases for the in-plane summation:

(a) (*m-n*) is a multiple of 2:

$$\vec{r}_{ij} = \begin{pmatrix} r_{ijx} \\ r_{ijy} \\ r_{ijz} \end{pmatrix} = \begin{pmatrix} k \cdot a \\ l \cdot \dfrac{a}{\sqrt{2}} \\ |m-n| \cdot \dfrac{a}{2\sqrt{2}} \end{pmatrix} \qquad \begin{array}{c} k = \ldots -1, 0, 1, \ldots \\ l = \ldots -1, 0, 1, \ldots \\ m \geq 0 \\ n \geq 0 \end{array} \tag{4.12}$$

(b) (*m-n*) is not a multiple of 2:

$$\vec{r}_{ij} = \begin{pmatrix} r_{ijx} \\ r_{ijy} \\ r_{ijz} \end{pmatrix} = \begin{pmatrix} \left(k + \frac{1}{2}\right) \cdot a \\ \left(l + \frac{1}{2}\right) \cdot \dfrac{a}{\sqrt{2}} \\ |m-n| \cdot \dfrac{a}{2\sqrt{2}} \end{pmatrix} \qquad \begin{array}{c} k = \ldots -1, 0, 1, \ldots \\ l = \ldots -1, 0, 1, \ldots \\ m \geq 0 \\ n \geq 0 \end{array} \tag{4.13}$$

(c) (*m'+n*) is not a multiple of 2:

$$\vec{r}_{ij} = \begin{pmatrix} r_{ijx} \\ r_{ijy} \\ r_{ijz} \end{pmatrix} = \begin{pmatrix} k \cdot a \\ l \cdot \dfrac{a}{\sqrt{2}} \\ (m+n) \cdot \dfrac{a}{2\sqrt{2}} + 2d \end{pmatrix} \qquad \begin{array}{c} k = \ldots -1, 0, 1, \ldots \\ l = \ldots -1, 0, 1, \ldots \\ m \geq 0 \\ n \geq 0 \end{array} \tag{4.14}$$

(d) (*m'+n*) is a multiple of 2:

$$\vec{r}_{ij} = \begin{pmatrix} r_{ijx} \\ r_{ijy} \\ r_{ijz} \end{pmatrix} = \begin{pmatrix} (k+\frac{1}{2})\cdot a \\ (l+\frac{1}{2})\cdot \frac{a}{\sqrt{2}} \\ (m+n)\cdot \frac{a}{2\sqrt{2}} + 2d \end{pmatrix} \quad \begin{matrix} k = \ldots -1,0,1,\ldots \\ l = \ldots -1,0,1,\ldots \\ m \geq 0 \\ n \geq 0 \end{matrix} \tag{4.15}$$

First, we try to find the coefficients U for situation (a), where the atoms in plane m is positioned right on top (or below) atoms in plane n. The following calculation serve as an example of how to do the calculation for the other situations (b) – (d). To simplify the expressions, we write

$$s \equiv |m-n| \cdot \frac{1}{2\sqrt{2}} \tag{4.16}$$

The lattice vectors can be applied to the U matrix as defined by (4.8) and (4.9), and the result is

$$\vec{U}^{nm} = \frac{1}{a^3} \sum_{l=-\infty}^{\infty} \sum_{k=-\infty}^{\infty} \frac{1}{(k^2 + \frac{l^2}{2} + s^2)^{\frac{3}{2}}} \begin{pmatrix} \frac{3k^2}{(k^2+\frac{l^2}{2}+s^2)} - 1 & \frac{\frac{3}{\sqrt{2}}kl}{(k^2+\frac{l^2}{2}+s^2)} & \frac{3ks}{(k^2+\frac{l^2}{2}+s^2)} \\ \frac{\frac{3}{\sqrt{2}}kl}{(k^2+\frac{l^2}{2}+s^2)} & \frac{\frac{3}{2}l^2}{(k^2+\frac{l^2}{2}+s^2)} - 1 & \frac{\frac{3}{\sqrt{2}}ls}{(k^2+\frac{l^2}{2}+s^2)} \\ \frac{3ks}{(k^2+\frac{l^2}{2}+s^2)} & \frac{\frac{3}{\sqrt{2}}ls}{(k^2+\frac{l^2}{2}+s^2)} & \frac{3s^2}{(k^2+\frac{l^2}{2}+s^2)} - 1 \end{pmatrix} \tag{4.17}$$

The summation runs over every integer k and every integer l (when m=0, (k,l)=(0,0) must be excluded). Immediately it is seen from symmetry reasons that all off-diagonal elements are zero. The summation takes care of remove the coupling between the dipole moments in the three different directions. However, as we shall see in Section 4.10, this feature is strictly due to the symmetry of a perfect fcc(110) surface, and if we break the symmetry by adding or removing atoms, the coupling has to be taken into account..

Spherical coordinates

It may be helpful to express the plane-wise dipole-dipole interaction coefficients (4.17) in terms of spherical coordinates. They can be defined as follows:

$$\cos\phi\sin\theta = \frac{r_x}{r} = \frac{k}{\sqrt{(k^2 + \frac{l^2}{2} + s^2)}}, \tag{4.18}$$

$$\sin\phi\sin\theta = \frac{r_y}{r} = \frac{\frac{l}{\sqrt{2}}}{\sqrt{(k^2 + \frac{l^2}{2} + s^2)}}, \tag{4.19}$$

$$\cos\theta = \frac{r_z}{r} = \frac{s}{\sqrt{(k^2 + \frac{l^2}{2} + s^2)}}. \tag{4.20}$$

Equation (4.17) can then be written

$$\ddot{U}^{nm} = \frac{1}{a^3}\sum_{l=-\infty}^{\infty}\sum_{k=-\infty}^{\infty}\frac{1}{(k^2 + \frac{l^2}{2} + s^2)^{\frac{3}{2}}}\begin{pmatrix} 3\cos^2\phi\sin^2\theta - 1 & 3\cos\phi\sin\phi\sin^2\theta & 3\sin\phi\sin\theta\cos\theta \\ 3\cos\phi\sin\phi\sin^2\theta & 3\sin^2\phi\sin^2\theta - 1 & 3\cos\phi\sin\theta\cos\theta \\ 3\cos\phi\sin\theta\cos\theta & 3\cos\phi\sin\theta\cos\theta & 3\cos^2\theta - 1 \end{pmatrix}. \tag{4.21}$$

Notice that s is just a parameter in this double-sum, and that the summation now takes place over discrete angles defined by k and l.

Evaluation of the coefficients

The sums in (4.17) converge very slowly. Typically, in order to get the two first digits, we need to sum over a few million terms. It is therefore necessary to find alternative methods in order to control the convergence and to speed up the calculation. In the following, two different methods are presented, each applicable to different cases of *m-n*. In the first method we apply the Fourier transform to the series by using the mathematical Hankel transformation. The results are valid for case a) and c) of the lattice vectors r_{ij}, defined on page 61, with the additional limitation that $s > 0$. In the second method we make use of Jacobi's imaginary transform and the gamma function to transform the series into a fast converging sum over Bessel functions. This is a more general approach, and it requires substantially more calculation. However, the results can be applied to all cases a)-d) defined on page 61. By using two completely different methods we are able to compare independent results, and thus it is easier to discover errors or inconsistencies. Appendix E lists several results for the dipole-dipole coefficients.

4.2 Dipole interaction coefficients calculated by the Hankel transformation

In this section we develop the lattice sums in terms of associated Legendre polynomials,

$$P_n^m(x) = (1-x^2)^{m/2}\frac{\mathrm{d}^m P_n}{\mathrm{d}x^m}, \tag{4.22}$$

where P_n is the standard Legendre polynomials of degree n. We then apply the Hankel transformation to transform the series into a two-dimensional Fourier-space.

Since $P_n^m(x) = 0$ when $m > n$, the only non-zero associated Legendre polynomials of the second degree are (not normalised):

$$P_2^0(\cos\theta) \equiv \tfrac{1}{2}\left(3\cos^2\theta - 1\right), \tag{4.23}$$

$$P_2^1(\cos\theta) \equiv -3\cos\theta\sin\theta\ , \tag{4.24}$$

$$P_2^2(\cos\theta) \equiv 3\sin^2\theta\ . \tag{4.25}$$

We are in particular interested in the spherical harmonics F_m,

$$F_m \equiv Y_2^m \equiv P_2^{|m|}(\cos\theta)\,e^{im\phi}\ . \tag{4.26}$$

For m = -2, …, 2, the spherical harmonics are:

$$F_{\pm 2} = 3\sin^2\theta\cos^2\phi - 3\sin^2\theta\sin^2\phi \pm i6\sin^2\theta\cos\phi\sin\phi\ , \tag{4.27}$$

$$F_{\pm 1} = -3\cos\theta\sin\theta\cos\phi \mp i3\cos\theta\sin\theta\sin\phi \tag{4.28}$$

$$F_0 = \tfrac{1}{2}\left(3\cos^2\theta - 1\right) \tag{4.29}$$

Each term in the matrix (4.21) can now be expressed as a sum of these harmonics,

$$\begin{aligned}\tfrac{1}{4}\left(F_2 + F_{-2}\right) - F_0 &= \tfrac{1}{2}\left(3\sin^2\theta\cos^2\phi - 3\sin^2\theta\sin^2\phi - 3\cos^2\theta + 1\right)\\ &= 3\sin^2\theta\cos^2\phi - 1\end{aligned}, \tag{4.30}$$

$$-i\tfrac{1}{4}\left(F_2 - F_{-2}\right) = -i\tfrac{1}{4}i12\sin^2\theta\cos\phi\sin\phi = 3\sin^2\theta\cos\phi\sin\phi\,, \tag{4.31}$$

etc., and we find

$$\ddot{U}^{nm} = \frac{1}{a^3}\sum_{l=-\infty}^{\infty}\sum_{k=-\infty}^{\infty}\frac{1}{(k^2 + \frac{l^2}{2} + s^2)^{\frac{3}{2}}}\begin{pmatrix} \frac{1}{4}F_2 - F_0 + \frac{1}{4}F_{-2} & -i\frac{1}{4\sqrt{2}}F_2 + i\frac{1}{4\sqrt{2}}F_{-2} & i\frac{1}{2}F_1 - i\frac{1}{2}F_{-1} \\ -i\frac{1}{4\sqrt{2}}F_2 + i\frac{1}{4\sqrt{2}}F_{-2} & -\frac{1}{4}F_2 - F_0 - \frac{1}{4}F_{-2} & -\frac{1}{2\sqrt{2}}F_1 - \frac{1}{2\sqrt{2}}F_{-1} \\ i\frac{1}{2}F_1 - i\frac{1}{2}F_{-1} & -\frac{1}{2\sqrt{2}}F_1 - \frac{1}{2\sqrt{2}}F_{-1} & 2F_0 \end{pmatrix}. \tag{4.32}$$

The series still converge very slowly. The plane-wise dipole-dipole interaction on the z-component of a dipole in plane n from the z-components of dipoles in plane m is described by $\ddot{U}_{33}^{nm}$:

$$U_{33}^{nm} = \frac{1}{a^3}\sum_{l=-\infty}^{\infty}\sum_{k=-\infty}^{\infty}\frac{2F_0}{(k^2+\frac{l^2}{2}+s^2)^{3/2}} \tag{4.33}$$

By introducing delta functions, this expression can be rewritten to give

$$\begin{aligned} U_{33}^{nm} &= \frac{1}{a^3}\sum_{l=-\infty}^{\infty}\sum_{k=-\infty}^{\infty}\int d\vec{r}_{xy}\,\delta(\vec{r}_{xy}-\vec{r}_{kl})\frac{2F_0}{(r^2+s^2)^{3/2}} \\ &= \frac{1}{a^3}\int d\vec{r}_{xy}\frac{2F_0}{(r^2+s^2)^{3/2}}\sum_{l=-\infty}^{\infty}\sum_{k=-\infty}^{\infty}\delta(\vec{r}_{xy}-\vec{r}_{kl}) \\ &= \frac{1}{a^3}\int d\vec{r}_{xy}\frac{2F_0}{(r^2+s^2)^{3/2}}\sqrt{2}\sum_{l=-\infty}^{\infty}\sum_{k=-\infty}^{\infty}e^{-i\vec{q}_{kl}\vec{r}} \\ &= \frac{2\sqrt{2}}{a^3}\sum_{l=-\infty}^{\infty}\sum_{k=-\infty}^{\infty}\int d\vec{r}_{xy}\frac{F_0}{(r^2+s^2)^{3/2}}e^{-i\vec{q}_{kl}\vec{r}} \end{aligned}, \tag{4.34}$$

where we have used the identity

$$\sum_{k=-\infty}^{\infty}\sum_{l=-\infty}^{\infty}\delta(\vec{r}_{xy}-\vec{r}_{kl}) = \frac{1}{A_E}\sum_{k=-\infty}^{\infty}\sum_{l=-\infty}^{\infty}e^{-i\vec{q}_{kl}\vec{r}}\ . \tag{4.35}$$

The summations on the right side of (4.34) and (4.35) are over reciprocal lattice points defined by k and l. The area of the surface unit cell is A_E. We now apply the Hankel transformation [17],

$$\int_0^{\infty}\int_0^{2\pi}\frac{P_l^{|m|}\left(\frac{s}{(r_{xy}^2+s^2)^{1/2}}\right)}{(r_{xy}^2+s^2)^{(l+1)/2}}e^{im\phi}e^{i\vec{q}\vec{r}_{xy}}\,rd\phi\,dr = \frac{q^{l-\frac{1}{2}}e^{-sq}(-1)^m}{(l-m)!}, \tag{4.36}$$

which is valid for $s > 0$ and $l > 0$ (here, m is the Legendre index, not the plane index m). In our case, this formula can be simplified to give

$$\int_0^{\infty}\int_0^{2\pi}\frac{F_m}{(r_{xy}^2+s^2)^{3/2}}e^{-i\vec{q}\vec{r}_{xy}}\,rd\phi\,dr = \frac{2\pi i^m e^{im}}{\sqrt{q}}\frac{q^{\frac{3}{2}}e^{-dq}(-1)^m}{(2-m)!}\ , \tag{4.37}$$

where ω is the angle between the x-axis and $\vec{q}$, so that (4.34) simplifies to

$$U_{33} = \frac{2\sqrt{2}}{a^3}\sum_{l=-\infty}^{\infty}\sum_{k=-\infty}^{\infty}\left.\frac{2\pi i^m e^{im\omega}q_{kl}e^{-sq_{kl}}(-1)^m}{(2-m)!}\right|_{m=0} = \frac{2\sqrt{2}\pi}{a^3}\sum_{l=-\infty}^{\infty}\sum_{k=-\infty}^{\infty}q_{kl}e^{-sq_{kl}}\ . \tag{4.38}$$

As k and l increases, the exponent on the right side of this equation decreases rapidly, and the sum converges very fast. If we do the same calculation for the other terms in (4.32) we get

$$\ddot{U}^{nm} = \frac{4\sqrt{2}\pi}{a^3}\sum_{l=-\infty}^{\infty}\sum_{k=-\infty}^{\infty}q_{kl}e^{-sq_{kl}}\begin{pmatrix} -\frac{1}{4}e^{i2\omega}-\frac{1}{2}-\frac{1}{4}e^{-i2\omega} & i\frac{1}{4\sqrt{2}}e^{i2\omega}-i\frac{1}{4\sqrt{2}}e^{-i2\omega} & \frac{1}{2}e^{i\omega}+\frac{1}{2}e^{-i\omega} \\ i\frac{1}{4\sqrt{2}}e^{i2\omega}-i\frac{1}{4\sqrt{2}}e^{-i2\omega} & \frac{1}{4}e^{i2\omega}-\frac{1}{2}+\frac{1}{4}e^{-i2\omega} & \frac{1}{2\sqrt{2}}ie^{i\omega}-\frac{1}{2\sqrt{2}}ie^{-i\omega} \\ \frac{1}{2}e^{i\omega}+\frac{1}{2}e^{-i\omega} & \frac{1}{2\sqrt{2}}ie^{i\omega}-\frac{1}{2\sqrt{2}}ie^{-i\omega} & 1 \end{pmatrix}, \tag{4.39}$$

$$\tilde{U}^{nm} = \frac{4\sqrt{2}\pi}{a^3}\sum_{l=-\infty}^{\infty}\sum_{k=-\infty}^{\infty} q_{kl} e^{-sq_{kl}} \begin{pmatrix} -\frac{1}{2}(1+\cos 2\omega) & -\frac{1}{2\sqrt{2}}\sin 2\omega & \cos 2\omega \\ -\frac{1}{2\sqrt{2}}\sin 2\omega & -\frac{1}{2}(1-\cos 2\omega) & -\frac{1}{\sqrt{2}}\sin 2\omega \\ \cos 2\omega & -\frac{1}{\sqrt{2}}\sin 2\omega & 1 \end{pmatrix}. \qquad (4.40)$$

From (4.36), the above equation is only valid for $s > 0$, that is when m and n is not equal (in-plane interaction). These series are easily evaluated since the s-dependence is only in the prefactor of the matrix. The transformed sums can typically give six correct digits from only the 3-5 first terms. This is an extreme improvement over direct summation!

The length of the reciprocal lattice vectors q is

$$q_{kl} = (2\pi)\sqrt{\left(k^2 + 2l^2\right)}, \qquad (4.41)$$

and the angle ω between the x –axis and $\vec{q}$ is

$$\omega = \omega_{kl} = \arccos\frac{k}{\sqrt{k^2+2l^2}} \qquad (4.42)$$

In Appendix E, numerical values for these sums are tabulated.

4.3 Interaction coefficients obtained by Bessel functions

Van der Hoff and Benson [18] use a different approach to solve the dipolsums. Their method contains some degrees of freedom, and here we will look at two alternative uses of it. In all the calculations below the factor $1/a^3$ has been excluded from the U coefficients for easier readability.

Alternative 1, for on-top plane interaction

We follow van der Hoff and Benson [18]. First we look at the plane interaction coefficient U_{11}^{nm}, the contribution to the x-component of a dipole in plane n from the x-components of all dipoles in plane m (m - n is a multiple of 2).

U_{11}

We employ Euler's definition of the gamma function,

$$\left(a^2+b^2+c^2\right)^{-n} = \frac{1}{\Gamma(n)}\int_0^{\infty} t^{n-1} e^{-\left(a^2+b^2+c^2\right)t} dt, \qquad n > 0, \qquad (4.43)$$

to introduce integrals into the sums:

$$U_{11}^{nm} = \sum_{k=-\infty}^{\infty}\sum_{l=-\infty}^{\infty}\left(\frac{3k^2}{(k^2+\frac{l^2}{2}+s^2)^{\frac{5}{2}}} - \frac{1}{(k^2+\frac{l^2}{2}+s^2)^{\frac{3}{2}}}\right) \tag{4.44}$$
$$= \left(\frac{1}{\Gamma(5/2)}\int_0^{\infty}\sum_{k=-\infty}^{\infty}\sum_{l=-\infty}^{\infty}3k^2 t^{\frac{3}{2}} e^{-(k^2+\frac{l^2}{2}+s^2)t}dt\right) - \left(\frac{1}{\Gamma(3/2)}\int_0^{\infty}\sum_{k=-\infty}^{\infty}\sum_{l=-\infty}^{\infty}t^{\frac{1}{2}} e^{-(k^2+\frac{l^2}{2}+s^2)t}dt\right)$$

This equation can be transformed with the help of a special case of Jacobi's imaginary transform,

$$\sum_{p=-\infty}^{\infty} e^{-p^2 t} = \left(\frac{\pi}{t}\right)^{\frac{1}{2}}\sum_{q=-\infty}^{\infty} e^{-q^2\pi^2/t}, \tag{4.45}$$

so that equation (4.44) takes the form

$$U_{11}^{nm} = \left(\frac{1}{\Gamma(\frac{5}{2})}\int_0^{\infty}\left(\frac{2\pi}{t}\right)^{\frac{1}{2}}\sum_{k=-\infty}^{\infty}\sum_{q=-\infty}^{\infty}3k^2 t^{\frac{3}{2}} e^{-(k^2+s^2)t-2q^2\pi^2/t}dt\right)$$
$$-\left(\frac{1}{\Gamma(\frac{3}{2})}\int_0^{\infty}\left(\frac{\pi}{t}\right)^{\frac{1}{2}}\left(\frac{2\pi}{t}\right)^{\frac{1}{2}}\sum_{r=-\infty}^{\infty}\sum_{q=-\infty}^{\infty}t^{\frac{1}{2}} e^{-s^2t-2q^2\pi^2/t-r^2\pi^2/t}dt\right). \tag{4.46}$$

The summations in the above expression can be divided into five terms:

$$U_{11}^{nm} = \left(\frac{12\sqrt{2\pi}}{\Gamma(\frac{5}{2})}\int_0^{\infty}\sum_{k=1}^{\infty}\sum_{q=1}^{\infty}k^2 t^1 e^{-(k^2+s^2)t-2q^2\pi^2/t}dt\right) + \left(\frac{6\sqrt{2\pi}}{\Gamma(\frac{5}{2})}\int_0^{\infty}\sum_{k=1}^{\infty}k^2 t^1 e^{-(k^2+s^2)t}dt\right)$$
$$-\left(\frac{2\sqrt{2\pi}}{\Gamma(\frac{3}{2})}\int_0^{\infty}\sum_{r=1}^{\infty}\sum_{q=-\infty}^{\infty}t^{-\frac{1}{2}} e^{-s^2t-2q^2\pi^2/t-r^2\pi^2/t}dt\right) \tag{4.47}$$
$$-\left(\frac{2\sqrt{2\pi}}{\Gamma(\frac{3}{2})}\int_0^{\infty}\sum_{q=1}^{\infty}t^{-\frac{1}{2}} e^{-s^2t-2q^2\pi^2/t}dt\right) - \left(\frac{\sqrt{2\pi}}{\Gamma(\frac{3}{2})}\int_0^{\infty}t^{-\frac{1}{2}} e^{-s^2t}dt\right)$$

It is now possible to apply the integration formula,

$$\int_0^{\infty}t^{n-1}e^{-k^2t-q^2\pi^2/t}dt = 2\left(\frac{q\pi}{k}\right)^n K_n(2kq\pi), \tag{4.48}$$

where K_n is the modified Bessel function of second order, and we get

$$U_{11}^{nm} = \left(\frac{48\sqrt{2}\pi^{\frac{5}{2}}}{\Gamma(\frac{5}{2})}\sum_{k=1}^{\infty}\sum_{q=1}^{\infty}k^2\left(\frac{q}{\sqrt{k^2+s^2}}\right)^2 K_2(2\sqrt{2}\sqrt{k^2+s^2}q\pi)\right) + \left(\frac{6(2\pi)^{\frac{1}{2}}\Gamma(2)}{\Gamma(\frac{5}{2})}\sum_{k=1}^{\infty}\left(\frac{k^2}{(k^2+s^2)^2}\right)\right)$$
$$-\left(\frac{4\sqrt{2\pi}^{\frac{3}{2}}}{\Gamma(\frac{3}{2})}\sum_{r=1}^{\infty}\sum_{q=-\infty}^{\infty}\left(\frac{\sqrt{2q^2+r^2}}{s}\right)^{\frac{1}{2}} K_{\frac{1}{2}}(2\sqrt{2q^2+r^2}s\pi)\right) \tag{4.49}$$
$$-\left(\frac{2^{\frac{11}{4}}\pi^{\frac{3}{2}}}{\Gamma(\frac{3}{2})}\sum_{q=1}^{\infty}\left(\frac{q}{s}\right)^{\frac{1}{2}} K_{\frac{1}{2}}(2\sqrt{2}qs\pi)\right) - \left(\frac{\sqrt{2\pi}\Gamma(\frac{1}{2})}{\Gamma(\frac{3}{2})s}\right)$$

From standard mathematical tables we find numerical values for the gamma function,

$$\Gamma(\tfrac{5}{2})=\frac{3\sqrt{\pi}}{4}\quad \Gamma(1)=1\quad \Gamma(\tfrac{3}{2})=\frac{\sqrt{\pi}}{2}\quad \Gamma(1)=1\quad \Gamma(\tfrac{1}{2})=\sqrt{\pi}\,. \tag{4.50}$$

The result for U_{11}^{nm} is:

$$\begin{aligned} U_{11}^{nm} &= \left(2^{\frac{13}{2}}\pi^2\sum_{k=1}^{\infty}\sum_{q=1}^{\infty}\left(\frac{kq}{\sqrt{k^2+s^2}}\right)^2 K_2(2^{\frac{3}{2}}\sqrt{k^2+s^2}q\pi)\right)+\left(2^{\frac{7}{2}}\sum_{k=1}^{\infty}\left(\frac{k^2}{(k^2+s^2)^2}\right)\right) \\ &-\left(2^{\frac{7}{2}}\pi\sum_{r=1}^{\infty}\sum_{q=-\infty}^{\infty}\left(\frac{\sqrt{2q^2+r^2}}{s}\right)^{\frac{1}{2}} K_{\frac{1}{2}}(2\sqrt{2q^2+r^2}s\pi)\right) \\ &-\left(2^{\frac{15}{4}}\pi\sum_{q=1}^{\infty}\left(\frac{q}{s}\right)^{\frac{1}{2}} K_{\frac{1}{2}}(2^{\frac{3}{2}}qs\pi)\right)-\left(\frac{2^{\frac{3}{2}}\pi}{s}\right) \end{aligned} \tag{4.51}$$

Term 1,3,4 and 5 converge to satisfactorily accuracy after summation over 2-10 terms, and the second term can easily be estimated. Numerical results are given in Appendix E.

U_{22}

The deduction in this case is similar to the U_{11} case. The last of the two terms in (4.44) is not changed when we move to U_{22}. We concentrate on the term corresponding to the first term of (4.44), and proceed as before:

$$\begin{aligned} \sum_{k=-\infty}^{\infty}\sum_{l=-\infty}^{\infty}\frac{\frac{3}{2}l^2}{(k^2+\frac{l^2}{2}+s^2)^{\frac{5}{2}}} &= \left(\frac{1}{\Gamma(5/2)}\int_0^{\infty}\sum_{k=-\infty}^{\infty}\sum_{l=-\infty}^{\infty}\sum\frac{3}{2}l^2t^{\frac{3}{2}}e^{-(k^2+\frac{l^2}{2}+s^2)t}dt\right) \\ &= \left(8\int_0^{\infty}\sum_{l=1}^{\infty}\sum_{q=1}^{\infty}l^2t^1e^{-(\frac{l^2}{2}^2+s^2)t-q^2\pi^2/t}dt\right)+\left(4\int_0^{\infty}\sum_{l=1}^{\infty}l^2t^1e^{-(\frac{l^2}{2}+s^2)t}dt\right) \\ &= \left(16\pi^2\sum_{l=1}^{\infty}\sum_{q=1}^{\infty}\left(\frac{lq}{\sqrt{\frac{l^2}{2}+s^2}}\right)^2 K_2(2\sqrt{\tfrac{l^2}{2}+s^2}q\pi)\right)+\left(4\sum_{l=1}^{\infty}\left(\frac{l^2}{(\frac{l^2}{2}+s^2)^2}\right)\right) \end{aligned} \tag{4.52}$$

This gives us the following expression for U_{22}:

$$\begin{aligned} U_{22}^{nm} &= \left(16\pi^2\sum_{l=1}^{\infty}\sum_{q=1}^{\infty}\left(\frac{lq}{\sqrt{\frac{l^2}{2}+s^2}}\right)^2 K_2(2\sqrt{\tfrac{l^2}{2}+s^2}q\pi)\right)+\left(4\sum_{l=1}^{\infty}\left(\frac{l^2}{(\frac{l^2}{2}+s^2)^2}\right)\right) \\ &-\left(2^{\frac{7}{2}}\pi\sum_{r=1}^{\infty}\sum_{q=-\infty}^{\infty}\left(\frac{\sqrt{2q^2+r^2}}{s}\right)^{\frac{1}{2}} K_{\frac{1}{2}}(2\sqrt{2q^2+r^2}s\pi)\right) \\ &-\left(2^{\frac{15}{4}}\pi\sum_{q=1}^{\infty}\left(\frac{q}{s}\right)^{\frac{1}{2}} K_{\frac{1}{2}}(2^{\frac{3}{2}}qs\pi)\right)-\left(\frac{2^{\frac{3}{2}}\pi}{s}\right) \end{aligned} \tag{4.53}$$

The values for the Bessel function are easily obtained either form mathematical tables or using software such as *Mathematica* from Wolfram Research.

U_{33}

As before, the last term in this case is equal to the last term for U_{11} in (4.44). The first term takes the form

$$\sum_{k=-\infty}^{\infty}\sum_{l=-\infty}^{\infty}\frac{3s^2}{(k^2+\frac{l^2}{2}+s^2)^{\frac{5}{2}}}=\left(\frac{3}{\Gamma(\frac{5}{2})}\int_0^{\infty}\left(\frac{\pi}{t}\right)^{\frac{1}{2}}\left(\frac{2\pi}{t}\right)^{\frac{1}{2}}\sum_{r=-\infty}^{\infty}\sum_{q=-\infty}^{\infty}s^2t^{\frac{3}{2}}e^{-s^2t-(q^2+2r^2)\pi^2/t}dt\right)$$

$$=\left(2^{\frac{11}{2}}\pi^2\sum_{l=1}^{\infty}\sum_{q=1}^{\infty}s^2\left(\frac{\sqrt{2r^2+q^2}}{s}\right)^{\frac{3}{2}}K_{\frac{3}{2}}(2\sqrt{2r^2+q^2}s\pi)\right)+\left(2^{\frac{21}{4}}\pi^2\sum_{r=1}^{\infty}s^2\left(\frac{r}{s}\right)^{\frac{3}{2}}K_{\frac{3}{2}}(2\sqrt{2}rs\pi)\right) \quad (4.54)$$

$$+\left(2^{\frac{9}{2}}\pi^2\sum_{r=1}^{\infty}s^2\left(\frac{q}{s}\right)^{\frac{3}{2}}K_{\frac{3}{2}}(2rs\pi)\right)+2^{\frac{3}{2}}\pi\left(\frac{1}{s}\right)$$

The term U_{33} can the be written as:

$$U_{33}^{nm}=\left(2^{\frac{11}{2}}\pi^2s^{\frac{1}{2}}\sum_{r=1}^{\infty}\sum_{q=1}^{\infty}(2r^2+q^2)^{\frac{3}{4}}K_{\frac{3}{2}}(2\sqrt{2r^2+q^2}s\pi)\right)+\left(2^{\frac{21}{4}}\pi^2s^{\frac{1}{2}}\sum_{r=1}^{\infty}r^{\frac{3}{2}}K_{\frac{3}{2}}(2\sqrt{2}rs\pi)\right)$$

$$+\left(2^{\frac{9}{2}}\pi^2s^{\frac{1}{2}}\sum_{q=1}^{\infty}q^{\frac{3}{2}}K_{\frac{3}{2}}(2qs\pi)\right)+2^{\frac{3}{2}}\pi\left(\frac{1}{s}\right)$$

$$-\left(2^{\frac{7}{2}}\pi\sum_{r=1}^{\infty}\sum_{q=-\infty}^{\infty}\left(\frac{\sqrt{2q^2+r^2}}{s}\right)^{\frac{1}{2}}K_{\frac{1}{2}}(2\sqrt{2q^2+r^2}s\pi)\right) \quad (4.55)$$

$$-\left(2^{\frac{15}{4}}\pi\sum_{q=1}^{\infty}\left(\frac{q}{s}\right)^{\frac{1}{2}}K_{\frac{1}{2}}(2^{\frac{3}{2}}qs\pi)\right)-\left(\frac{2^{\frac{3}{2}}\pi}{s}\right)$$

In this case, the solution contains six terms.

Alternative 1, for in-between plane interaction

In case b) and d) defined by the equations (4.13) and (4.15), we use the same method as above, but with the following transformation:

$$\begin{aligned}k &\to k+\tfrac{1}{2}\\ l &\to l+\tfrac{1}{2}\end{aligned} \quad (4.56)$$

We need to apply the general version of Jacobi's imaginary transform,

$$\sum_{p=-\infty}^{\infty}e^{-(p+a)^2t}=\left(\frac{\pi}{t}\right)^{\frac{1}{2}}\sum_{q=-\infty}^{\infty}e^{-q^2\pi^2/t}\cos 2qa\pi \xrightarrow{a=\frac{1}{2}} \left(\frac{\pi}{t}\right)^{\frac{1}{2}}\sum_{q=-\infty}^{\infty}(-1)^q e^{-q^2\pi^2/t} \quad . \quad (4.57)$$

This leads to the following changes (which we list for reference purposes):

U_{11}

$$
\begin{aligned}
U_{11}^{nm} = & \left(2^{\frac{13}{2}} \pi^2 \sum_{k=0}^{\infty} \sum_{q=1}^{\infty} \cos\left(\sqrt{2} q \pi\right) \left(\frac{(k+\frac{1}{2})q}{\sqrt{(k+\frac{1}{2})^2 + s^2}} \right)^2 K_2(2^{\frac{3}{2}} \sqrt{(k+\frac{1}{2})^2 + s^2}\, q\pi) \right) \\
& + \left(2^{\frac{7}{2}} \sum_{k=0}^{\infty} \left(\frac{(k+\frac{1}{2})^2}{((k+\frac{1}{2})^2 + s^2)^2} \right) \right) \\
& - \left(2^{\frac{7}{2}} \pi \sum_{r=1}^{\infty} \sum_{q=-\infty}^{\infty} \cos\left(\sqrt{2} q \pi\right) (-1)^r \left(\frac{\sqrt{2q^2 + r^2}}{s} \right)^{\frac{1}{2}} K_{\frac{1}{2}}(2\sqrt{2q^2 + r^2}\, s\pi) \right) \\
& - \left(2^{\frac{15}{4}} \pi \sum_{q=1}^{\infty} \cos\left(\sqrt{2} q \pi\right) \left(\frac{q}{s} \right)^{\frac{1}{2}} K_{\frac{1}{2}}(2^{\frac{3}{2}} qs\pi) \right) - \left(\frac{2^{\frac{3}{2}} \pi}{s} \right)
\end{aligned}
\tag{4.58}
$$

U_{22}

$$
\begin{aligned}
U_{22}^{nm} = & \left(16\pi^2 \sum_{l=0}^{\infty} \sum_{q=1}^{\infty} (-1)^q \left(\frac{(l+\frac{1}{2})q}{\sqrt{\frac{(l+\frac{1}{2})^2}{2} + s^2}} \right)^2 K_2(2\sqrt{\frac{(l+\frac{1}{2})^2}{2} + s^2}\, q\pi) \right) \\
& + \left(4 \sum_{l=0}^{\infty} \left(\frac{(l+\frac{1}{2})^2}{(\frac{(l+\frac{1}{2})^2}{2} + s^2)^2} \right) \right) \\
& - \left(2^{\frac{7}{2}} \pi \sum_{r=1}^{\infty} \sum_{q=-\infty}^{\infty} \cos(\sqrt{2} q \pi) (-1)^r \left(\frac{\sqrt{2q^2 + r^2}}{s} \right)^{\frac{1}{2}} K_{\frac{1}{2}}(2\sqrt{2q^2 + r^2}\, s\pi) \right) \\
& - \left(2^{\frac{15}{4}} \pi \sum_{q=1}^{\infty} \cos(\sqrt{2} q \pi) \left(\frac{q}{s} \right)^{\frac{1}{2}} K_{\frac{1}{2}}(2^{\frac{3}{2}} qs\pi) \right) - \left(\frac{2^{\frac{3}{2}} \pi}{s} \right)
\end{aligned}
\tag{4.59}
$$

U_{33}

$$
\begin{aligned}
U_{33}^{nm} = &\left(2^{\frac{11}{2}}\pi^2 s^{\frac{1}{2}}\sum_{r=1}^{\infty}\sum_{q=1}^{\infty}\cos(\sqrt{2}r\pi)(-1)^q\left(2r^2+q^2\right)^{\frac{3}{4}}K_{\frac{3}{2}}(2\sqrt{2r^2+q^2}s\pi)\right)\\
&+\left(2^{\frac{21}{4}}\pi^2 s^{\frac{1}{2}}\sum_{r=1}^{\infty}\cos(\sqrt{2}r\pi)r^{\frac{3}{2}}K_{\frac{3}{2}}(2\sqrt{2}rs\pi)\right)\\
&+\left(2^{\frac{9}{2}}\pi^2 s^{\frac{1}{2}}\sum_{q=1}^{\infty}(-1)^q q^{\frac{3}{2}}K_{\frac{3}{2}}(2qs\pi)\right)+2^{\frac{3}{2}}\pi\left(\frac{1}{s}\right)\\
&-\left(2^{\frac{7}{2}}\pi\sum_{r=1}^{\infty}\sum_{q=-\infty}^{\infty}\cos(\sqrt{2}q\pi)(-1)^r\left(\frac{\sqrt{2q^2+r^2}}{s}\right)^{\frac{1}{2}}K_{\frac{1}{2}}(2\sqrt{2q^2+r^2}s\pi)\right)\\
&-\left(2^{\frac{15}{4}}\pi\sum_{q=1}^{\infty}\cos(\sqrt{2}q\pi)\left(\frac{q}{s}\right)^{\frac{1}{2}}K_{\frac{1}{2}}(2^{\frac{3}{2}}qs\pi)\right)-\left(\frac{2^{\frac{3}{2}}\pi}{s}\right)
\end{aligned}
\tag{4.60}
$$

Alternative 1, for in-plane interaction, $s = 0$

The deduction above is not valid for dipole-dipole in-plane interaction (case $s = 0$), because the summation does not include the point $(k\,,\,l\,) = (0,0)$.

U_{11}

The sum to be calculated is now of the form

$$
\begin{aligned}
&\sum_{k=-\infty}^{\infty}\sum_{l=-\infty}^{\infty}\left(\frac{3k^2}{\left(k^2+\frac{l^2}{2}\right)^{\frac{5}{2}}}-\frac{1}{\left(k^2+\frac{l^2}{2}\right)^{\frac{3}{2}}}\right)\Bigg|_{(k,l)\neq(0,0)}\\
&=\left(\frac{1}{\Gamma(5/2)}\int_0^{\infty}\sum_{k=-\infty}^{\infty}\sum_{l=-\infty}^{\infty}3k^2t^{\frac{3}{2}}e^{-(k^2+\frac{l^2}{2})t}dt\right)-\left(\frac{1}{\Gamma(3/2)}\int_0^{\infty}\sum_{k=-\infty}^{\infty}\sum_{l=-\infty}^{\infty}t^{\frac{1}{2}}e^{-(k^2+\frac{l^2}{2})t}dt\right)\Bigg|_{(k,l)\neq(0,0)}
\end{aligned}
\tag{4.61}
$$

It is possible to split each term as before, and for the $U_{11}{}^0$ coefficient we get

$$
\begin{aligned}
U_{11}^0 = &\left(\frac{8}{3\sqrt{\pi}}\int_0^{\infty}\sum_{k=1}^{\infty}\sum_{l=-\infty}^{\infty}3k^2t^{\frac{3}{2}}e^{-(k^2+\frac{l^2}{2})t}dt\right)\\
&-\left(\frac{4}{\sqrt{\pi}}\int_0^{\infty}\sum_{k=1}^{\infty}\sum_{l=-\infty}^{\infty}t^{\frac{1}{2}}e^{-(k^2+\frac{l^2}{2})t}dt\right)-\left(\frac{2}{\Gamma(3/2)}\int_0^{\infty}\sum_{l=1}^{\infty}t^{\frac{1}{2}}e^{-\frac{l^2}{2}t}dt\right)\\
&=2^{\frac{11}{2}}\sum_{k=1}^{\infty}\sum_{q=1}^{\infty}k^2\left(\frac{\sqrt{2}q\pi}{k}\right)^2K_2\left(2^{\frac{3}{2}}qk\pi\right)+2^{\frac{7}{2}}\sum_{k=1}^{\infty}k^{-2}\\
&-2^5\pi\sum_{k=1}^{\infty}\sum_{q=1}^{\infty}\left(\frac{q}{k}\right)K_1\left(2^{\frac{3}{2}}qk\pi\right)-2^{\frac{5}{2}}\sum_{k=1}^{\infty}k^{-2}-2^{\frac{5}{2}}\sum_{l=1}^{\infty}l^{-3}
\end{aligned}
\tag{4.62}
$$

We get twice as many terms for the in-plane interaction as for the out-of-plane interaction in (4.51), and question may be asked about the efficiency of applying this transformation. Note, however, that the direct summation for the in-plane interaction converges most slowly of all the series.

U_{22}

Similar to the U_{11} case we get:

$$\begin{aligned} U_{11}^{nm} &= \left(\frac{8}{3\sqrt{\pi}}\int_0^\infty \sum_{l=1}^{\infty}\sum_{k=-\infty}^{\infty} \tfrac{3}{2} l^2 t^{\frac{3}{2}} e^{-(k^2+\frac{l^2}{2})t}\,dt\right) \\ &-\left(\frac{4}{\sqrt{\pi}}\int_0^\infty \sum_{k=1}^{\infty}\sum_{l=-\infty}^{\infty} t^{\frac{1}{2}} e^{-(k^2+\frac{l^2}{2})t}\,dt\right)-\left(\frac{2}{\Gamma(3/2)}\int_0^\infty \sum_{l=1}^{\infty} t^{\frac{1}{2}} e^{-\frac{l^2}{2}t}\,dt\right) \\ &= 32\pi^2\sum_{l=1}^{\infty}\sum_{q=1}^{\infty} q^2 K_2\left(2^{\frac{1}{2}} ql\pi\right)+16\sum_{l=1}^{\infty} l^{-2} \\ &-2^5\pi\sum_{k=1}^{\infty}\sum_{q=1}^{\infty}\left(\frac{q}{k}\right)K_1\left(2^{\frac{3}{2}} qk\pi\right)-2^{\frac{5}{2}}\sum_{k=1}^{\infty} k^{-2}-2^{\frac{5}{2}}\sum_{l=1}^{\infty} l^{-3} \end{aligned} \tag{4.63}$$

U_{33}

The zz-component is just the three last terms if the above sum:

$$\tilde{U}_{33}^{nm} = \sum_{\substack{k=-\infty \\ (k,l)\neq(0,0)}}^{\infty}\sum_{l=-\infty}^{\infty} -\frac{1}{\left(k^2+\frac{l^2}{2}\right)^{\frac{3}{2}}} = -2^5\pi\sum_{k=1}^{\infty}\sum_{q=1}^{\infty}\left(\frac{q}{k}\right)K_1\left(2^{\frac{3}{2}} qk\pi\right)-2^{\frac{5}{2}}\sum_{k=1}^{\infty} k^{-2}-2^{\frac{5}{2}}\sum_{l=1}^{\infty} l^{-3}\,. \tag{4.64}$$

Alternative 2

We now have enough information to calculate all the necessary dipole-dipole interaction coefficients. However the procedure of van der Hoff and Benson contains several degrees of freedom when choosing what transformations to apply. In particular, this is true for Jacobi's imaginary transformation, (4.57). To illustrate this, and to utilize the advantage of being able to compare independent results, we look at an alternative approach.

We will be looking at U_{11}, and use Euler's definition of the gamma function to get

$$\sum_{k=-\infty}^{\infty}\sum_{l=-\infty}^{\infty}\left(\frac{3k^2}{(k^2+\frac{l^2}{2}+s^2)^{\frac{5}{2}}}-\frac{1}{(k^2+\frac{l^2}{2}+s^2)^{\frac{3}{2}}}\right) \qquad (4.65)$$
$$=\left(\frac{1}{\Gamma(5/2)}\int_0^{\infty}\sum_{k=-\infty}^{\infty}\sum_{l=-\infty}^{\infty}3k^2t^{\frac{3}{2}}e^{-(k^2+\frac{l^2}{2}+s^2)t}dt\right)-\left(\frac{1}{\Gamma(3/2)}\int_0^{\infty}\sum_{k=-\infty}^{\infty}\sum_{l=-\infty}^{\infty}t^{\frac{1}{2}}e^{-(k^2+\frac{l^2}{2}+s^2)t}dt\right)$$

These sums are first transformed with the help of the definition of the gamma function (4.43) as before. Now, instead of using the Jacobi transform (4.57) on both the k and l sums above, as we did before on page 66, it is only applied to the sum over l,

$$U_{11}^{nm}=\left(\frac{1}{\Gamma(\frac{5}{2})}\int_0^{\infty}\left(\frac{2\pi}{t}\right)^{\frac{1}{2}}\sum_{k=-\infty}^{\infty}\sum_{q=-\infty}^{\infty}3k^2t^{\frac{3}{2}}e^{-(k^2+s^2)t-2q^2\pi^2/t}dt\right)$$
$$-\left(\frac{1}{\Gamma(\frac{3}{2})}\int_0^{\infty}\left(\frac{2\pi}{t}\right)^{\frac{1}{2}}\sum_{k=-\infty}^{\infty}\sum_{q=-\infty}^{\infty}t^{\frac{1}{2}}e^{-(k^2+s^2)t-2q^2\pi^2/t}dt\right) \qquad (4.66)$$
$$=\sqrt{2\pi}\int_0^{\infty}\sum_{k=-\infty}^{\infty}\sum_{q=-\infty}^{\infty}\left(\frac{3k^2t}{\Gamma(\frac{5}{2})}-\frac{1}{\Gamma(\frac{3}{2})}\right)e^{-(k^2+s^2)t-2q^2\pi^2/t}dt$$

These sums are split up and thereafter transformed with the help of (4.48). Numerical values for the gamma function are then substituted, and simplifying the result one obtains

$$U_{11}^{nm}=2^{\frac{13}{2}}\pi^2\sum_{k=1}^{\infty}\sum_{q=1}^{\infty}\left(\frac{kq}{\sqrt{k^2+s^2}}\right)^2K_2\left(2^{\frac{3}{2}}\sqrt{k^2+s^2}q\pi\right)$$
$$-32\pi\sum_{k=1}^{\infty}\sum_{q=1}^{\infty}\left(\frac{q}{\sqrt{k^2+s^2}}\right)K_1\left(2^{\frac{3}{2}}\sqrt{k^2+s^2}q\pi\right) \qquad (4.67)$$
$$-16\pi\sum_{q=1}^{\infty}\left(\frac{q}{s}\right)K_1\left(2^{\frac{3}{2}}sq\pi\right)+2^{\frac{5}{2}}\sum_{k=1}^{\infty}\left(\frac{k^2-s^2}{(k^2+s^2)^2}\right)-\frac{2^{\frac{3}{2}}}{s^2}$$

Numerical results for these dipolesums are given in Appendix E, and are equal to those calculated by alternative 1, and by the Hankel transformation in Section 4.2.

4.4 Solving the dipole matrix equation

As the U-coefficients are calculated, we proceed by solving equation (4.9) for p_n. The external field E_0 can be found by noting that the dipole moment of the bulk p_B is given by a similar relation as (4.9):

$$\vec{p}_B=\alpha(\vec{E}_0+\frac{1}{4\pi\varepsilon_0}\sum_{m=-\infty}^{\infty}\vec{U}^{nm}\vec{p}_B) \qquad (4.68)$$

$$
\begin{pmatrix}
1-\alpha U_x^{00}-\alpha U_x^{00}\left(\dfrac{\varepsilon_g-1}{\varepsilon_g+1}\right) & & \cdots & & -\alpha U_x^{04}-\alpha U_x^{04}\left(\dfrac{\varepsilon_g-1}{\varepsilon_g+1}\right) \\
& 1-\alpha U_x^{11}-\alpha U_x^{11}\left(\dfrac{\varepsilon_g-1}{\varepsilon_g+1}\right) & & & \\
\vdots & & 1-\alpha U_x^{22}-\alpha U_x^{22}\left(\dfrac{\varepsilon_g-1}{\varepsilon_g+1}\right) & & \vdots \\
& & & 1-\alpha U_x^{33}-\alpha U_x^{33}\left(\dfrac{\varepsilon_g-1}{\varepsilon_g+1}\right) & \\
-\alpha U_x^{40}-\alpha U_x^{40}\left(\dfrac{\varepsilon_g-1}{\varepsilon_g+1}\right) & & \cdots & & 1-\alpha U_x^{44}-\alpha U_x^{44}\left(\dfrac{\varepsilon_g-1}{\varepsilon_g+1}\right)
\end{pmatrix}
\begin{pmatrix}
\tilde{p}_{x0} \\ \tilde{p}_{x1} \\ \tilde{p}_{x2} \\ \tilde{p}_{x3} \\ \tilde{p}_{x4}
\end{pmatrix}
$$

$$
=\begin{pmatrix}
1-\alpha U_x^{00}-2\alpha U_x^{01}-2\alpha U_x^{02} \\
1-\alpha U_x^{11}-2\alpha U_x^{12}-2\alpha U_x^{13} \\
1-\alpha U_x^{22}-2\alpha U_x^{23}-2\alpha U_x^{24} \\
1-\alpha U_x^{33}-2\alpha U_x^{34}-2\alpha U_x^{35}+\alpha U_x^{45} \\
1-\alpha U_x^{44}-2\alpha U_x^{45}-2\alpha U_x^{46}+\alpha U_x^{45}+\alpha U_x^{46}
\end{pmatrix} \tag{4.77}
$$

From this equation, $\tilde{p}$ can be found by inverting the 5x5 matrix.

4.5 Spectrum calculational procedure

The RAS curve is calculated as follows:

1. Check whether it is reasonable to describe the surface as a lattice of polarisable entities surrounded by a Drude electron gas.
2. Find a suitable dielectric function data set and calculate the plasma frequency ω_p and the relaxation time τ.
3. Select a reasonable effective surface height d, and get the appropriate plane-wise dipole-dipole interaction coefficients.
4. Use the Clausius-Mosotti relation,

$$\frac{\varepsilon - \varepsilon_{Drude}}{\varepsilon + 2\varepsilon_{Drude}} = \frac{n\alpha}{3\varepsilon_0}, \tag{4.78}$$

   to obtain the polarisability α for the bulk. Here, n is the number density of ions, ε is the bulk dielectric function and ε_{Drude} is the permittivity of the electron gas. Assume that the polarisability for the bulk is unchanged as one approach the surface.
5. For each crystallographic direction, and for each frequency ω, invert the matrix equation (4.77) to find numerical values for the normalised dipoles in the 3-7 topmost lattice planes.
6. With the use of (4.2), calculate the surface conductivity σ in the two directions.
7. The complex-valued reflection anisotropy spectrum is then obtained from (4.1).

4.6 Example: Ag(110)

A metal that fulfils these criteria of the Swiss cheese model is silver. A theoretical local-field effect spectrum for the (110) surface of this noble metal with $d = 2^{-5/2}a$ has been published by Borensztein *et al* [20], and we can therefore check our calculation by comparing with their result.

We use the standard dielectric function data for silver by Johnson and Christy [21]. By a linear fit of the low-energy real part of the dielectric function the plasma frequency is found to be $\omega_p = 9.17$ eV. Similarly, a linear fit of the low-energy imaginary part of the dielectric function gives the relaxation time $\tau = 31 \cdot 10^{-15}$ s. After solving the coupled set of equations, (4.76), we find the normalised dipole moments close to the surface. In Figure 4.3, the $[\bar{1}10]$ and [001] components of the dipole moment of the atoms in the top lattice plane is plotted as a function of photon energy. In the area 3.7 eV- 3.9 eV, near the intraband transition threshold, both components have a strong resonance. The normalised dipole moment in the $[\bar{1}10]$ direction at the energy (3.74 eV), corresponding to the maximum value of the resonance, is plotted as a function of depth in Figure 4.4. It is seen that even at this resonance value, the dipole moment reaches the bulk value within 3-4 lattice planes.

The next step is to calculate the surface conductivity. The surface conductivity can be defined as the relation between the excess surface electric current density and the electric field at the surface,

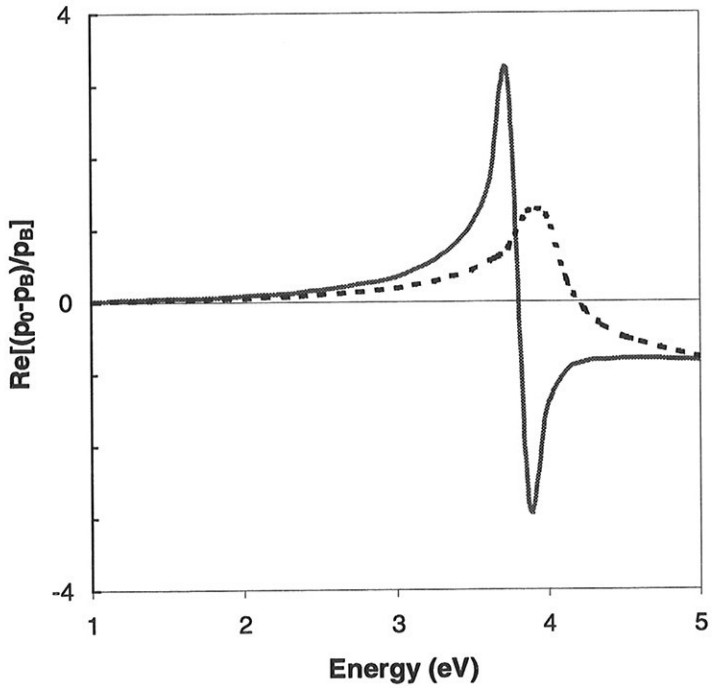

Figure 4.3. Real part of the normalised dipole moments (deviation from bulk value) of the top layer of the Ag(110) surface. Solid line: [110] component, broken line: [001] component.

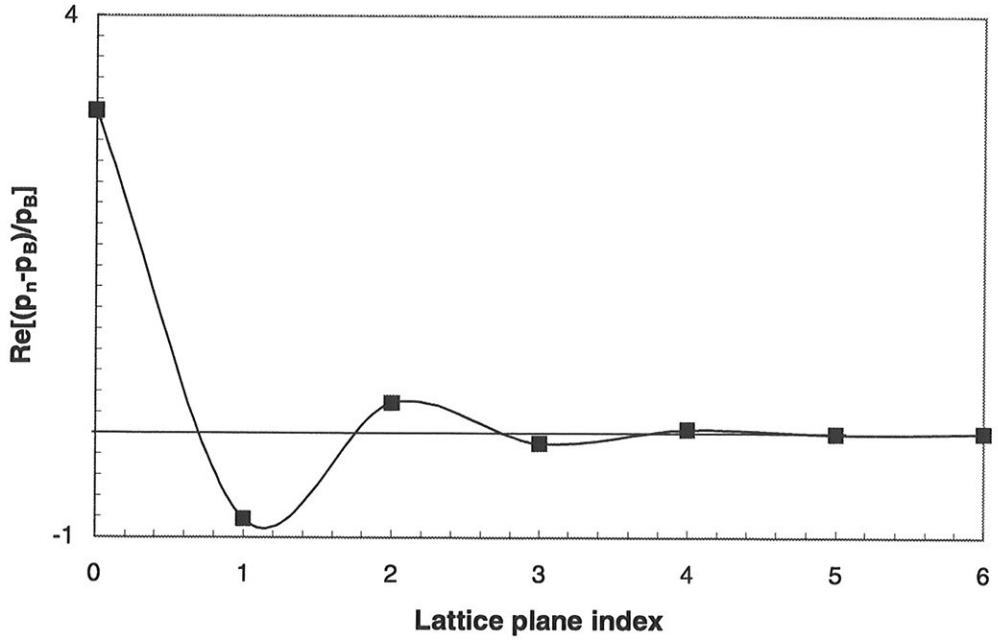

Figure 4.4. Normalised dipole moment (deviation from bulk value) for the topmost lattice planes (the $[\bar{1}10]$ component).

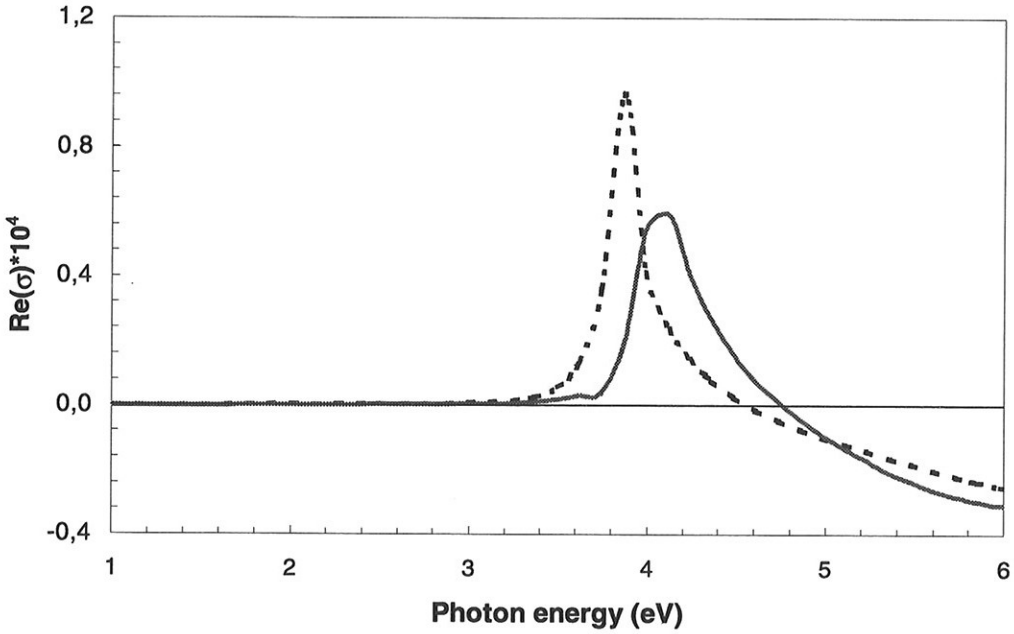

Figure 4.5. Surface conductivity for Ag(110). Solid line: [110] component, broken line: [001] component.

$$\vec{\sigma}\,\vec{E} = \int_0^\infty d\eta\, \Delta\vec{j}(\eta)\ , \tag{4.79}$$

where $\Delta j(\eta)$ is the deviation in current density from the bulk value. The surface conductivity for Ag(110), calculated with the use of (4.2), is shown in Figure 4.5. Note that since the surface conductivity by (4.2) is given as a plane-wise sum over normalised dipole moments, it is possible to define a surface conductivity for plane n, i.e. σ_n. The total surface conductivity is then

$$\vec{\sigma} = \sum_{n=0}^{\infty} \vec{\sigma}_n\ . \tag{4.80}$$

The surface conductivity as a function of the lattice plane could be plotted in a similar manner as the dipole moments in Figure 4.4, corresponding to a charge sheet model.

The theoretical reflection anisotropy spectrum can be obtained from (4.1). The real part is shown in Figure 4.6. There is one a double-peak resonance at 3.8 eV. Compared to other noble metals, the signal is strong, close to 2%. The imaginary part is also strong, and is shown in Figure 4.7. In Chapter 5 the origin of the resonance will be discussed together with comparison to measured values.

4.7 Sensitivity to dielectric input parameters

It is interesting to examine how the dielectric input parameters affect the resulting reflection anisotropy spectra. This is especially true for silver since the dielectric data from Johnson and Christy [21] contains only five points in energy range of the double peak shown in Figure 4.6. Therefore, we have made a comparison with calculations based on two other data sets, both with significantly more data points. The result is plotted in Figure 4.8. It is seen from this figure that the data set of Johnson and Christy is too sparse to accurately predict the maximum and minimum values and the height of the peek, but the form of the resonance curve is close to correct. Interpolation is clearly necessary.

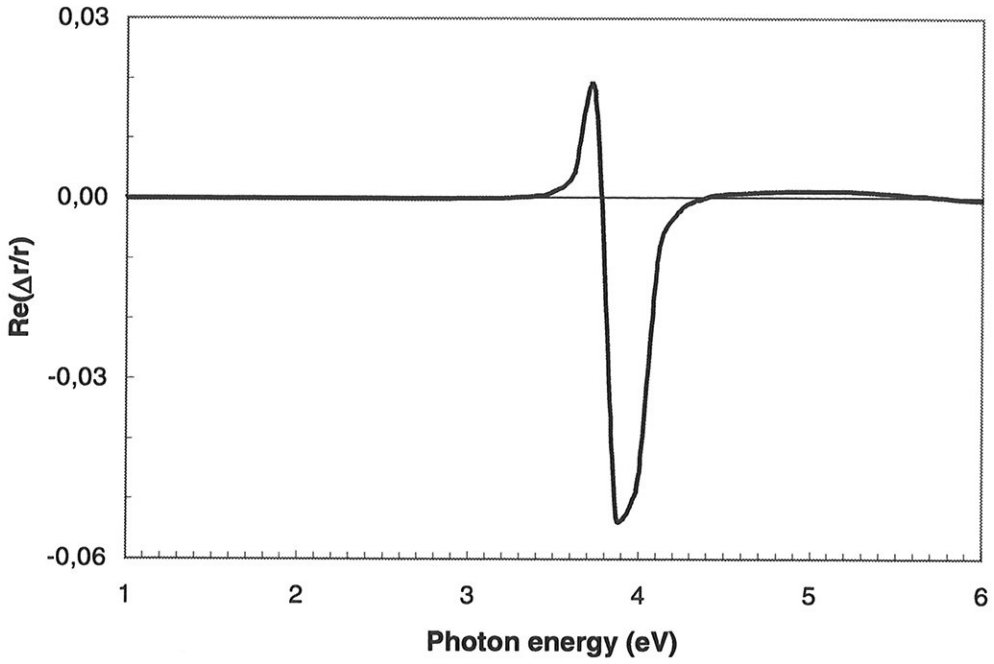

Figure 4.6. Real part of the reflection anisotropy spectrum for Ag(110).

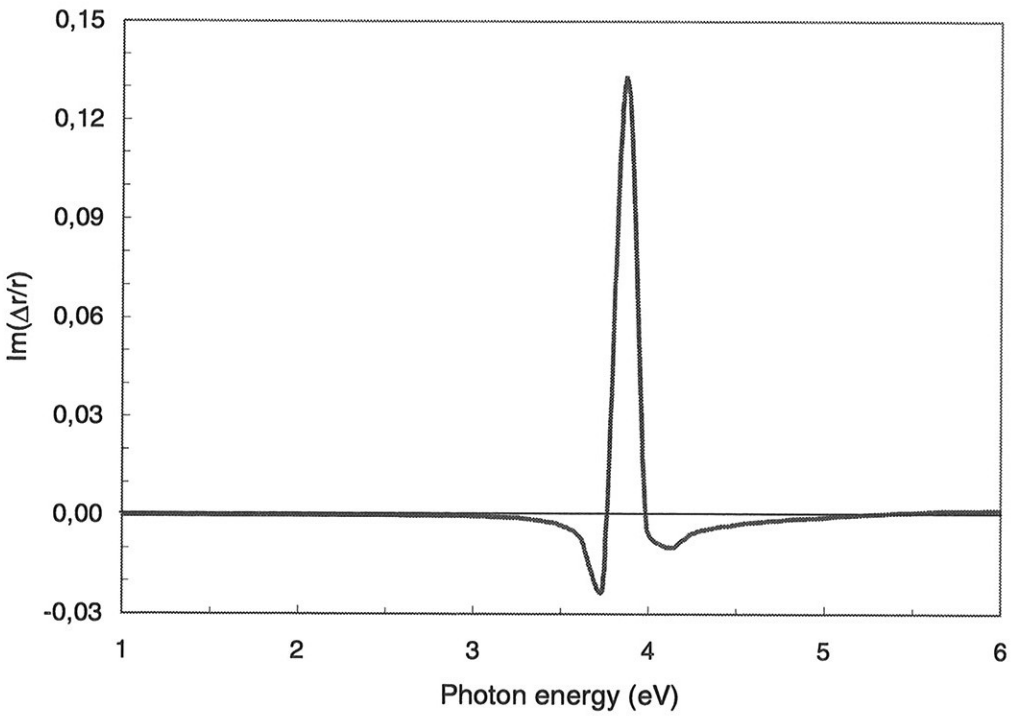

Figure 4.7. Imaginary part of the reflection anisotropy spectrum for Ag(110).

The strong RAS signal in the range 3.7 - 4.0 eV is caused by two effects. Firstly, the resonance is shifted by the local-field effect to the plasma frequency region where dissipation is low. The surface conductivity is therefore large, and if a difference exists between the two crystallographic axes, the resulting RAS signal will also be large. Secondly, the very low reflectivity of silver around 3.9 eV enhances the signal from the surface. The low reflectivity makes it difficult to predict the strength of the double-peak. A small offset error either in the dielectric data or in the measured reflectivity can increase or reduce the calculated peaks by one magnitude. The same is true for the *measured* reflection anisotropy data in this energy range: Bandwidth of monochromators, light-detector offset, contamination and surface defects can all strongly influence the strength of the individual peaks.

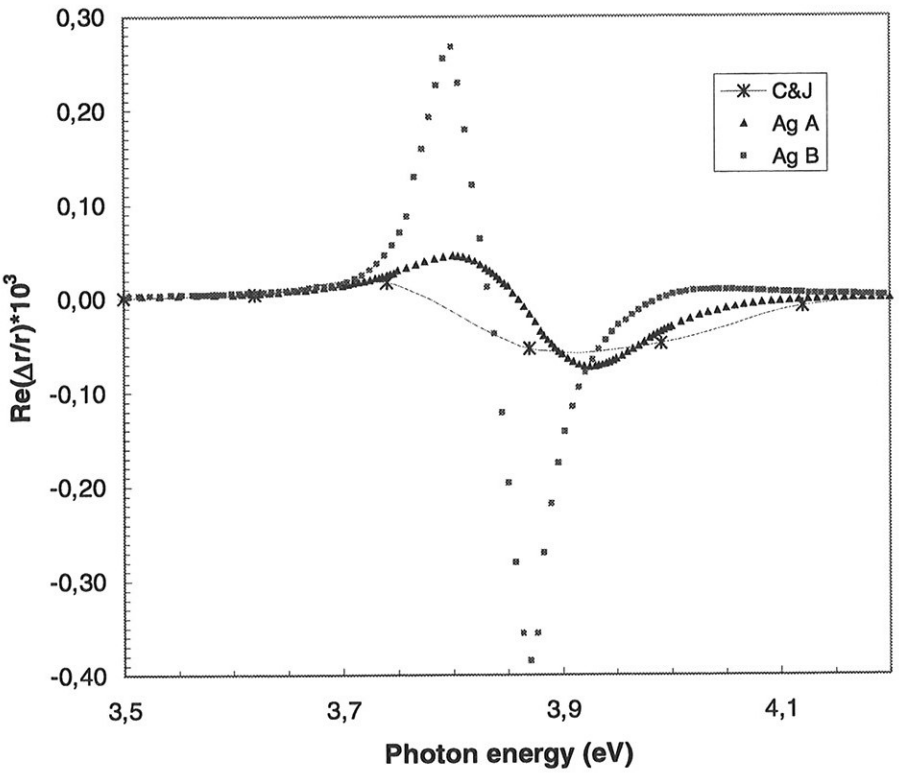

Figure 4.8. Variation in the calculated RA spectra with respect to separate dielectric data sets (Johnson and Christy (J&C), Ag A [86], Ag B [86]).

Within certain limits we are free to select values for the plasma frequency ω_p and the relaxation time τ. For noble metals, the best way to get reasonable and useful values for these parameters is, for each calculation, to fit a Drude dielectric function to the low energy part of the dielectric data. However, even with this method, the actual value may vary considerably depending on how the best fit is calculated. In Figure 4.9, the calculated reflection anisotropy spectra of Ag(110) (data set Ag A), is shown for different values of the plasma frequency. The plasma frequencies are all in the range of reasonable values from a best-fit calculation. There is a small shift in the zero crossing of the RAS curve towards higher energies as the plasma frequency increases from 8 to 10 eV. In addition, the strength of the peaks increase, and the ratio between them approaches unity.

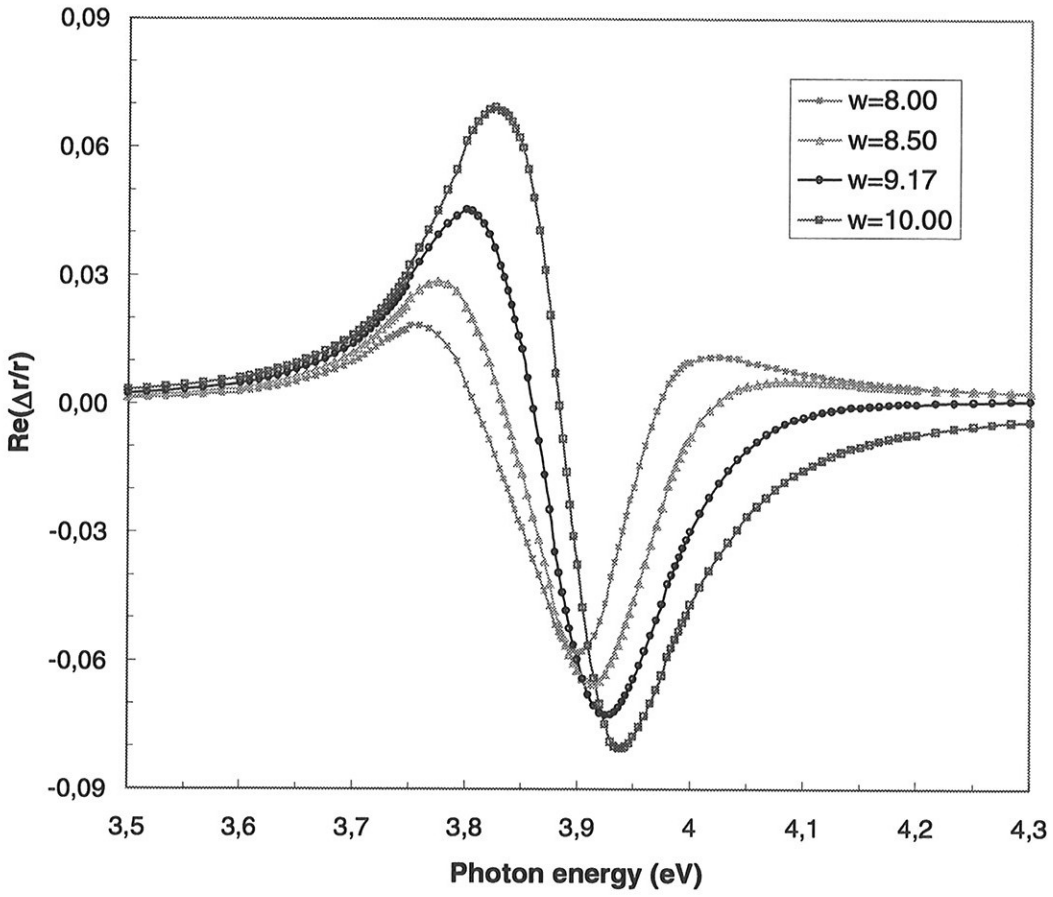

Figure 4.9. Real part of RAS of Ag(110) for different values of the plasma frequency energy $w=\hbar\omega_p$.

4.8 Variation in the effective surface height

A possible improvement in the calculations is to replace the abrupt electronic surface at half the interplanar distance from the top layer with a more realistic surface profile. As a first step we modify the effective surface height d. For example, the effective surface $d_{\parallel}$ in (1.19) could be used in our model. The important question for our model is at what effective surface height d the mirroring of the ion-core dipoles takes place.

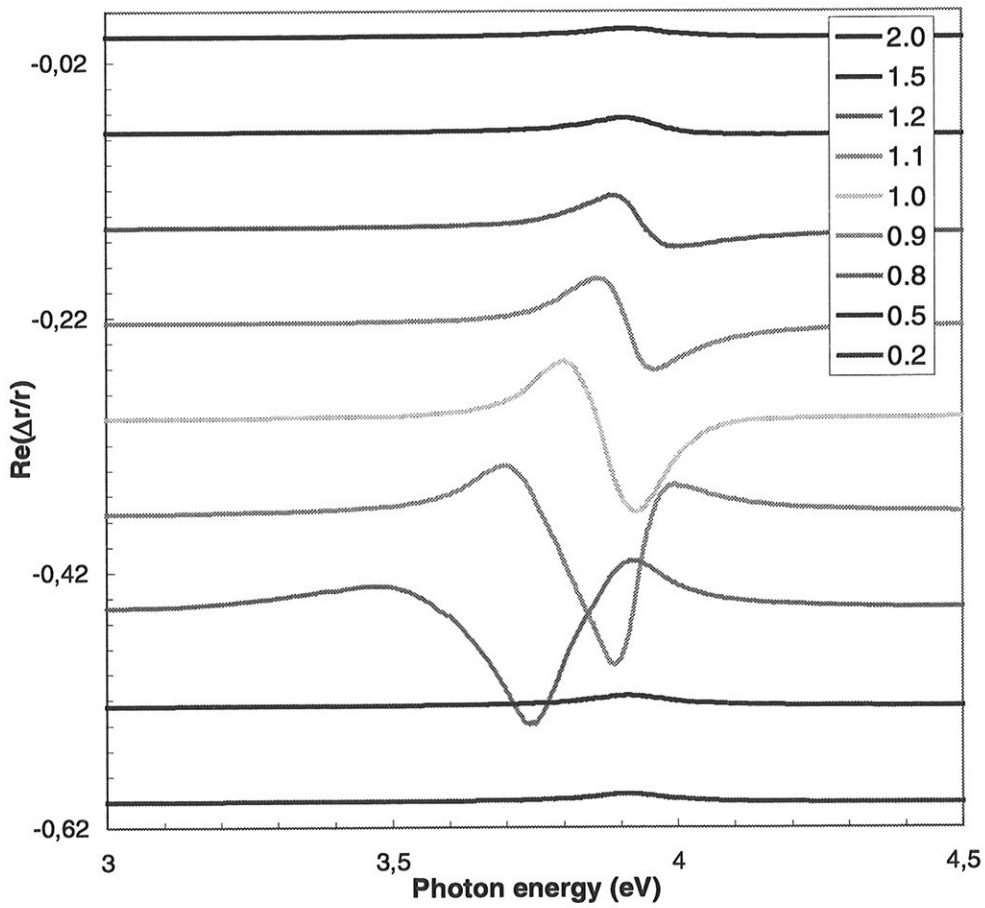

Figure 4.10. Calculated RAS of Ag(110) as a function of effective surface height d. The range of d is from 0.2 – 2.0 the original value. The curves are shifted vertically for clearity.

To investigate the effect of d on the Ag(110) RAS spectra, we go back to the definition of the lattice vectors for interaction between a plane and an image plane, (4.14) and (4.15). Of course, d only affects the z-component r_{ijz} of these vectors. Moreover, the interplanar distance s is only a parameter in the final expressions, for example in (4.40) and (4.58). For each new value of d we have to evaluate the series given by these expressions to get the new set of U-coefficients. Some results are given in Appendix E. In Figure 4.10, the real part of the reflection anisotropy for silver is shown for several d values. It is seen that the effective surface height probably lies in the range 0.8-1.2 times half the interplanar distance, as the other curves do not match the measured spectra. In addition, it is clear that relaxation effects are important for our model calculations.

4.9 Surface defects

A part of the standard procedure to clean surfaces in vacuum is to bombard the surfaces with ions of noble gases like xenon. At a given temperature, the mobility of the surface atoms is sufficient to repair some of the damages. Typically the sample is heated for some time after sputtering to further heal the surface (annealing). After sputtering, but before annealing, the lattice is distorted and contains vacancies and other defects in the top layers. One way to include these effects in the calculations is to introduce an *effective* plane-wise dipole-dipole interaction coefficient $f_m \cdot U_{nm}$, where f_m is a defect factor.

Consider as an example a situation where a certain fraction of the lattice sites is unoccupied. The average interaction strength between dipoles in the top plane and dipoles in deeper layers will be reduced. The reduction depends on the distribution and the number of unoccupied sites. The defect factor will therefore be less than unity, $f_0<1$ and $f_{0'}<1$. Furthermore, if nearly all atoms in the top layer are missing it is reasonable to remove that lattice plane from the model, and define the next layer as the top layer. In this case, the average interaction is characterised by a defect factor larger than unity $f_0>1$ and $f_{0'}>1$. All other defect factors are unity in both cases. The effect on the silver spectrum is indicated by the curves in Figure 4.11. As the defect factor changes from 2 to 0.2 there is a 0.2 eV shift in energy for the zero crossing of the two-peaked structure. In addition, the profile of the resonance is modified.

4.10 Possible improvements

The local-field effect theory based on the Swiss cheese model has proven to reproduce many of the measured reflection anisotropy spectra of noble metals. Still, it is of interest to improve the calculations, in particular to deal with reconstructed and stepped surfaces.

Clearly, the electronic charge distribution at the surface should be described by a more realistic profile. In fact, the model as it is now resembles in many ways an oxygen-covered surface, where one would expect the electron distribution at the surface to be step-like.

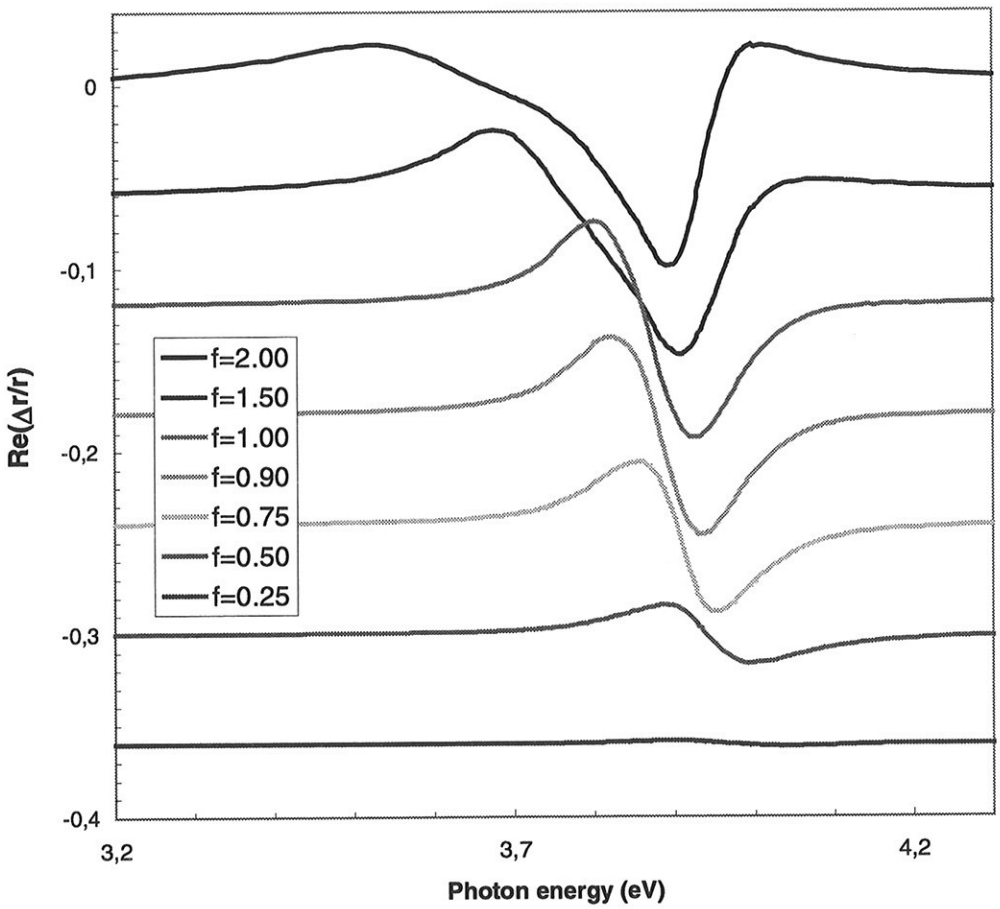

Figure 4.11. The effect of an imperfect top layer on the RAS of Ag(110). The curves are shifted vertically for clarity.

The introduction of effective U-coefficient in Section 4.9 could also be applied to the (1x2) or (2x1) reconstructed surfaces of the 'missing row' type. Alternatively, one could try to solve the exact set of equations for the reconstructed surface. The resulting model is illustrated in Figure 4.12. It is easily seen that all coefficients describing the interaction on a dipole in a plane m from all dipoles in plane $n = 0$ and $n'=0$ are changed, and thus have to be recalculated. This will work for the y-component. However, from the dipole-dipole interaction (4.4) it is seen that there is a coupling between the different components of the dipoles. In other words, the x-component of the dipole moment p_n depends on the x,y and z-component of another dipole p_m. For the (1x1) surface, the symmetric summation over k and l made all off-diagonal components of $\vec{U}$ in (4.17) equal to zero. At the (1x2) missing row surface, the symmetry is broken, and U_{13} and U_{31} is non-zero. Therefore, in every lattice plane, atoms a and b in Figure 4.12 can have different dipole moments, as a result of the missing atoms in the top layer. We may divide each plane in two mathematically separate planes consisting of dipoles of type a and type b respectively. The 7x7 matrix equation (4.77) will then transform

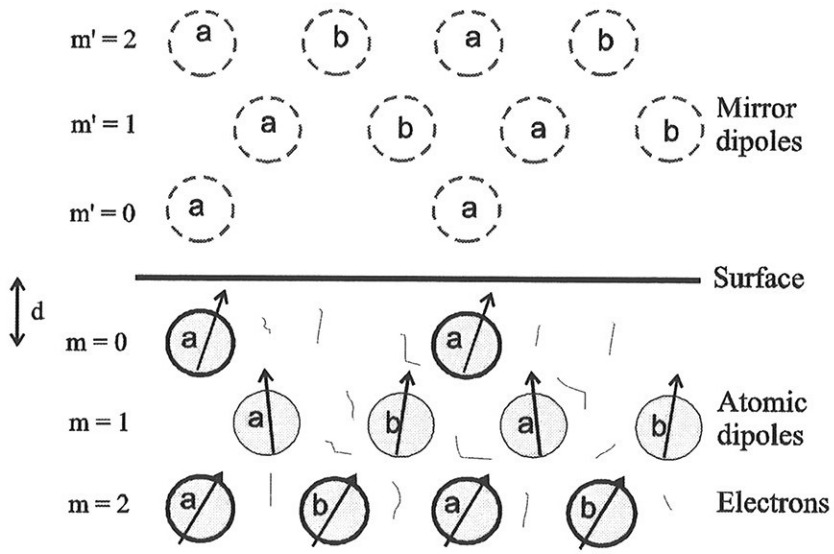

Figure 4.12. The (1x2) fcc Swiss cheese model. Note that atomic dipoles in plane m=1 and m'=1 are positioned behind the others in this cross section.

into a 14x14 matrix equation. Taking into account the x-z coupling, we need to solve 28x28 matrix equation to get the reflection anisotropy spectra, with additional problems concerning the border conditions.

5 Results

The experimental and theoretical results presented here include results for Ag(110), Cu(110), Au(110), Ni(110), Au(100) and Pt(100). The first three sections are reworked version of published papers [30][43][44], the fourth section is a paper in print [89], while the three last sections are results to be published in the future. This is the reason why the sections in this chapter have a different format than rest of the thesis. Note that results on nickel are included even though it is not a noble metal.

5.1 The electronic structure of Cu(110) and Ag(110) surfaces studied by reflection anisotropy spectroscopy

Summary

Experimental curves for the normalised azimuthal reflection difference $\Delta r/r$ for clean and oxygen reconstructed Cu(110) and Ag(110) between 1.5 and 5.5 eV are presented. The copper spectra contain resonances at 2.1 eV and around 4 eV. Using expressions for the screened dipole-dipole interaction we have found that the surface local-field effect and polarisation dependent transitions between surface states at the $\overline{Y}$ point of the surface Brillouin zone are responsible for the main features in the spectra. In the silver spectra there is a resonance at 1.7 eV originating from polarisation dependent transitions between surface states. The changes in the signals upon formation of ordered oxygen overlayers Cu(110)(2x1)-O and Ag(110)(2x1)-O are discussed.

Introduction

The electronic structure of metal surfaces is of fundamental interest in a number of contexts ranging from chemisorption processes to corrosion and the formation of overlayers. Until recently, probing of surface electronic structure has usually been accomplished by photoemission spectroscopy. Optical spectroscopy has not been considered suitable for surface studies due to the large penetration depth of photons, which implies low surface sensitivity. Recently, however, an optical technique with extremely high surface sensitivity has been developed; *reflection anisotropy spectroscopy* (RAS) [8]. RAS measures the complex normal incidence reflection difference between two orthogonal directions in the surface region of a sample. The signal is normalised to the average reflectivity. The technique

The RAS signal for the (2x1)-O reconstructed Cu(110) surface is shown in Figure 5.1 as well as the Cu(110) surface after exposure to air. Clearly the strength of the peak at 2.1 eV is reduced in both cases. It is interesting to note that the remaining part resembles the curve-

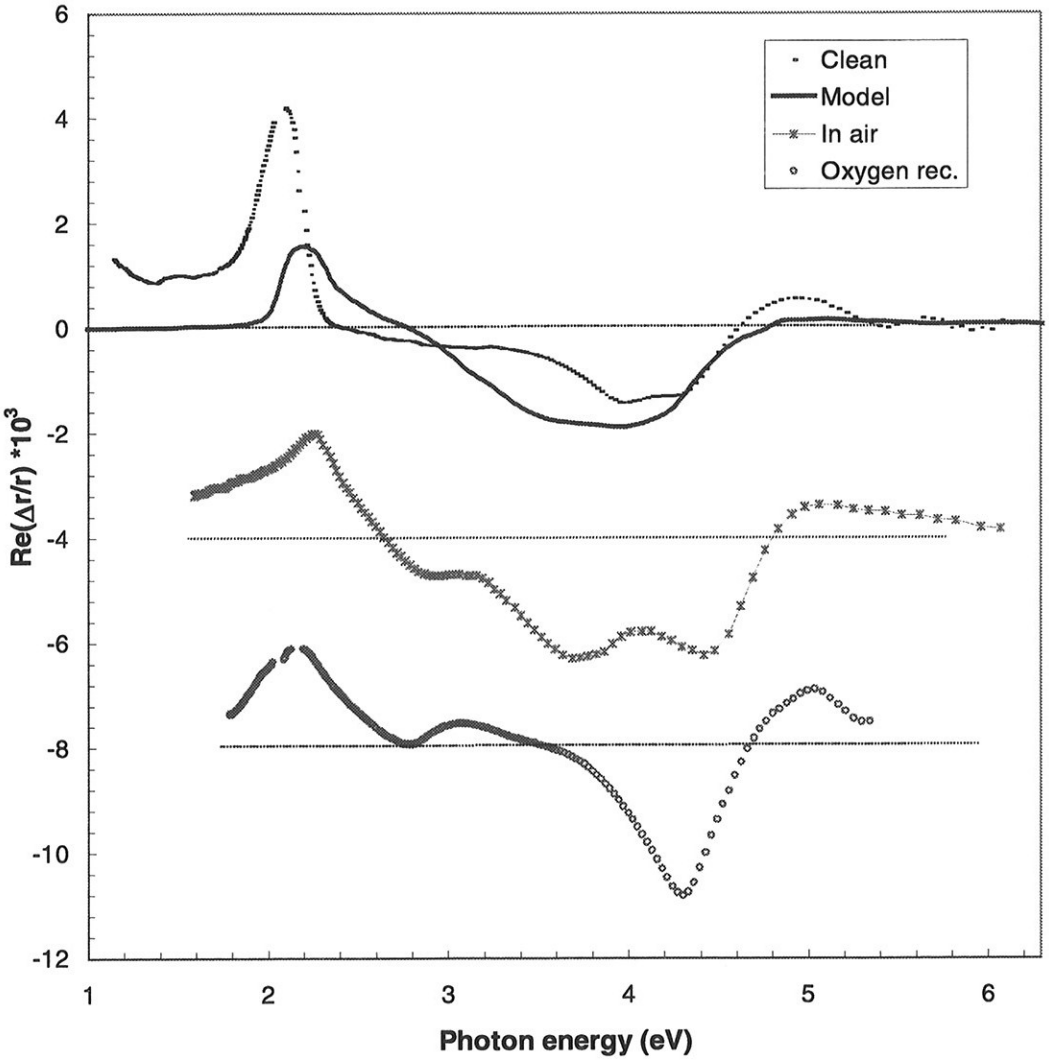

Figure 5.1. Experimental RAS spectra for the clean Cu(110) surface (dots), air exposed Cu(110) surface (stars), and oxygen reconstructed Cu(110) (2x1)-O surface (circles). The solid line shows the result from the local-field calculations. (For the sake of clarity the curves for the air and oxygen exposed surface have been shifted downwards.)

profile predicted bye local-field calculations. The feature at 2.1 eV has previously been observed by Hofmann *et al.*[23], and they assigned it purely to transitions between surface states. As noted by Jiang *et al.* [25], the occupied surface states near the $\overline{Y}$ point of the surface Brillouin zone are derived from p_y-type states. This permits dipole transitions to unoccupied states of *s*-symmetry. Accordingly, these transitions can only be induced by light polarized along the [001] axis. We therefore expect an anisotropy in the reflected light due to polarisation dependent transitions between surface states. Our calculations and experimental data show that only part of the peak can be explained in this way. Even after exposure to full atmospheric pressure a peak at 2.1 eV is still observed. This peak corresponds to the peak predicted by the screened surface local-field effect. The difference between the clean surface 2.1 eV peak and the peak in the air-exposed sample is in our opinion roughly the contribution from transitions between surface states.

A similar contribution in the Ag(110) spectra from dipole-allowed transitions between surface states around 1.7 eV is expected from photoemission results and from second harmonic generation [26]. Indeed, our RAS data of the clean and oxygen reconstructed Ag(110) surface confirm this, as shown in Figure 5.2. This line has not been seen previously in RAS measurements [27]. The strength of the peak is smaller than in the Cu(110) case. This is to be expected from published band structures for the surface states [28]. Comparison of the Cu and Ag band structures reveals that the number of filled states are considerably smaller for Ag. Furthermore, both the position and line-shape agrees well with second harmonic generation results [26]. After oxygen reconstruction, the peak disappeared. Local-field effect theory gives no resonance in this part of the spectrum.

The interpretation that the 2.1 eV resonance in Cu(110) in reality is a double resonance is strengthened by the observation of the 1.7 eV peak in Ag(110). This peak is unquestionably arising from transitions between surface states. A peak arising from transitions between surface states in Cu(110) should therefore also be expected. However, the peak at 2.1 eV remaining after exposure to air can not be assigned to transitions between surface states; thus we are left to conclude that the resonance at 2.1 eV in Cu(110) has two origins.

Conclusions

In conclusion, we have observed a resonance in the RAS-signal from Ag(110) surfaces which can be attributed to transitions between occupied and unoccupied surface states near the $\overline{Y}$

point in the surface Brillouin zone. The observations of these transitions have made a more detailed understanding of the RAS spectrum for Cu(110) possible. We have shown that the reflection anisotropy can be modelled as a sum of contribution from local-field effects close to the surface and transitions between occupied and unoccupied surface states in the $\overline{Y}$ point region.

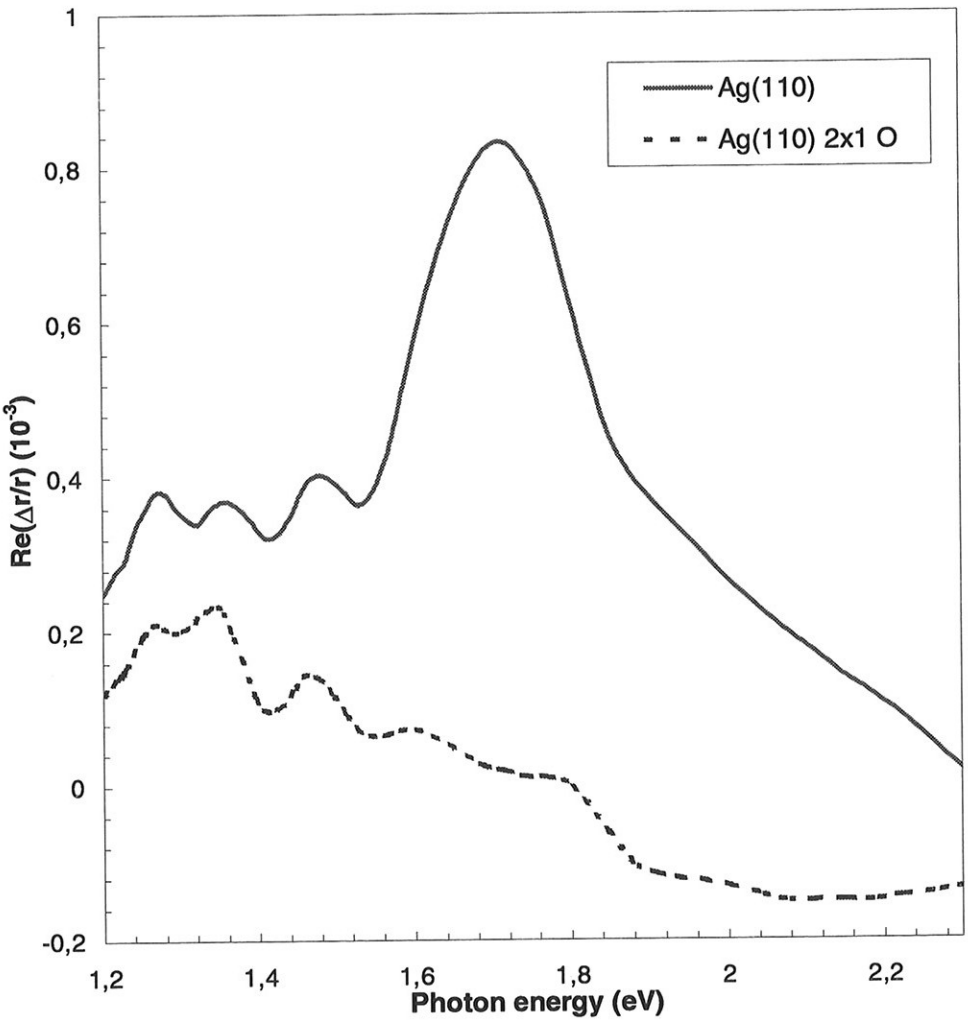

Figure 5.2. RAS spectra for the clean Ag(110) surface (solid line) and oxygen reconstructed Ag(110) (2x1)-O surface in the region around the surface state resonance.

5.2 Local-field effects at the Ag(110) and Cu(110) surfaces studied by reflection anisotropy spectroscopy

Summary

We have calculated the screened surface local-field effect for the fcc (110) case, and applied the results to Cu and Ag. Theoretical reflection anisotropy spectra are compared with experimental ones for both clean and oxygen covered surfaces between 1.8 and 5.5 eV. In the Cu(110) case, there is a satisfactory agreement. For the clean Ag(110) surface, the surface seems to exist in two different states resulting in two qualitatively different RAS spectra. Only one of them can be modelled reasonably well by surface local field effect theory. In addition, we investigate how variation in model parameters change the form of the spectra of Ag(110).

Introduction

Reflection anisotropy spectroscopy (RAS) has recently been introduced as a surface probe for metals. Originally developed for semiconductor surfaces [8][29], RAS measures the normal incidence reflection difference for light polarised along two orthogonal directions. When the bulk optical response is isotropic, RAS is a sensitive tool for detecting weak electronic anisotropies at surfaces. In face-centred cubic crystals like Cu and Ag the surface dielectric function must be biaxial at the (110) surface. As demonstrated elsewhere [30] this effect gives rise to an interesting and characteristic variation in the experimental RAS signal. Several traits in the spectra are mainly a result of the cut-off in the bulk crystallographic structure: the dipole-dipole interaction sums depend on the surface crystallography and give a surface dielectric function that deviates from the bulk permittivity. As stressed by Kar and Bagchi [19] there is a considerably variation in the strength of the induced effective dipole moment with depth near the surface. This variation is different for the $[\bar{1}10]$ and [100] directions and it is this variation which contributes to the RAS signal. Below we present experimental spectra for Ag and Cu, and by including effects caused by screening we discuss in some detail the effects of the local-field on the spectra.

Experimental

The reflection anisotropy of Cu(110) and Ag(110), defined as

$$\frac{\Delta r}{r} = 2\frac{(r_{[\bar{1}10]} - r_{[001]})}{(r_{[\bar{1}10]} + r_{[001]})}, \tag{5.5}$$

were measured *in-situ* in an UHV chamber with base pressure below $1 \cdot 10^{-10}$ mbar. Samples were oriented to within 0.1° and polished. Repeated cycles of argon sputtering and annealing to 670 K (Ag) and 750K (Cu) were used to clean the samples UHV, until a clear low energy electron diffraction (LEED) pattern was observed. Reconstructed (2x1)-O surfaces were obtained by exposure to 10 L (Cu) and 20000 L (Ag) of oxygen [30]. The RAS spectrometer is of the type described by Scholz *et al.* [22], with a spectral range of 1.2 to 5.5 eV. Light from a 150-watt xenon short arc lamp is polarised and focused on to the sample. The reflected beam passes through a photoelastic modulator (50kHz), a polariser (analyser), and a monochromator in front of a silicon pin diode detector. In order to keep window effects as small as possible a BOMCO low-strain window was used. The polarisers is of the Rochon type, and the system is equipped with two monochromators: a single grating monochromator for the energy range 2 to 6 eV and a quartz prism monochromator for the range 1 to 3 eV.

Local-field effects at fcc(110) surfaces

Anisotropy in the reflectivity of Au(110) and Ag(110) have earlier been modelled by a *Swiss cheese* model [32]. One assumes (see Figure 4.1) that the *d* electrons are localised around the ionic core of the atoms in the fcc lattice, whereas the *s-p* electrons are delocalised in the region between the cores. The dipole moment of each lattice point *i* is described by

$$\vec{p}_i = \alpha \left[\vec{E}_0 + \sum_{j \neq i} T_{ij} \vec{p}_j + \sum_{j'} T_{ij'} \vec{p}_{j'} \right], \tag{5.6}$$

where $\vec{E}_0$ the external electric field and T the dipole-dipole interaction operator. The first summation is over all lattice points. The last term is a summation over all the contributions from the mirror dipoles induced above the surface by the screening semi-infinite electron gas. The effective polarisability α for the bulk is obtained from the Clausius-Mossotti relation,

$$\frac{\varepsilon - \varepsilon_{Drude}}{\varepsilon + 2\varepsilon_{Drude}} = \frac{n\alpha}{3\varepsilon_0}, \tag{5.7}$$

where n is the number density of ions, ε is the bulk dielectric function and ε_{Drude} is the permittivity of the electron gas. To solve the infinite set of equations (5.6), we note that each lattice point have the same dipole moment $\vec{p}_n$ in a lattice plane n. The summation over all lattice points can therefore be transformed into a plane-wise summation, where the operator T in (5.6) is replaced by the plane interaction tensor U. We write for the x-component of the dipole moment

$$p_{nx} = \alpha(E_{0x} + \frac{1}{4\pi\varepsilon_0}\sum_{m=0}^{\infty} U_{xx}^{nm} p_{mx} + \frac{1}{4\pi\varepsilon_0}\sum_{m'=0}^{\infty} U_{xx}^{nm'} \frac{\varepsilon_{Drude}-1}{\varepsilon_{Drude}+1} p_{m'x}), \quad (5.8)$$

Here, U_{xx}^{nm} is the contribution to the x-component of a dipole in plane n from all dipoles in plane m. Off-diagonal contributions such as U_{xy}^{nm} vanish because of symmetry reasons in the case of a fcc(110) surface. The U-coefficients are the sum of slowly converging series including all in-plane lattice points, and are calculated by transformation to resiprocal space [18]. The last summation term in (5.8) refers to a sum over all mirror planes m'. In the bulk, there is no contribution from this sum and (5.8) simplifies to

$$p_{Bx} = \alpha(E_{0x} + \frac{1}{4\pi\varepsilon_0}\sum_{m=-\infty}^{\infty} U_{xx}^{nm} p_{Bx}), \quad (5.9)$$

so that the x-part of the relative dipole moments p_{nx}/p_{Bx} can be found from the matrix equation

$$\left(1 - \frac{\alpha}{4\pi\varepsilon_0}U_{xx}^{nm} - \frac{\alpha}{4\pi\varepsilon_0}U_{xx}^{nm'}\left(\frac{\varepsilon_{Drude}-1}{\varepsilon_{Drude}+1}\right)\right)\left(\frac{p_{nx}}{p_{Bx}}\right) = \left(1 - \frac{\alpha}{4\pi\varepsilon_0}\sum_{l=-\infty}^{\infty} U_{xx}^{0l}\right), \quad m,n = 0,\ldots,\infty . \quad (5.10)$$

The U_{xx}^{nm}-coefficients are only dependent on the distance between planes, $|n-m|$, whereas $U_{xx}^{nm'}$ also depend on the distance d to the mirror surface. The dipole moment p_{nx} differ significantly from the bulk value only for the 2 – 5 planes closest to the surface, and (5.10) are reduced to a finite set of equations. Together with the similar solution for p_{ny} we use the result to calculate the surface conductivity

$$\sigma = -i a \varepsilon_0 \, 2^{-3/2} \, \omega(\varepsilon - \varepsilon_{Drude}) \sum_n \frac{p_n - p_B}{p_B}, \quad (5.11)$$

where a is the lattice constant. The RAS signal is then given by the reflection difference

$$\frac{\Delta r}{r} = \frac{2(\sigma_{[1\bar{1}0]} - \sigma_{[001]})}{c\varepsilon_0(\varepsilon - 1)}. \quad (5.12)$$

The previous measurements on the Au(110) and Ag(110) surfaces under ambient conditions were described reasonably well with this model [32].

Results and discussion

We now apply the above calculation to the noble metals Cu and Ag. Using the dielectric data for Cu from Johnson and Christy [21] we get the spectrum shown in Figure 5.1. In this case the distance d to the mirroring surface is assumed to be half of the interplanar distance. In the same figure we have shown result from RAS measurements on clean, oxygen reconstructed

and oxidised Cu(110) at room temperature. It can be seen that our theoretical results reproduce the measured curves reasonably well in all three cases, although the best fit is for the Cu(110) sample in air. The peak around 2.1 eV is shifted towards higher energies and the strength is reduced when the clean surface is exposed to air and oxygen. This shift is most probably due to a change in the critical energy for the onset of inter-band transitions in the bulk dielectric function of copper when approaching the surface. Such a change will shift the peak in the RAS spectrum by the same amount, and in the same direction.

The feature at 2.1 eV for the clean sample has previously been observed by Hofmann *et al.*[23], and they explained it as transitions between surface states near the $\overline{Y}$ point of the surface Brillouin zone. In contrast, our calculations suggest that at least part of the strength in this peak originates from anisotropic local-field effects close to the surface. The double-peak structure around 4 eV in the RAS measurements of the clean Cu(110) is strengthened when the surface is exposed to air or the temperature decreases. At the oxygen reconstructed surface, however, the double peak is replaced by a significantly sharper single peak. Both the magnitude and sign of the reflection anisotropy signal is reproduced by the local-field effect calculations in this energy range, but no double peak structure emerges.

RAS spectra for the Ag(110) surface are shown in Figure 5.3. After a few (<10) cleaning cycles we observed a clear LEED pattern, and the RAS spectrum was at this stage dominated by a double resonance around 3.8 eV. After extensive cleaning (>30 cycles) the spectrum had changed to become similar to the one published elsewhere [27], containing only a single negative peak at 3.8 eV. A small, but clear, feature at 1.7 eV originating from polarisation dependent transitions between surface states was present at both stages [30], indicating a clean surface. When the clean surface was exposed to air, the positive peak reappeared, as shown in Figure 5.3. Together with other RAS measurements [33], our results shows that there exist two distinctive forms of the resonance at 3.8 eV for the clean Ag(110) surface, perhaps indicating two different 'states' of the clean surface.

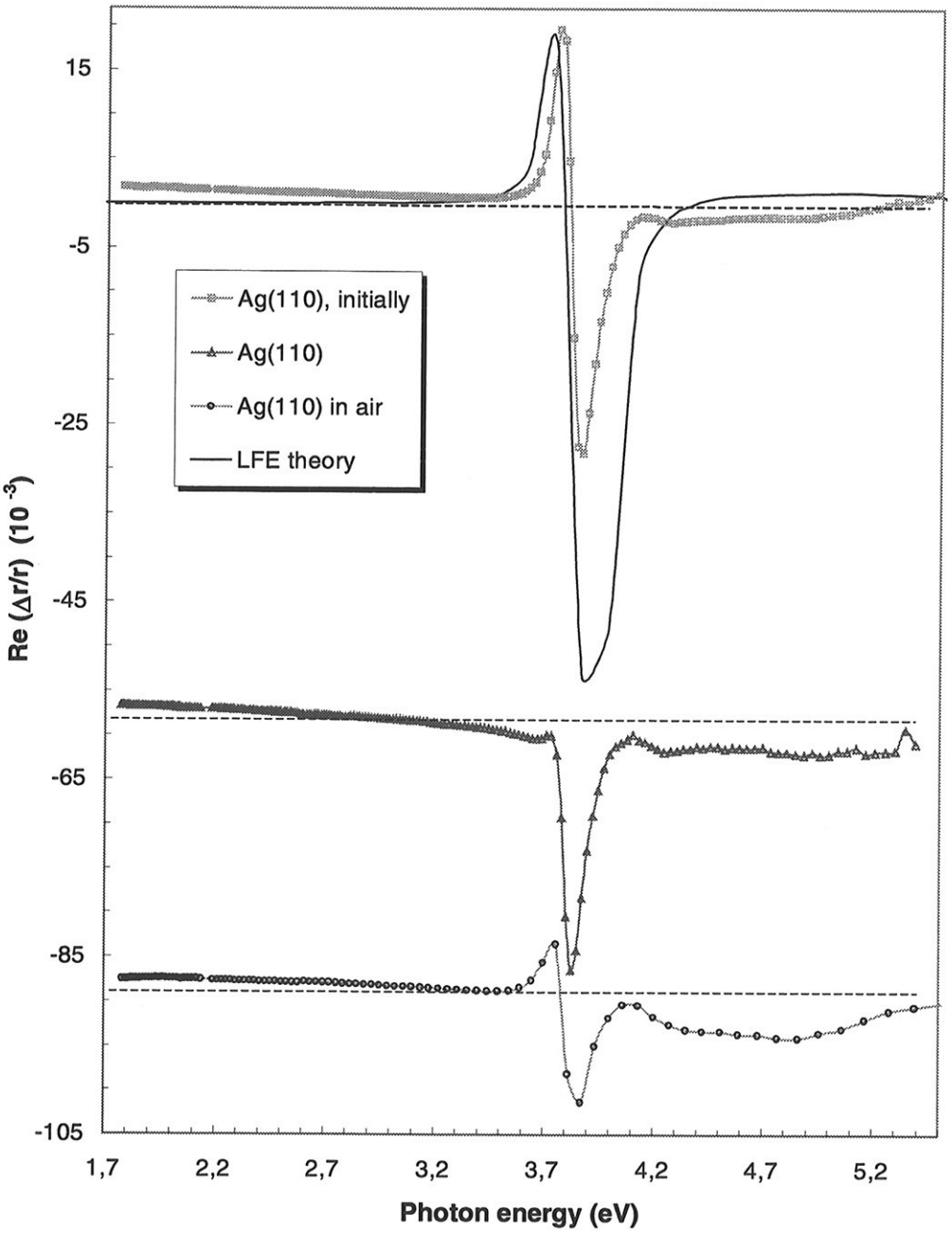

Figure 5.3 Experimental RAS spectra for the initial clean Ag(110) surface (squares), the the Ag(110) surface after extensive cleaning (triangles, shifted downwards), and the Ag(110) surface exposed to air (circles, shifted downwards). The solid line shows the result of the local-field calculations.

The result of local-field effect calculations for the Ag(110) surface, using silver data based on Johnson and Christy [21], is also plotted in Figure 5.3. The d parameter equals half the interplanar distance. The spectrum contains a double resonance at 3.8 eV and resembles the measured double resonance spectra very well. The discrepancy at the negative peak is most probably due to the low reflectivity of silver at that energy. Note also that the RAS spectrum of Ag(110) in air has the same form as the calculated curve.

To investigate how the Swiss cheese parameters discussed above influence the line-profile, we did calculations using different dielectric data sets, and varied the plasma frequency. In addition the d parameter for the electron gas/vacuum boundary surface was adjusted. In all cases the resulting spectra showed a relatively large variation in both the strength and form of the peak at 3.8 eV. The d-parameter depends on such effects as electron spill-out and surface relaxation. Figure 5.4 shows the result of varying d in the range 0.45 – 0.55 of the interplanar distance. Again, dielectric data from Johnson and Christy [21] were used, and the value for the plasma frequency was $\omega_p = 9.17$ eV. Even in this small range there is a significant variation in the spectra. Increasing d leads to a decreased size for the negative peak and a shift of the resonance towards higher energies. The positive peak has a maximum at $d = 0.46$ and decreases with larger d. The best fit to the double resonance spectrum is for a distance $d =$ 0.51. Greater variations in the d parameter produced a range of different curves. However, we were not able to reproduce satisfactorily the single resonance form of the RAS spectra by varying parameters in the surface local field model.

Concluding remarks

We have shown that the surface local-field effect model is capable of explaining several features in the reflection anisotropy spectra of both Cu(110) and Ag(110). Somewhat unexpected, this is especially true for the oxidised surfaces, perhaps because the model parameters for some reason are best suited for such cases. There seem to be two different surface conditions for clean Ag(110), resulting in two qualitatively different reflection anisotropy spectra. It is of much interest to investigate this effect further, for example with RAS in combination with scanning tunneling microscopy.

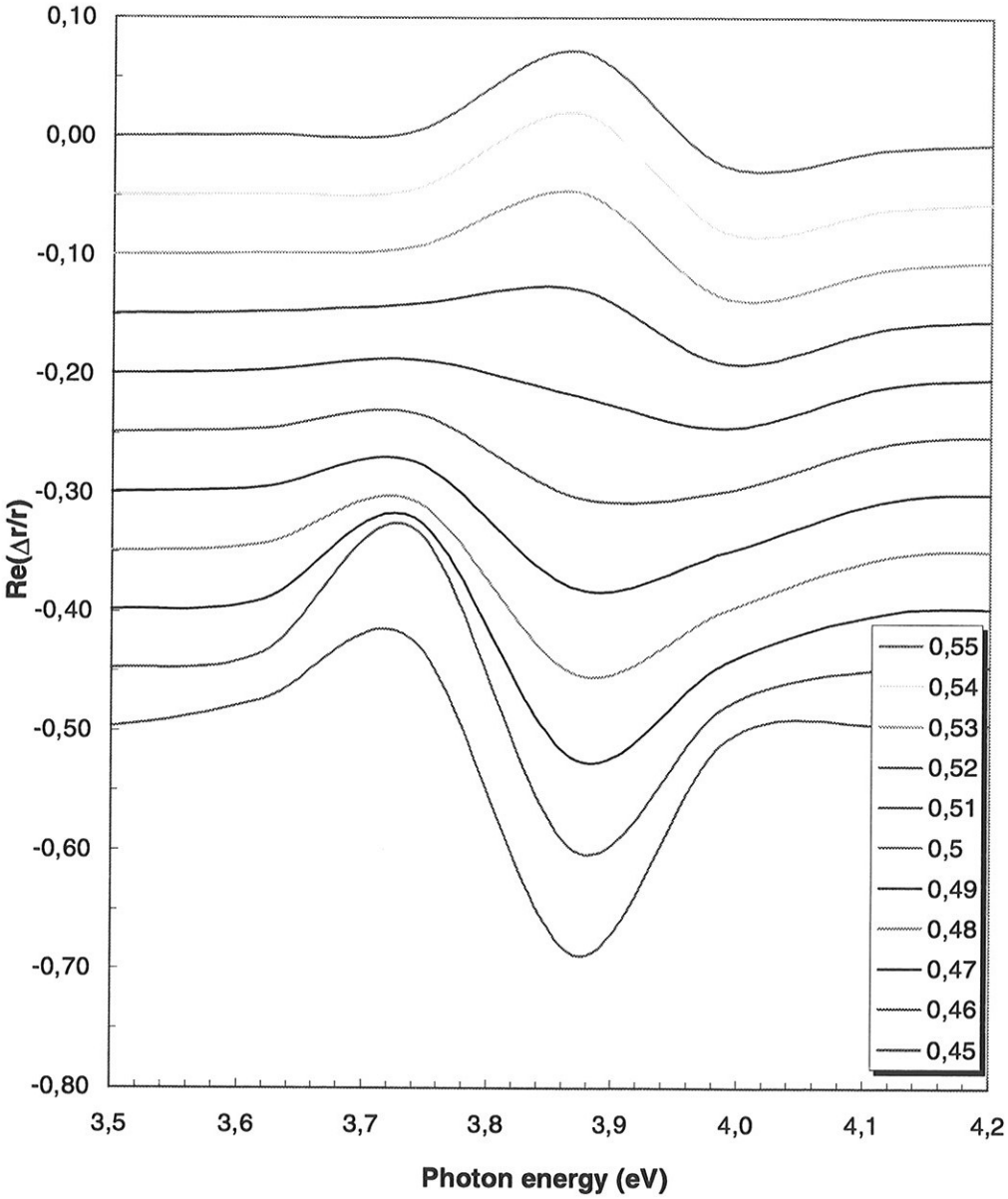

Figure 5.4. Theoretical RAS spectra for the Ag(110) surface based on local-field effect calculations with the varying *d*-parameter: 0.55 (top) to 0.45 (bottom). The curves are shifted successively downwards.

5.3 The effect of sputtering-induced disorder on the surface dielectric tensor of Cu(110)

Summary

The effect of low-energy sputtering on the surface electronic structure of Cu(110) was studied under room temperature conditions by means of reflection-anisotropy spectroscopy (RAS) at photon energies between 1.6 and 6 eV. Sputtering times varied from 0 to 60 minutes, and the energy of the Ar^+ ions was 500 eV. Spectral changes that depended on fluence in a reproducible manner were observed. We argue that vacancies in the top layer are responsible for some of the strongest changes, at least for short sputtering times. The spectra could be reproduced by local-field calculations where the screened dipole-dipole interaction coefficients between the top layer and the underlying ones were reduced by a factor proportional to the vacancy concentration. Both components of the surface dielectric tensor are calculated. The behaviour of the RAS signal for longer sputtering times is discussed.

Introduction

The surface morphology of sputtered metals and semiconductors has recently attracted much interest [34][35][36][37][38]. When an initially flat surface is ion bombarded, erosion takes place, and the surface area increases. This effect tends to increase the total surface energy of the sample, but several diffusion channels act as stabilizing mechanisms. Time and temperature are important experimental parameters, and in addition the kinetic energy of the ions plays a decisive role. Eklund *et al.* [39] studied the graphite surface bombarded with 5 keV Ar^+ ions, and were to the authors' knowledge the first to study the scaled behaviour of the height-height correlation function.

It has been suggested [36][40] that at low kinetic energies, i.e. below 1 keV, sputtering may be looked upon as a kind of *inverted* layer-by-layer growth. The difference between such a process and conventional homoepitaxial growth, of the van der Merwe type, is mainly that instead of mobile adatoms and islands the surface contains a growing fraction of vacancies and vacancy islands, i.e. flat holes completely surrounded by monostep terraces. Formation of vacancy islands requires that vacancies are free to condense. The temperature must therefore

be sufficiently high, and the step edge barrier [41] low, for this to occur. Alternatively, the ion flux must be so weak that the process is not too far from equilibrium.

Recently, the effect of sputtering on the Ag(110) surface has been studied by a variable temperature scanning tunneling microscope [38]. In a limited range around room temperature a ripple structure whose wave vector pointed along the [001] direction was observed. The ripples were absent for ion energies below 800 eV, and in contrast to their formation on isotropic surfaces [42], they did not depend on the direction of the incoming ions.

In spite of many morphological studies, not much is known about the change in the spectroscopic parameters upon sputtering. Here, we report on some characteristic changes in the surface electronic structure of clean Cu(110) following bombardement with low-energy Ar^+ ions.

Experimental

As experimental method we apply reflection-anisotropy spectroscopy (RAS) which gives the difference between the complex reflection amplitude for the $[\bar{1}10]$ and [001] directions, i.e.

$$\frac{\Delta r}{\bar{r}} = 2\frac{(r_{[\bar{1}10]} - r_{[001]})}{(r_{[\bar{1}10]} + r_{[001]})}, \tag{5.13}$$

Using a photoelastic modulator, and a 150 watt xenon short arc lamp as light source, the signal was measured as function of sputtering time. A silicon pin diode was used as detector. . The copper sample was prepared by polishing, and orientated to within 0.1°. Before starting the controlled sputtering process in the UHV chamber the surface was cleaned with cycles of argon sputtering and annealing to 750 K. The optical window in the vacuum chamber was of the low-strain type in order to keep the influence on the RAS signal at a minimum. The cleaning cycles were repeated until a sharp (1x1) low energy electron diffraction (LEED) image was observed. The base pressure of the chamber was less than 10^{-10} mbar.

During sputtering the vacuum-chamber was backfilled with Ar gas of 99.999 % purity. Ar^+ ions with energy 500 eV were directed towards the sample at an angle of incidence close to 30°. The projection of the beam direction was parallel with the $[\bar{1}11]$ direction of the sample surface. The RAS signal was measured for a variety of sputtering times.

Results and discussion

In order to show the main trend of the measurements we present in Figure 5.5 $\mathrm{Re}(\Delta r / \bar{r})$ curves corresponding to the sputtering times 5, 10, 25 and 35 minutes. With an Ar^+ ion flux around $4 \cdot 10^{17}$ m^{-2} s^{-1} this gives a fluence that increased from 0 to about $8 \cdot 10^{20}$ m^{-2}. The spectra corresponding to larger fluences are not shown as they did not deviate much from the 35 minutes spectrum. No pronounced broadening of the LEED diffraction spots could be detected. However, the diffuse LEED background increased slightly with sputtering time.

Also included in Figure 5.5 is the spectrum for the clean, unsputtered surface. As

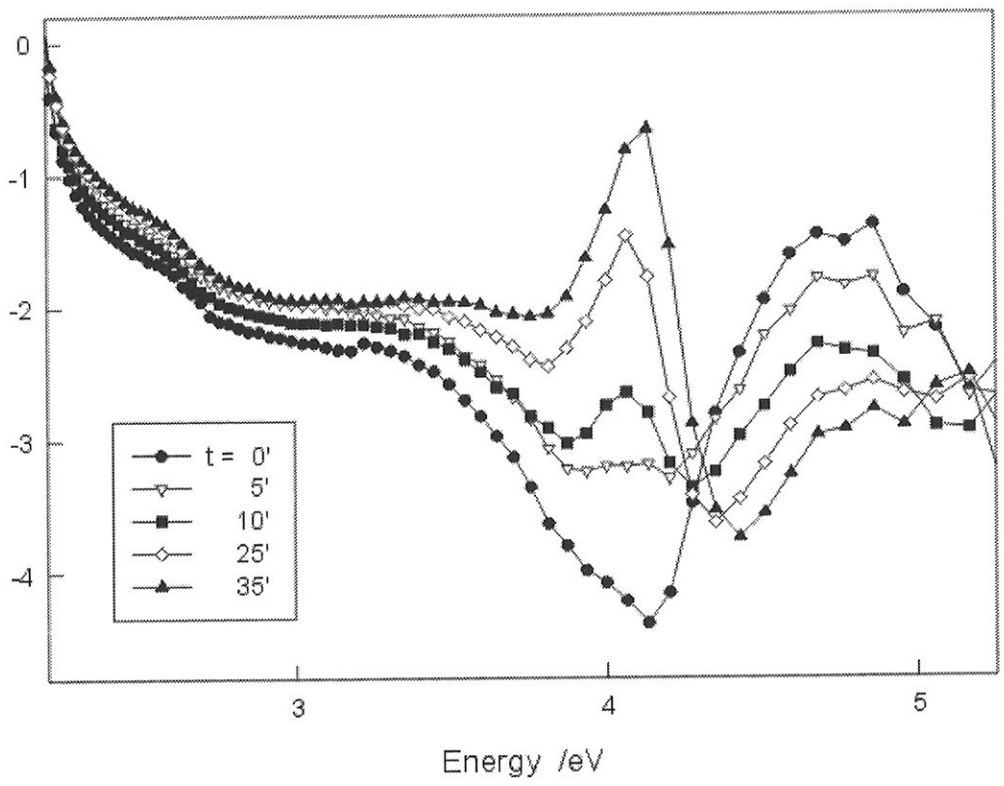

Figure 5.5. Experimental reflection-anisotropy spectra for the both the unsputtered and the sputtered Cu(110) surface. The data are recorded for sputtering times that varied from 0 to 35 minutes. (The curves for longer sputtering times did not deviate much from the spectrum corresponding to 35 minutes.)

demonstrated elsewhere [30] several main features of this spectrum can be explained by the local-field theory of Tarriba and Mochán [15]. According to this theory, the dipole moments associated with the surface d-band transitions interact with each other and with their mirror images. The shielding factor is $s = (\varepsilon_g - 1)/(\varepsilon_g + 1)$ where the electron gas contribution $\varepsilon_g = 1 + \chi_g$ has its origin in the delocalized sp-electrons. Since the dipole-dipole interactions associated with the surface interband-transitions are inequivalent for the in-plane $[\bar{1}10]$ and [001] directions, a non-zero RAS signal is generated. There are, however, two additional contributions in the experimental spectrum. First, in agreement with the findings in [23], most of the line-strength around 2 eV has its origin in transitions between surface states near the $\bar{Y}$ point of the surface Brillouin zone [25]. Second, below 2 eV the real and imaginary parts of the experimental RAS signal show that the effective mass for electron transport in the $[\bar{1}10]$ direction is smaller than for transport along the [001] direction, while the corresponding lifetime is larger [43]. The strength of the RAS signal at and below 2 eV did not change significantly during the sputtering, and this region is not included in Figure 5.5.

The minimum in the experimental curve for the unsputtered surface around 4.1 – 4.2 eV, and the broad maximum between 4.7 and 4.9 eV, are well reproduced by the local-field theory alone. The calculated curve has the same shape as the measured one, but is shifted downwards in energy. Upon sputtering, the observed minimum in the experimental curve becomes less pronounced, and after a few minutes of sputtering time a maximum starts to emerge. The new peak becomes sharper with additional sputtering, but its strength appears to saturate after about 35 minutes. To discuss this behaviour we apply the expression

$$\frac{\Delta r}{r} = -\frac{4\pi i t \Delta\varepsilon_s}{\lambda(\varepsilon_b - 1)} \tag{5.14}$$

which is a first-order expansion in (t/λ) of (5.13), with λ as the wavelength and t as the thickness of the surface region. The difference between the two in-plane principal components of the surface permittivity tensor is $\Delta\varepsilon_s = \varepsilon_{[\bar{1}10]} - \varepsilon_{[001]}$. Because the maximal value of the peak between 4.1 eV and 4.2 eV is very close to zero the principal values of the surface tensor are almost equal here. In contrast, the broad maximum between 4.7 and 4.9 eV becomes less pronounced upon sputtering.

The fixed point at 4.3 eV shows that the difference between the principal values remains constant at just this energy value. The modifications of the RAS signal below and above the fixed point must be closely related to the change in the surface morphology. As a result of the ion bombardment the surface contains an increasing amount of vacancies, vacancy islands, and steps. In addition, particularly after long sputtering times, ripple-shaped disorder and fractal-like topography may be present. We interpret the increasing diffuse background in the LEED pattern as a growing number of uncorrelated surface defects, in particular surface vacancies. It is of interest to calculate their effects on the RAS data. The contribution from the d-band to the bulk permittivity is χ_b, and ε_g is approximated by a Drude term. Near the surface the interband transitions gives rise to a depth dependent effective polarization that deviates from the bulk value. Using the Clausius-Mossotti relation and introducing layer dependent susceptibilities χ_j this can be written as

$$\chi_j = \frac{1}{3+\chi_b}(3+\sum_{k=0}^{K-1} U_{|j-k|}\chi_k + s\sum_{k'=0}^{K-1} U_{j+k'}'\chi_{k'}) \qquad (5.15)$$

The surface region, and thereby the upper limit K in (5.15), is determined by the requirement that $\chi_j \neq \chi_b$. The U_m and U'_m coefficients express the dipole-dipole and dipole-mirror dipole interaction, respectively. A discussion of the U' coefficients is given elsewhere [44]. The subscripts of the coefficients denote the numbering of planes from the actual dipole. Thus, U_0 refers to interaction with dipoles that are in the same plane, and U_m to the effective interaction with dipoles in the m'th neighbouring planes. In the absence of relaxation $U_m \equiv U_{-m}$.

The numerical evaluation of the coefficients can be simplified by various mathematical techniques [17][18]. Some of the strongest coefficients for the $[\bar{1}\,10]$ direction of the vacancy-free surface are: U = [13.5484, 2.0116, -0.4179,..]3/(16π), U'= [-14.9867, 0.1807, -0.0153,..]3/(16π). For the [001] direction we find U = [2.5627, 8.3801, -1.4108, ..]3/(16π), and U'= [-20.3247, 1.2310, -0.1441,...]3/(16π). We base the calculations for the sputtered surface on the assumption that there is an average number n of vacancies in the top layer. If the vacancies are distributed randomly over N lattice sites the effective oscillator strength associated with the top layer decreases. Indirectly, through (5.14), the effect of a non-zero vacancy concentration $f = n/N$ modifies the polarization also in deeper layers. The ensemble-averaged values for the $f \neq 0$ case can be found by running a Monte Carlo

program that calculate the contributions from the various vacancy configurations. However, such calculations are equivalent with the approximation

$$< U_m > \approx (1 - \frac{n}{N}) U_m \tag{5.16}$$

A similar expression is valid for $< U_m' >$. The RAS signal is obtained by inverting

$$\mathbf{M}\chi = \beta \tag{5.17}$$

with $\beta^T = \alpha(1,1,...1)$ and the polarizability $\alpha = 3/(3 + \chi_b)$. The matrix elements in (5.17) are

$$M_{ij} = (1 - \alpha \cdot u_1)\delta_{ij} - \alpha(u_{1+|i-j|} \cdot (1 - \delta_{ij}) - s \cdot u_{i+|j-1|}') \tag{5.18}$$

Here, $u_{m+1} \equiv < U_m >$ and $u_{m+1}' \equiv < U_m' >$ whenever an element M_{i1} belongs to the first column. In the rest of the matrix $u_{m+1} \equiv U_m$ and $u_{m+1}' \equiv U_m'$. The difference between the

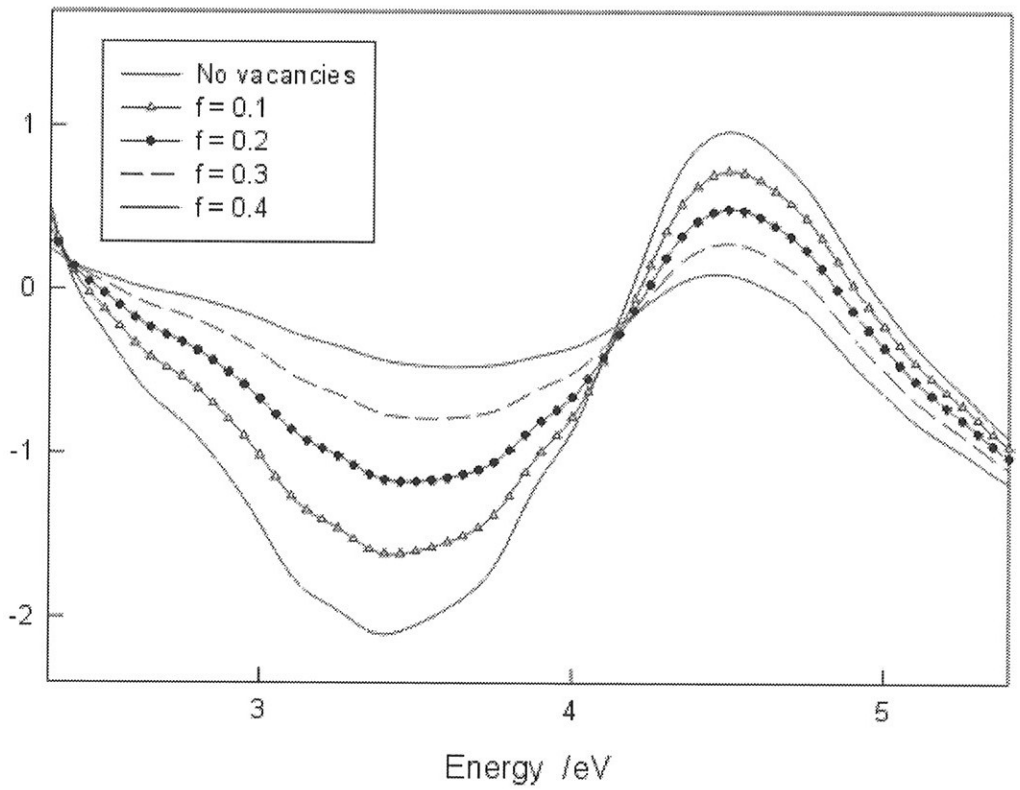

Figure 5.6. RAS curves calculated by local-field theory for vacancy concentration $0 \leq f \leq 0.4$ in the top layer of Cu(110).

effective permittivities in (5.14) can be obtained by calculating the effective susceptibility in each principal direction. The RAS curves calculated by this method are shown in Figure 5.6. We have assumed that f increases linearly with fluence, and the five curves correspond to $f = 0,....0.4$. It can be seen that the development of the RAS signal is well reproduced between 4.3 and 5.2 eV. The presence of a fixed point is also verified. Since the RAS signal approaches zero with increasing f the main trend below 4.3 eV is also in agreement with the experimental data. The small discrepancy between the measured and calculated ordinate values is mostly due the non-zero strain in the window glass.

The energy of the fixed point happens to coincide with a minimum in the bulk ε_2 curve [21]. The minimum arises because interband transitions near the K point in the Brillouin zone take place at lower energies than transitions associated with the L point. The K absorption features are caused by transition from the filled 3d band to the Fermi level, while transitions from partially filled states with s symmetry near the Fermi level to the unfilled 4p band define the L features [45]. In Figure 5.7 we show the imaginary part of the permittivity for the vacancy-free Cu(110) surface, and include the bulk permittivity for comparison. It can be seen that the minimum in the latter curve becomes weaker at the surface, and the [001] component deviates considerably from the $[\bar{1}10]$ component. When vacancies are introduced into the top layer one expects the difference between the two directions to diminish, in agreement with Figure 5.7. The presence of the 'diluted' surface causes the effective surface permittivity to drop significantly below the curve for the bulk values. In Figure 5.8 we show the real part of the surface permittivity. When no vacancies are present the curves for the two tensor axes cross each other at the arrow in the figure. If the vacancy concentration increases to $f = 0.3$ the crossing points are shifted upwards. At the same time both curves become less negative. There is no simple relationship between these crossing points and the energy of the RAS fixed point. According to (5.14) the energy of the fixed point is determined also by the imaginary tensor components and the bulk permittivity.

Conclusions

In conclusion, we find that sputtering-induced changes in the RAS curves can be explained as a reduction in the effective dipole moments associated with the top layer. The good agreement between the calculations and the RAS signal indicates that during the initial phase of the ion bombardment the surface is dominated by large regions that are relatively flat. In these

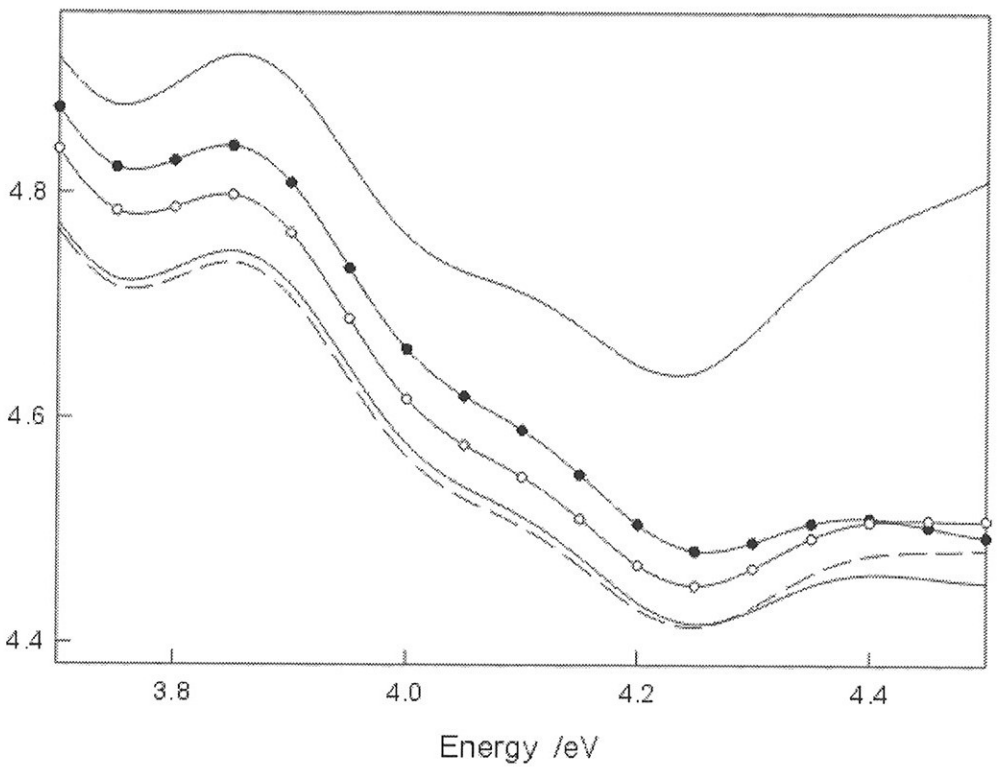

Figure 5.7. The imaginary part of the Cu(110) surface permittivity. The upper, fully drawn curve for the isotropic, bulk copper permittivity is included for comparison. Below, the [$\bar{1}$10] (filled circles) and the [001] (unfilled circles) surface tensor components are shown. The two remaining, lower curves show the [$\bar{1}$10] (unbroken) and the [001] (broken) components for a surface with a vacancy occupancy equal to 0.3. The curves have been calculated by local-field theory.

regions there is a steadily increasing vacancy concentration. At longer sputtering times formation of vacancy islands and layer-by-layer removal start to takes place. It is clear, however, that this simple model is incapable of explaining the sharp peak that emerges just below the fixed point for the longest sputtering times. Equation (5.14) suggests that this maximum could arise either because there is a large imaginary value for the $[\bar{1}10]$ tensor component, or a small value for the [001] component. Another possibility is that the real part of the $[\bar{1}10]$ component becomes small while the [001] component increases. In order to choose between the various cases it would be of interest to know the influence of such features as steps, scaled surface topography, or ripples. Here, it is a problem that it is difficult to predict the length scale on which the height-height correlation starts to influence the RAS signal. The LEED data must therefore be supplemented with information about the surface morphology obtained by for example laser scattering, or such real-space techniques as scanning tunnelling microscopy and atomic force microscopy.

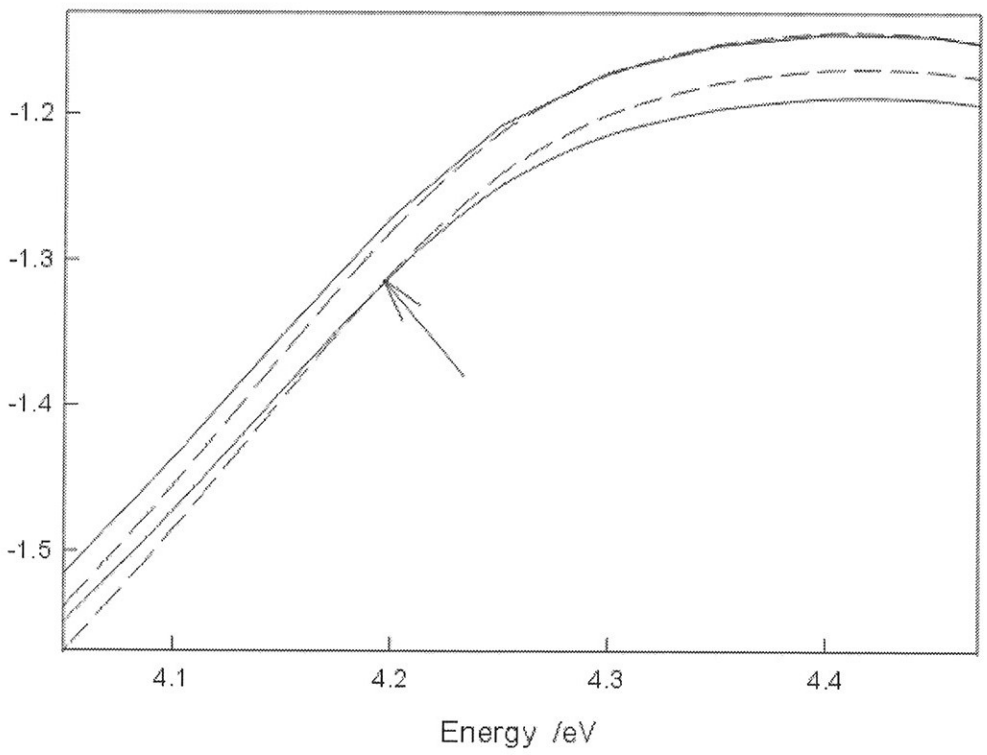

Figure 5.8. The real part of the surface permittivity tensor of Cu(110). The unbroken and dotted curves which crosses each other at the arrow are the $[\bar{1}10]$ and the [001] components of the vacancy-free surface, respectively. The two remaining curves show the components of a surface where 30 % of the lattice sites in the top layer are unoccupied.

5.4 The influence of surface steps on the optical and electronic anisotropy of Ag(110)

Summary

The Ag(110) surface was studied at various stages of annealing and ion bombardment cycles by means of reflection-anisotropy spectroscopy (RAS) and scanning tunnelling microscopy (STM). At low fluence and a limited number of heat treatment cycles a positive RAS signal at 3.8 eV followed by a negative peak at 3.9 eV was recorded. STM showed that the room temperature surface corresponding to this curve profile had steps whose edges were parallel with the in-plane [110] direction. At longer sputtering times, with several cycles of annealing, we obtained a statistically isotropic distribution of steps and terraces. Ag(110) surfaces of the latter kind result in RAS curves where the positive low energy component at 3.8 eV is absent. We discuss the spectra in terms of local-field calculations where the screened dipole-dipole interaction coefficients are modified by surface steps. If the step edges are isotropically distributed instead of parallel to the [110] direction the strength of the low-energy part of the RAS curve is reduced. However, the calculated reduction in strength is not enough to account for the experimental results. Step-induced coupling to surface plasmons is an additional mechanism, which gives a much stronger reduction in strength. The influence of both effects on the RAS curve increases with decreasing correlation length. The plasmon-based mechanism takes place already at lengths of order 100 nm, whereas the cut-off in the dipole-dipole interaction need correlation lengths that are almost one magnitude lower to be important.

Introduction

Low-index surfaces of Ag crystals attain very easily a corrugated topography. There is an energy cost in creating extra surface area, but at high temperatures the lowering in the free energy due to the configurationally entropy of the topography is sufficient to create a stable structure. The roughening transition of Ag(110) was first studied by G. A. Held *et al.* [46] who found evidence for a transition temperature around 720 K. Out-of-plane diffraction data [47] indicate that thermal roughening occurs through a process in which (110) faceted regions are gradually replaced by the rough phase. The roughening temperature found from this type of data was 790 K. Recently [38], the surface morphology resulting from ion bombardment of Ag(110) has been studied by scanning tunnelling microscopy (STM). It was concluded

that bombardment around room temperature stimulates the growth of a ripple structure whose direction is independent of both azimuthal and polar beam angle. The ripples were found to be parallel with the in-plane $[1\bar{1}0]$ direction, and the average spatial periodicity was 63 ± 13 nm. The coherence length was several hundred nanometers. The data indicated that in order to achieve ripple formation the kinetic energy of the ions has to be larger than about 800 eV. Not much is known about the change in the electronic structure following step formation on a metal surface. This is in strong contrast to the morphology itself, where several theories have been formulated and applied to the study of both step dynamics and step interaction [48]. Changes within the surface Brillouin zone are easiest to interpret when the step direction is coincident with one of the surface main axes; in the Ag(110) case this means the [001] or the $[1\bar{1}0]$ direction.

The technique of reflection-anisotropy spectroscopy (RAS) gives the difference between the complex reflection amplitude for light polarized in two orthogonal directions. The RAS signal typically originates from the outer 3-4 layers and the technique should therefore be a sensitive probe for the study of step-induced changes. It has recently been established [30][33] that when RAS measurements on Ag(110) are made under ultra high vacuum (UHV) conditions transitions between surface states generate a line at 1.7 eV. In an oxygen atmosphere this feature is completely absent.

In Ag the permittivity at the d-band absorption edge is caused by transitions in extended regions of the Brillouin zone[49]. The interband transitions [21] [50] have a well defined on-set around 3.8 eV. Below 3.8 eV the band structure is free-electron like. In contrast to simple metals [51] the slope of the surface plasmon dispersion is found to be positive [52] in angle resolved electron energy loss spectroscopy, where moment transfers normally are larger than in optical experiments. In jellium models of metal surfaces a negative slope indicates that the centroid of the screening charge is outside the surface. Another interesting feature of Ag(110) is that the surface plasmon dispersion is anisotropic [53]. The first indication for this effect was found by attenuated total reflection experiments in air [54]. The 4d bands push both the surface (3.68 eV) and bulk (3.78 eV) plasmon frequencies in the $\vec{q} = 0$ limit just below the on-set for interband transitions, but it is not known in detail how this influences optical experiments [55][56].

The first RAS studies [20] of Ag(110) showed that a strong two-peak feature with dispersion-shape is present just below 4 eV. A strong maximum at 3.8 eV followed by a negative peak at 3.9 eV was observed, but the experiments were performed in air. Subsequent measurements made under UHV conditions indicated that the characteristic dispersion-shape is present also when the surface is clean [33]. Surprisingly, however, a clean Ag(110) surface can in some cases result in a RAS profile where the two-peak structure is absent. Instead, there is a negative single-line peak at 3.9 eV. The positive low-energy part of the dispersion-shaped double peak loses its strength after repeated cleaning and annealing [27][44], and vanishes almost completely after a certain number of cycles. The end result is then a single negative peak at 3.9 eV.

Since Ag is a noble metal it is of interest to do local-field calculations in an attempt to interpret the RAS profile in the absorption edge region. However, reasonable choices of parameters tend to give a profile with dispersion shape, and it seems difficult to explain the development towards a negative single-line peak. It is possible to reduce the strength of the low-energy peak somewhat by adjusting the distance from the top atomic layer to the location of the mirror plane [44]. This parameter simulates the effects of electronic spill-out. It appears nevertheless difficult to suppress the peak completely by this and other modifications of standard local-field theory. The apparent failure of local-field theory to describe the observed single-line RAS profile of Ag(110) should be contrasted with the Cu(110) case where a good agreement with experimental data is easily obtained [43].

The influence of the surface morphology on the RAS signal has to the authors' knowledge not been much discussed. In the Ag(110) case it is of interest to identify those structural parameters that are able to reduce the strength of the low-energy part of the dispersion-shaped RAS profile. Below, we report on the relationship between the step structure as measured by STM and RAS. Using STM it should be possible to correlate effects of short-wave height-height correlations, of order several nanometer, with electronic anisotropy. We also calculate and discuss the effects of surface plasmons and the local-field.

Experimental

The two silver samples, A and B, described in this study were prepared by polishing and oriented to within 0.1° with respect to the surface normals. The orientation was checked by

Laue recordings. Inside the vacuum chamber the surface quality was controlled by LEED. The base pressure of the chamber was $2 \cdot 10^{-10}$ mbar. The surfaces were cleaned with cycles of argon sputtering and annealing to maximum 750 K. During sputtering the vacuum chamber was backfilled with Ar gas. Ar^+ ions with energy 500 eV were directed towards the sample at angles of incidence in the 30° - 45° range. The azimuthal angle, i.e. the projection of the beam direction, was 45° with respect to the in-plane [001] direction. The sample B had earlier been used in optical experiments in another vacuum chamber, and had for that reason been exposed to much higher number of cleaning cycles than sample A.

The STM experiments were carried out using a room temperature Omicron UHV STM. The STM images were recorded in constant current mode, using -1.0 nA tunnelling current and -1.0 V bias voltage. These tunnelling conditions were used to ensure that the STM-tip did not modify the surface during scanning. The STM data are represented as top view greyscale images with the darkest colours representing the lowest levels.

With a photoelastic modulator, and a 150 watt xenon short arc lamp as light source, we have constructed a compact, portable RAS set-up, which can be used for *in situ* measurements of samples inside the STM chamber. A silicon pin diode was used as detector. There was a small and slowly varying background in the RAS signal despite the installed low-strain window in the STM chamber. It is in principle possible to correct for this effect by using the fact that the signal is non-zero only in a narrow interval around 4 eV. Since the RAS signal is strong, and the noise level low, we present uncorrected spectra.

STM images and RAS profiles

We show in Figure 5.9 some STM images of the Ag(110) surfaces. Figure 5.9 a) and b) shows the surfaces of samples A and B, respectively. The surface of sample B is clean and the monostep-heights of Ag(110) are clearly visible. There is a distribution of monostep terraces with no common, preferred direction. Some of the terraces are several hundred nanometer wide, but the average terrace width was found to be typically one magnitude lower. The surface of sample A is also clean but the steps tend now to be parallel with each other. This sample has undergone a limited number of cleaning cycles. The STM images are representative for the whole sample area since several images were taken across the whole sample. In qualitative agreement with the ripple formation described by [38], the step

direction turns out to be aligned with the $[\bar{1}10]$ direction. Note that we used a kinetic energy of 500 eV for the Ar^+ ions. This value is well below the proposed threshold energy [38] of 800 eV for formation of parallel ripples.

In Figure 5.10 and Figure 5.11 representative $\mathrm{Re}(\Delta r / \bar{r})$ curves for the surfaces corresponding to Figure 5.9 a) and b) are shown. The experimental data (filled triangles) in Figure 5.10 show that if the step edges are aligned the RAS profile has a dispersion shape. It is of some interest to note that in agreement with [32] measurements on sample A before complete cleaning gave a RAS profile with a much stronger low-energy peak. We do not include these initial spectra in the discussion since the surface is not clean. Apart from the amplitude itself the measured profile corresponding to isotropic disorder in Figure 5.11 (filled triangles) is in agreement with independent UHV measurements [27]. It appears that annealing and ion bombardment reduces the height of the low-energy peak in Figure 5.10

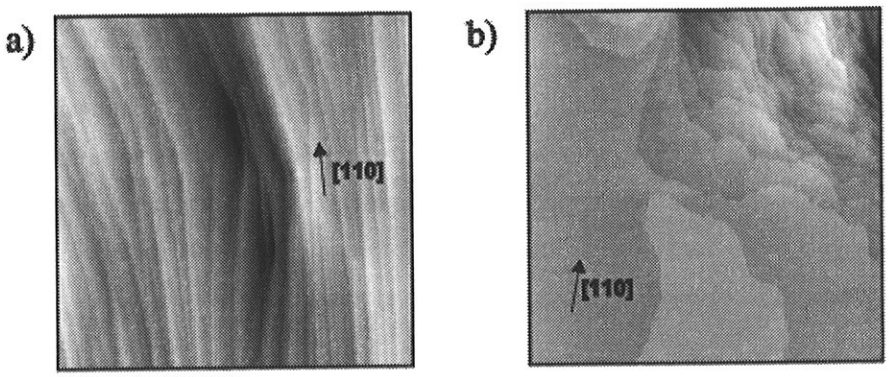

Figure 5.9. STM images, 500x500 nm^2, of two Ag(110) samples. The in-plane [110] direction is indicated in both images. The tunneling current was -1.0 nA and the sample bias voltage -1.0 V. Each step corresponds to a height difference 0.144 nm. (a) Surface distribution of monostep terraces for sample A, which has been exposed to a limited number of ion bombardment/annealing cycles, but is clean. (b) The surface of sample B. This surface is also clean, but the total number of cleaning cycles is much higher.

almost one magnitude. Simultaneously, the negative high-energy component is reduced in strength, but not to the same degree, with the end result shown in Figure 5.11.

Phenomenological treatment

Assuming the validity of a two-layer model the real part of the RAS signal from a cubic sample is $\propto -it\Delta\varepsilon_s/(\varepsilon-1)$ where t is the thickness of the surface region, s stands for surface, and $\Delta\varepsilon_s$ is the difference between the surface tensorial components of the dielectric function. Note that this difference, and thereby the whole RAS profile of Ag(110), can be parameterised in a very simple way by the bulk permittivity alone: if the absorption edge associated with the on-set for interband transitions for one of the two principal directions is slightly shifted in energy a non-zero $\Delta\varepsilon_s$ results. Clearly, if we neglect the real part of $\Delta\varepsilon_s$

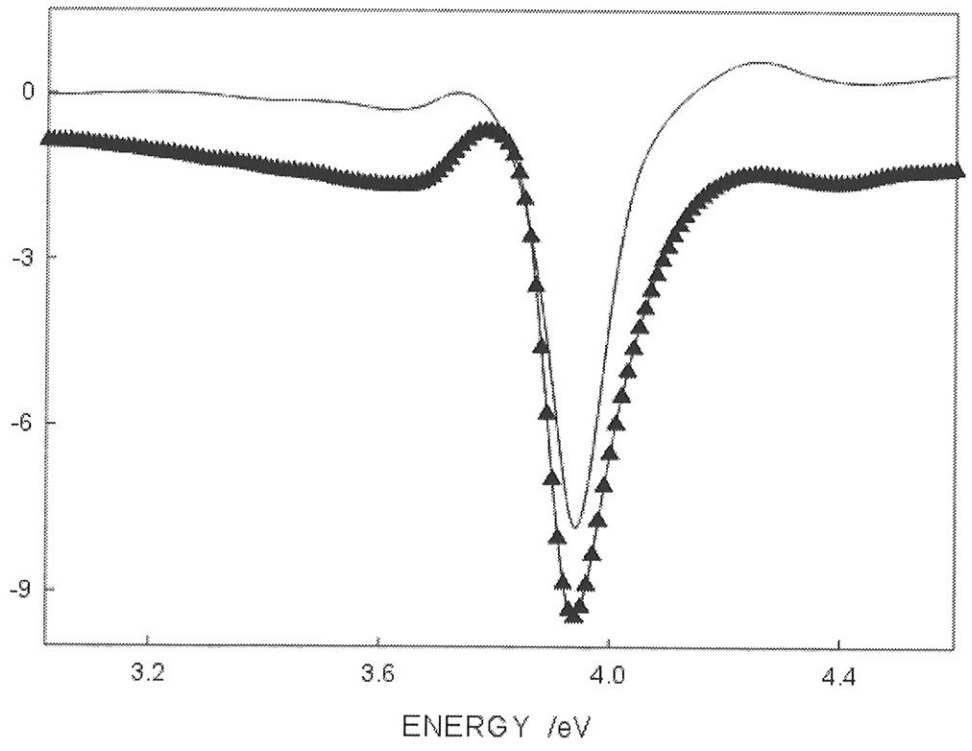

Figure 5.10. Experimental (filled triangles) and calculated (unbroken curve) reflection-anisotropy spectrum for sample A.

and the influence of the denominator $(\varepsilon - 1)$ the RAS profile must resemble a single line, approximately given as the algebraic difference between the d-band absorption edges. If one of the absorption edges instead of being shifted is broadened the curve can get a dispersion shape. Minor shift and broadening effects of this type can generally be expressed as the first-order expansion

$$\Delta\varepsilon_s \approx (\Delta\omega + i\Delta\Gamma)\frac{d\varepsilon}{d\omega}. \tag{5.19}$$

The parameters $\Delta\omega$ and $\Delta\Gamma$ are equal to the difference in energy shifts and lifetime broadening, respectively, for the two principal directions. Derivative effect given by (5.19) has been noted for semiconductors [57], but has to the authors' knowledge not been much discussed for metals [27][43]. It has recently been suggested that derivative spectra in optical

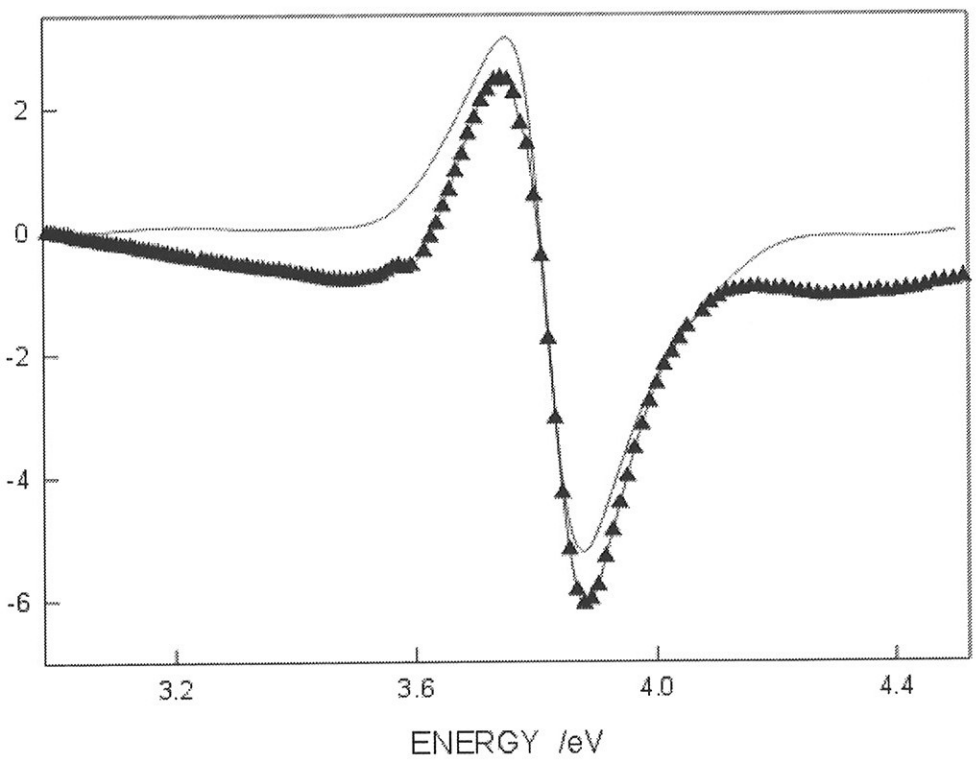

Figure 5.11. Experimental RAS profile (filled triangles) for sample B. Calculations are shown by unbroken, upper curve.

surface spectroscopies generally may be an effect of final-state localization [58]. As a result of the absorption process the electrons and holes form propagating wave packets, and there arise small differences in the measured bulk critical point energies and broadening parameters.

Using $\Delta\Gamma = 0$ and $\Delta\omega \neq 0$ we obtain a very good description (unbroken curve) of the spectrum in Figure 5.11, corresponding to Figure 5.9 b). This is in agreement with the study published in [27] for another Ag sample that also had undergone several sputtering and annealing cycles. The small vertical disagreement is due to effects of the window strain. The permittivity data given by [21] were used in the calculations. It is of particular significance that (5.19) also reproduces the remaining, weak low-energy peak. It can be concluded that the RAS feature of sample A resembles the signal that would arise if the interband transitions for light polarized in the [001] direction hypothetically took place at slightly higher energies than for light in the $[1\bar{1}0]$ direction. The two absorption edges are unbroadened. The value obtained for the product $t \cdot \Delta\omega$ is 0.21 Å·eV.

In order to calculate the measured RAS profile in Figure 5.10 it is necessary to use $\Delta\Gamma \neq 0$ eV and $\Delta\omega = 0$. This choice is the opposite of the one discussed above. Again, we obtain a curve that resembles the measured one. However, the agreement with the experiment can be considerably improved by generalizing (5.19) to arbitrarily shifted and broadened ε curves. We have therefore evaluated the integral

$$\Delta\varepsilon_s = \varepsilon - \int \varepsilon(\omega' - \Delta\omega) f(\omega - \omega') d\omega \qquad (5.20)$$

for different broadening functions *f*. Lifetime effects and experimental broadening are described by f, which is assumed to act on the surface tensorial component for the [001] direction. A comparison with the experimental data shows that a Gaussian profile is the best choice. In (5.20) the permittivity for the $[1\bar{1}0]$ direction has been assumed to be unbroadened and identical with the bulk permittivity. Letting $\Delta\Gamma$ stand for the halfwidth of f, we find that the parameters $t \cdot \Delta\Gamma = 0.75$ Å·eV, $\Delta\omega = 0$, reproduce the experimental curve. In Figure 5.10 the results of the calculations (unbroken curve) are compared with the experimental data (filled triangles). Again, the small discrepancy is mostly due to window strain.

Surface steps and the local-field

Since the RAS profile is determined by the difference $\Delta\varepsilon_s$ it follows that although (5.20) is a simple way of reproducing the experimental RAS signal it does not need to be the correct one. Local-field calculations based on a perfect planar surface predict for example in contrast to (5.20) a sharp maximum in the surface conductivity at the absorption edge, but are nevertheless also capable of reproducing the dispersion-shaped version [44] of the signal.
It is of interest to calculate the local-field for non-planar surfaces in order to check whether the single-line RAS profile in Figure 5.11 can be reproduced. In local-field theory [19][32] the Clausius-Mossotti relation as applied to the interband component of the susceptibility is combined with a plane-wise summation of the dipole-dipole interaction $d(\mathbf{R}_{mn})$ between lattice points m and n to give the effective field. If the surface is planar the local-field depends only on the distance from the surface. The dipolar interaction can then be replaced with U_m coefficients that describe the effective interlayer interaction (see for example [30]). If the in-plane surface structure is crystallographically perfect, and the surface is plane, it has been common to speed up the calculations by mathematical methods, for example by transforming to reciprocal space. A natural first approximation to cases where steps and terraces are present at the surface would be to estimate an ensemble average of the dipole sums. Such a procedure was used in [59] to model the possible influence of vacancies at an otherwise perfect Cu(110) surface. Using STM images calculations of this type can be done in an exact, albeit time-consuming, fashion. It is possible, however, to estimate the effect of the steps in a simpler way by calculating upper limits for the local-field. In order to do this it is necessary to investigate how dipoles located far away from an arbitrary atom influence the U_m coefficients in the presence of terraces. The step topography can be characterized by the height-height correlation function

$$g(\mathbf{r}) = \delta^{-2} < z(\mathbf{r})z(0) > \tag{5.21}$$

According to the STM images the root mean square height $\delta = \sqrt{< z(0)^2 >}$ is much less than the correlation length. First, we note that since the terraces in Figure 5.9 have a finite width there has to be a cut-off in the sum over all dipolar interactions. This cut-off occurs each time a summation term involves a lattice site that is situated at one of the step edges.
We now make the reasonable assumption that the average local-field is a function of depth, or layer numbering from the surface, also when the surface is weakly stepped. As a result the

numerical evaluation of the dipole-dipole interaction coefficients should be modified according to

$$U_m = \sum_n d(\mathbf{R}_{mn}) f(\mathbf{r}_{mn})) \tag{5.22}$$

where $\mathbf{r}_{mn}$ is the surface projection of $\mathbf{R}_{mn}$. Clearly, if no surface steps are present $f(\mathbf{r}_{mn}) \equiv 1$ everywhere. If the surface is stepped the function f must be expected to have a bell-shaped profile, with $f(\mathbf{0}) = 1$. The arguments for this are as follows: the strength of the dipole-dipole interaction goes as $|\mathbf{R}_{mn}|^{-3}$. Obviously, $f \equiv 1$ as long as the lattice sites in the summation belong to the same terrace as an arbitrary reference site. However, each time an atom located just beyond a step edge is included in the sum there is a disproportionate change in the interatomic distance. It follows that the most important effect of the step structure is to *increase* the effective $|\mathbf{R}_{mn}|$ values whenever $|\mathbf{r}_{mn}| > L_c$. Here, L_c is a critical distance of the same order as the terrace width. The reduced contribution from dipoles that are located at distances $|\mathbf{r}_{mn}| > L_c$ can be taken care of by requiring that f goes to zero when $|\mathbf{r}_{mn}| > L_c$.

We now approximate L_c with the correlation length, and f with the correlation function g. This is done despite the fact that the influence of δ on the coefficients clearly are more complicated than given by (5.22). However, the approximation should nevertheless give an estimate of the change in the RAS profile for different types of step edge distributions. Calculated RAS-profiles that correspond to anisotropic and isotropic height-height correlation lengths are shown in Figure 5.12. We have summed over several quadratic grids, consisting of up to 10^5 lattice points, in order to obtain numerical values for the U_m coefficients. The curves are based on Gaussian approximations for the *g*-function. The upper, unbroken curve is obtained for a perfect correlation in the $[\bar{1}10]$ direction and an imperfect one along [001]. The halfwidth for the g-function in the latter direction was put equal to 12 nm. Halfwidths of this order should give a crude, but qualitatively correct, approximation to surface topographies of the type given in Figure 5.9 a). The result of permitting L_c to be isotropic and equal to 12 nm in *both* directions is shown by the dashed curve.

The unbroken, lower curve in Figure 5.12 shows the calculated RAS profile for a non-stepped surface, i.e. $L_c \rightarrow \infty$ in two orthogonal directions. Also this curve has been obtained by evaluating the sum (5.22) over a finite surface mesh. The overall RAS amplitude turns out to be somewhat larger than the curve that would have resulted if exact calculations of the U_m coefficients had been made. It can be seen that in comparison with the RAS curve for the non-stepped surface the most important effect of the parallel steps is to reduce the strength of the negative high-energy peak. The low-energy peak increases slightly. Isotropic disorder restores the strength of the negative high-energy peak, and there is also a reduction in the

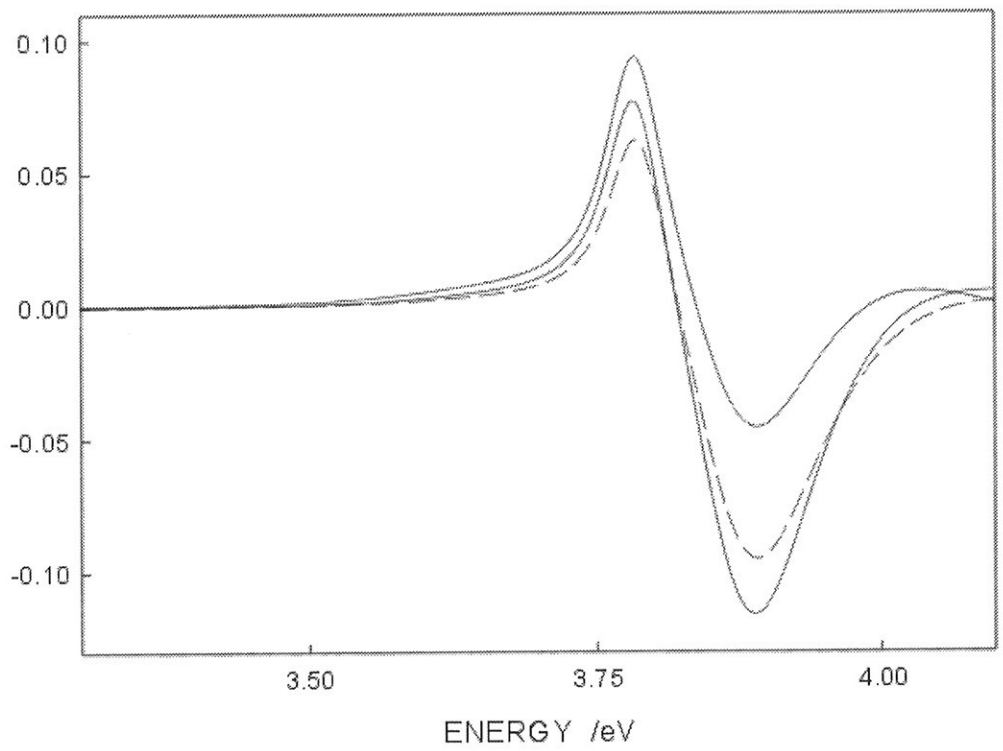

Figure 5.12. Influence of steps on the local-field for the Ag(110) surface. The upper unbroken curve is based on an anisotropic height-height correlation. (See Figure 5.9 a)) Isotropic disorder reduces the low-energy component of the RAS profile and increases the amplitude of the negative high-energy component (dashed curve). The lower unbroken curve shows the RAS signal for a planar surface, and is included for reference.

strength of the low-energy peak. Although the main trend is in partial agreement with the experimental date the effect is not very strong. The critical limit for L_c to significantly influence the signal through modification of the local-field is in the 10 – 15 nm range. Clearly, the effect would have been stronger if L_c, in contrast to the experimental situation, decreased with the development towards isotropy.

Surface plasmons

There is an alternative mechanism that operates at a longer correlation lengths than the dipole-dipole interaction does, and which in our opinion is important for the development of the RAS profile: surface corrugation with wavelengths in the 10 – 100 nm range may induce coupling between incoming photons and surface plasmons. The necessary momentum transfer is provided by the surface topography. It is well known that the intensity distribution of scattered polarized light [60][61] is modified by surface plasmons. The intensity of the specularly reflected beam is reduced [62] by $\Delta R(\omega)$, which has a maximum near the plasmon energy. Even at normal incidence, where the momentum transfer has to be larger than at oblique incidence, surface plasmons absorb energy from the incoming beam. Using both quantum perturbation theory and classical theory Elson and Ritchie [63][64] have made quantitative estimates of ΔR for normal incidence. In the absence of broadening they obtained a strongly asymmetric curve profile that peaks at the plasmon energy. A similar profile was found by Kretschmann and Kröger [65].

The reflectance drop can be calculated by redefining the permittivity as $\varepsilon \rightarrow \varepsilon + \Delta\varepsilon$, and the question arises whether $\Delta\varepsilon$ is large enough, and has the right energy, to influence the RAS signal. Clearly, if the surface dielectric function is isotropic and the step edges are unoriented the RAS signal is zero. It is of some interest to note that that propagating normally to a set of parallel edges would be able to generate a non-zero signal, even if the Ag(110) surface permittivity hypothetically were isotropic.

The possible influence of surface plasmons will now be checked in two steps: first, we assume that the intrinsic electronic surface anisotropy caused by the local-field is unmodified by the surface plasmons. In Ag, the strong RAS signal near 4 eV is generally a result of the low reflectance, caused by the fact that ε is close to unity. In a two-layer model the RAS signal is inversely proportional to the factor $(\varepsilon + \Delta\varepsilon - 1)$. This factor alone may therefore

modify the RAS profile, both when the surface steps are aligned or when they are disordered. A closer inspection shows that the positive low-energy peak is smallest when the step edges are unaligned. However, despite being in agreement with the RAS measurements the effect is too weak to explain the experimental data. Furthermore, only the permittivity within the decay length of the surface plasmon is changed by the plasmons. Near the plasmon energy this decay length is less than the penetration depth of the incoming photons [66]. It would therefore be more correct to use a three-layer model for the modelling of the dielectric structure, and the calculated effect would then be even smaller.

In a second calculational step we include the effects of the plasmons on the electronic anisotropy itself. These calculations are based on the assumption that the surface plasmons consist mainly of coherently oscillating electrons with predominantly *sp*-symmetry. Accordingly, it is mostly the Drude component of ε that is modified by the plasmon-induced reflectance drop. It is therefore necessary to modify the local-field calculations by changing the screening of the induced dipole moments that are associated by the localized interband transitions. This can be done by calculating $\Delta\varepsilon$ from published [61][63][64][65] estimates of the reflectance drop. We assume that the expression

$$\Delta R = \delta^2 \left(\frac{\omega}{c}\right)^4 \frac{[\mathrm{Re}(\varepsilon)]^2}{\{-[1+\mathrm{Re}(\varepsilon)]\}^{5/2}} \tilde{g}[|\mathbf{k}_p(\omega)|] \tag{5.23}$$

is valid for the observed monostep terraces. Here, $\tilde{g}(\mathbf{k})$ is the Fourier transform of the height autocorrelation function, and $\mathbf{k}_p(\omega)$ is the dispersion relation for the surface plasmon. The strength of (5.23) increases rapidly with decreasing L_c, which is in the $10 - 10^2$ nm range. In comparison with electron scattering experiments the moment transfers corresponding to these length scales are of order 10^{-2} Å^{-1}, or smaller. The experimentally observed split between dispersion in the two in-plane directions [52][56][67] is small, and will be neglected. It is therefore a good approximation to write the surface plasmon dispersion as

$$|\mathbf{k}_p| \equiv \frac{\omega}{c}\sqrt{\frac{\varepsilon(\omega)}{\varepsilon(\omega)+1}} \tag{5.24}$$

In order to calculate $\Delta\varepsilon$ we have to first find the phase change induced by the plasmons. This is done by evaluating the Kramers-Kronig integral

$$\Delta\theta = \frac{1}{2\pi}\int_a^b \frac{\ln|(\omega-\omega')/(\omega+\omega')|}{1-\Delta R/R}\frac{d(\Delta R/R)}{d\omega'}\,d\omega' \tag{5.25}$$

Since ΔR is localized to a small energy interval below the on-set for interband transitions, where there is a sharp cut-off in the plasmon spectrum, the integration limits a and b could be chosen relatively close to each other; 1 eV and 5.5 eV, respectively. The change in the Drude permittivity was obtained from

$$\Delta\varepsilon = \left(\frac{1-\sqrt{R-\Delta R}\exp(i(\theta-\Delta\theta)}{1+\sqrt{R-\Delta R}\exp(i(\theta-\Delta\theta))}\right)^2 - \varepsilon \tag{5.26}$$

Repeating the local-field calculations we now find that the surface plasmon significantly

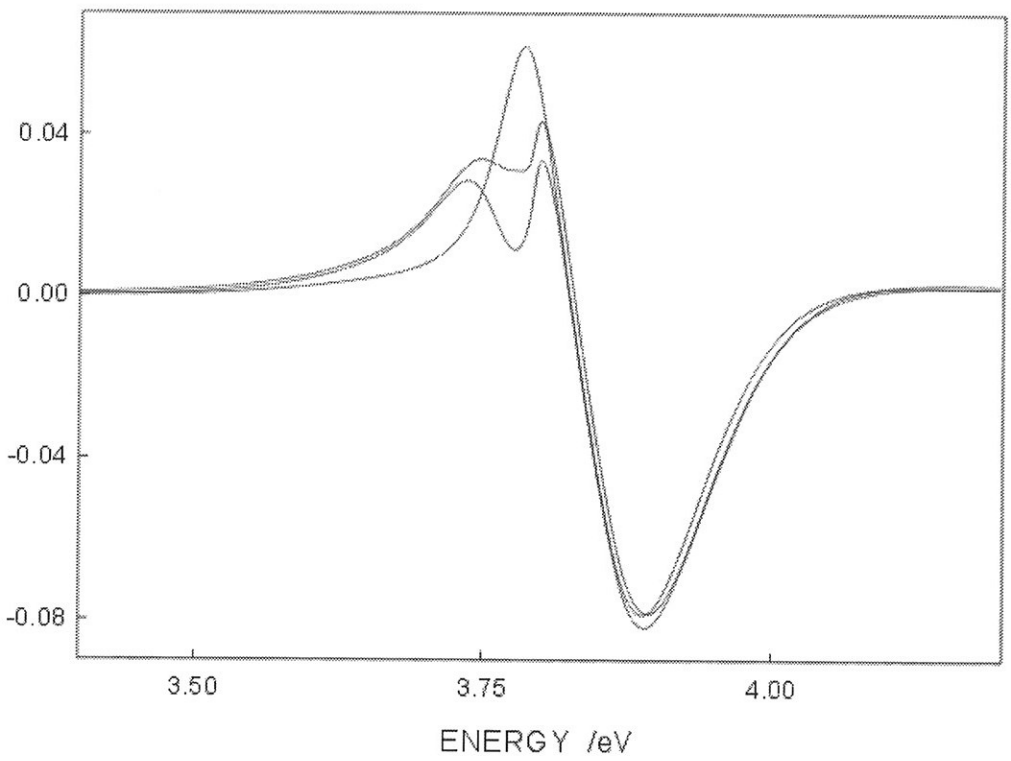

Figure 5.13. Estimate of plasmon-induced reduction of low-energy part of the RAS signal. The curve with the strongest positive peak shows the RAS profile in the absence of surface steps and surface plasmons. There is a slight reduction in the RAS intensity when steps parallel with $[1\bar{1}0]$ are present. The other curves illustrates that when the distribution of step edges is isotropic the reduction is so strong that the low-energy peak is almost obliterated. The 'extra' peak in the calculated curve is due to the choice of correlation function and the absence of lifetime effects and experimental broadening in the calculations.

influence the low-energy part of the RAS curve. The calculated profile does not critically depend on whether a two- or three-layer model is used in the calculations. However, the effect depends strongly on the choice of correlation function and the degree of broadening. Figure 5.13 shows the RAS curve obtained with a Gaussian approximation for g, and the values $\delta = 5$ nm, $L_c = 74$ nm. The RAS signal from a smooth surface is included for reference. The lower curve at the low-energy peak is valid for an isotropic distribution of step edges. There is a significant reduction in the strength of the RAS signal. If the step edges are parallell the reduction is much less, in particular if the sample surface is less corrugated. Figure 5.13 is based on identical corrugation parameters for the two cases. Note that the presence of the 'extra' double peak is due to our choice of correlation function and the absence of lifetime-effects and experimental broadening. The curves are calculated with the value 3.78 eV for the screened surface plasmon energy. This is slightly higher than 3.68 eV, the energy derived from the optically measured permittivity. Broadening, together with the experimentally observed positive dispersion [52] for Ag(110), should increase the latter energy somewhat. The positive low-energy RAS peak is in a region where it is difficult to distinguish between surface and bulk plasmons.

The curves in Figure 5.13 are presented mainly to illustrate the feasibility of the surface plasmon mediated mechanism. However, we find generally that any absorption mechanism can have a similar effect as the surface plasmons as long as its spectrum is asymmetrical with a cut-off in the 3.7 - 3.8 region. It is the position of the centroid for the induced charge density that determines the sign of the surface plasmon dispersion. To the authors' knowledge nobody has investigated in detail how the electron density profile at the surface of noble metals influences the screening of the local-field. However, it is well known that whenever the charge profile is sufficiently diffuse higher order surface multipoles [68] arise. In simple metals the energy of a surface multipole is less than the bulk plasmon energy, but larger than the surface monopole plasmon energy. It is interesting to note that electron energy loss spectroscopy recently has provided evidence [69] for the presence of a multipole plasmon mode also on Ag(110). The mode, which was not easy to distinguish from the monopole plasmon, was found at 3.72 eV. Since multipole modes are optically active [70] they are able to influence both the photo-yield and optical absorption, and it cannot be excluded that they contribute to the extinction of the low-energy RAS peak. The question remains open, however, since it has been argued [71] that the surface multipole plasmon in Ag in reality

must have an energy above the on-set for interband transitions. The reason is that the extra node in the electronic charge profile results in a very short decay length for the electric field, thereby reducing the amount of screening by d-band transitions. Calculations based on time-dependent local density approximation [71] indicated that the multipole plasmon energy should be about 7 eV.

Conclusions

A two-peaked, dispersion-shaped RAS curve is measured at room temperature when the step edges are parallell with the $[1\bar{1}0]$ direction. An isotropic distribution of steps gives instead a single negative peak. The extinction of the positive low-energy component seems to be caused by a step-induced absorption of light by surface plasmons. The limited terrace width causes a cut-off in the dipole-dipole interaction. At the experimentally observed correlation length in this work the plasmon-mediated mechanism appear to dominate.

The measurements illustrate that STM in combination with spectroscopy is useful in studies of nano-scaled structural details on metal surfaces. The technique of RAS is sensitive to the presence of surface steps and can for that reason provides information related to thermal roughening and ripple formation.

5.5 Room-temperature RAS of the clean Au(110) surface.

Summary

The reflection anisotropy spectrum of the clean Au(110) surface at room-temperature is presented. It has a broad minimum in the range 2 – 4 eV with two weak structures around 2.4 eV and 3.4 eV, respectively. The broad minimum is attributed to the screened surface local-field effect on resonant dipoles near the surface, whereas the negative peak at 2.4 eV is explained by a shift in the critical point energy of the *d*-band absorption edge of Au at the surface.

Introduction

The optical response of the outermost monolayers of a crystal can be significantly different from the response of the bulk. Reflection anisotropy spectroscopy (RAS) is a valuable and inexpensive tool for investigating this difference. Using this technique, the difference between the normal-incidence optical reflection of light polarized along the two principal axes in the surface plane can be measured as a function of the photon energy. The bulk optical properties of cubic crystals are isotropic. Any observed signal must therefore be caused by the lower symmetry of the surface.

Results for the anisotropic noble metal surfaces Ag(110) and Cu(110) have shown that features in the observed RA spectra are explained reasonably well by a local-field effect model developed by Tarriba and Mochan [15][20][23][27][30][33][43][44][59]. This model takes into account both *d* and *s-p* electrons as well as lattice geometry of the (110) surface. Resonances in the Cu(110) spectrum at 2.1 eV and in the Ag(110) spectrum at 1.7 eV were attributed to transitions between surface states, and cannot be reproduced by this model.

A natural extension of the work on Ag and Cu is to measure the reflection anisotropy of the Au(110) surface. RAS measurements of this surface under ambient conditions have been published, and the main features can be reproduced to a certain degree by local-field effect calculations [78]. In contrast, the *clean* Au(110) surface has a (1x2) reconstruction of the 'missing-row' type in room-temperature. One would therefore expect the reflection anisotropy to be different than the spectra taken under ambient conditions.

Below, we present the reflection anisotropy spectrum for the clean, (1x2) reconstructed Au(110) surface. To explain the features in the spectrum, we have calculated reflection anisotropy from a local-field effect model and a derivative model.

Experimental

The Au(110) sample was oriented to within 0.1°, polished and placed in an UHV chamber with base pressure less than $1 \cdot 10^{-10}$ mbar. A clean surface was obtained by repeated cycles of argon bombardment and annealing cycles. The energy of the argon ions was 0.5 keV, and during annealing the sample was heated to 800 K. The sample cleanliness and surface reconstruction was monitored by low energy electron diffraction (LEED). The UHV chamber is equipped with a heatable 'strain-free' window, and the sample is positioned about 30 cm from the polarisator and PEM of the RAS system. The spectra were corrected for window effects by using an isotropic Si(100) sample in the chamber as a reference.

The reflection anisotropy of Au(110), defined as

$$\frac{\Delta r}{r} = 2\frac{(r_{[\bar{1}10]} - r_{[001]})}{(r_{[\bar{1}10]} + r_{[001]})}, \tag{5.27}$$

was measured with a RAS spectrometer somewhat similar to the type described by Scholz *et al.* [22], with a spectral range of 1.2 to 5.5 eV. The system is based on a photoelastic modulator (50kHz) and is equipped with a 150-watt xenon short arc lamp as light source. Polarised light is focused on to the sample, and the reflected light is modulated, spectrally filtered, and subsequentially detected by a Si-pin-diode.

Results

Figure 5.14 shows a typical real part RA spectrum as obtained for the clean 1x2 reconstructed surface at room temperature. In the measured range the reflection anisotropy is negative with a broad minimum in the range 2 – 4 eV and two weak structures at 2.4 eV and 3.4 eV respectively. The strength of the peaks in the RA of Au(110) is larger than what is measured for Cu(110), but considerably smaller than the strength of the peaks for Ag(110). In the range 2.5 – 5 eV the spectrum has a somewhat similar *form* to the one published in [78] for a sample under ambient conditions, but the anisotropy of the clean sample is greater than the anisotropy of the sample in air. The change of the positive peak at 2.4 eV in the RA of the latter sample to a negative peak at the same energy on the clean sample is the most notable difference between the spectra.

As a first approximation in modelling the reflection anisotropy we have tried the local-field effect model of by Tarriba and Mochan [15] on an *unreconstructed* Au(110) surface. The result is shown in Figure 5.14. We have used the dielectric data for Au from Johnson and Christy [21]. The response from the screening electron gas is assumed to be a Drude dielectric function, with plasma energy $\hbar\omega_p = 9.06$ eV and relaxation time $\tau = 9 \cdot 10^{-15}$ s. In agreement with the experimental spectrum, the real part of the theoretical spectrum has a broad negative minimum in the range 2.5 – 4 eV. However, the strength of the reflection anisotropy in this

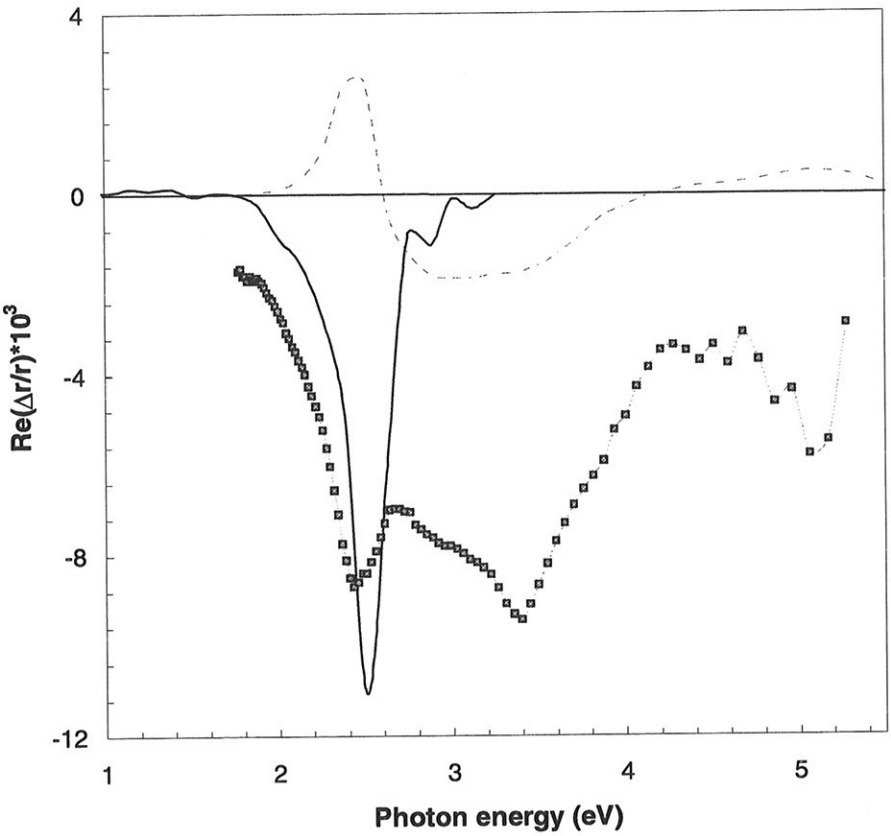

Figure 5.14 Real part of reflection anisotropy of Au(110) (1x2). Experimental spectrum (boxes), theoretical local field effect model (broken line) and critical-point shift model (solid line) with $t \cdot \Delta E = 0.14$ nm eV .

range is greatly underestimated by this theory. This is probably an effect of neglecting the missing rows on the reconstructed surface. The local-field spectrum has a positive peak at 2.2 eV, similar to the RA of the sample in air, but this peak is absent in our measured data. The theoretical spectrum describes the RA of the sample in air significantly better than the RA of the clean reconstructed sample. This can be due to the reconstruction itself, but from similar conclusions for the Ag(110) and Cu(110) surfaces, one can ask whether the local-field effect model best describes oxidised surfaces. One reason can be that the abrupt transition to zero in the electron density on the surface used in the model is closer to the situation for metal surface with an oxide layer on top.

To explain the feature at 2.4 eV we note that this energy is close to the critical point energy of the onset of interband transitions for Au (see Section 1.2 and Figure 1.2). Assuming a model of an anisotropic film of thickness t on top of an isotropic substrate, the reflection anisotropy is given by [27]

$$\frac{\Delta r}{r} = \frac{4\pi i t}{\lambda} \frac{\Delta \varepsilon_s}{(\varepsilon_b - 1)} . \tag{5.28}$$

Here $\Delta\varepsilon_s$ is the anisotropy of the dielectric function of the film and ε_b is the bulk dielectric function. If there is a difference ΔE in the critical point energy of the $[1\,\bar{1}\,0]$ and the [001] direction of the surface, and an anisotropy $\Delta\Gamma$ in the broadening of the onset, then for interband transitions the anisotropy of the dielectric is

$$\Delta\varepsilon_s = \frac{\partial \varepsilon_b}{\partial E}(\Delta E + i\Delta\Gamma). \tag{5.29}$$

The reflection anisotropy takes the form

$$\frac{\Delta r}{r} = \frac{4\pi i E t}{hc} \frac{(\Delta E + i\Delta\Gamma)}{(\varepsilon_b - 1)} \frac{\partial \varepsilon_b}{\partial E} . \tag{5.30}$$

A range of values for t, ΔE and $\Delta\Gamma$ can produce a structure around the critical point energy in the reflection anisotropy. In Figure 5.14 the result of this model with $t \cdot \Delta E = 0.14$ nm eV and $\Delta\Gamma = 0$ is shown. It follows from the figure that the peak at 2.4 eV can be explained reasonably well as a shift in the d-band absorption edges for the top surface layer. Note that in this phenomenological model the difference between the unreconstructed and reconstructed surface is included in the film thickness and energy shift parameters.

Conclusions

We have demonstrated that the anisotropy of the clean reconstructed Au(110) 1x2 surface in the range 1.5 – 5 eV can be attributed to at least two different effects. The screened surface local-field effect on resonant dipoles located near the surface results in a broad negative anisotropy in the range 2.5 – 4 eV. In addition, a shift in the critical point energy of the onset of *d*-band to Fermi level interband transition produces a negative peak at 2.4 eV. The structure at 3.4 eV is not explained by these models.

5.6 Ras of Pt(100) and Au(100)

Summary

Reflection anisotropy spectra of the clean, pseudo-hexagonally reconstructed Pt(100) and Au(100) surfaces are presented. The main feature in the Au(100) spectrum is a peak at 2.5 eV. It is demonstrated that this resonance originates from a difference in the *d*-band absorption edge in the dielectric function between the two principal axes of the surface layer. The clean reconstructed Pt(100)-hex-R0.7° surface has a reflection anisotropy spectrum with a broad negative peak at 3.5 eV, contrary to previously measured results. This spectrum can be modelled reasonably well by an effective medium model.

Introduction

The clean (100) surfaces of Au, Pt and Ir have similar complex reconstructions, a wave-like quasi-hexagonal structure on top of the square lattice [76][79]. For Au(100), interaction of the dense top hexagonal layer with the underlying unreconstructed crystal planes produces a large unit cell, recently estimated to be close to (28x5) [80]. The five-fold periodicity originates from the stacking of six [011] rows on top of five rows in the second layer. In the orthogonal direction the large periodicity is a result of a small contraction along the [011] rows. On the Pt(100) surface, two hexagonal phases occur depending on the surface preparation procedure, namely the metastable Pt(100)-hex and the Pt(100)-hex-R0.7° reconstructions [81]. The latter structure has a surface unit cell (Nx5), where N =12-14, slightly rotated with respect to the square lattice in the substrate. For both surfaces, the nearest neighbour distance within the surface layer is compressed by 4% compared to the nearest neighbour distance in the bulk [82]. This observation supports the idea that the reconstructions of the (100) surfaces of Au and Pt are driven by the relief of surface stress.

A large part of the work on reflection anisotropy spectroscopy on metals has devoted to the anisotropic (110) noble metal surfaces [20][23][27][30][32][33][43][44][59]. The reconstructed (100) surfaces of Au and Pt are anisotropic with an isotropic bulk, and are also suitable for RAS experiments.

Experimental

We measured the reflection anisotropy

$$\frac{\Delta r}{r} = \frac{(r_{\parallel} - r_{\perp})}{(r_{\parallel} + r_{\perp})/2}, \tag{5.31}$$

of a reconstructed Pt(100) surface and a reconstructed Au(100) surface. Here $r_{\parallel}$ and $r_{\perp}$ are the reflectivity parallel and normal to the longest axis in the surface unit cell respectively. The platinum sample used is identical to the one used in [76]. The RAS measurements were performed in an UHV chamber with base pressure less than $1 \cdot 10^{-10}$ mbar. To obtain a clean surface the samples were prepared by several sputtering and annealing cycles. The energy of the argon–ions used in sputtering was 500 eV, and the sputtering current was approximately 5 $\mu A/cm^2$. During annealing the Au sample was heated to 900 K for 15-60 min, and the Pt sample was heated to 1100 K in an oxygen partial pressure of 10^{-7} mbar for up to two hours. The quality of the sample structure and reconstruction was monitored by low-energy electron diffraction (LEED). In addition, the Pt sample was measured by scanning tunnelling microscopy (STM) to check the quality of the surface. LEED was used to check that a large area of the surfaces was reconstructed as a single domain.

The RAS spectrometer is of the type described by Scholz *et al.* [22], with a spectral range of 1.5 to 5.5 eV. Light from a 150-watt xenon short arc lamp is polarised and focused on the sample surface. The reflected beam passes through a photoelastic modulator (50kHz), a polariser (analyser), and a monochromator in front of a silicon pin diode detector. The polarisers are of the Rochon type. In order to keep window effects as small as possible a low-strain UHV window was used. In addition, the spectra were corrected for windows effect by using an isotropic Si(100) sample in the chamber as a reference. To reduce the possibility of measuring multiple reconstruction domains, the spot-size on the sample was minimised.

Au(100)

The reflection anisotropy as defined in (5.31) of the clean reconstructed Au(100) surface is shown in Figure 5.15. The most dominant feature is the negative peak at 2.5 eV. In addition, there are two weak positive structures at 1.9 eV and 4.3 eV. The reflection anisotropy of the main features is generally weaker than what is measured for Au(110) (see Section 5.5), Cu(110) and Ag(110) [30][44]. Contribution to the spectrum from multiple domains with different orientation of the reconstruction can reduce the measured reflection anisotropy, but will in general not influence the *profile* of the measured curve. Although, as explained above, precautions were taken to minimise this effect, the strength of the anisotropy in our measurement is somewhat uncertain.

The main negative peak at 2.5 eV is close to the critical-point energy in the dielectric function of Au, corresponding to the onset of *d*-band to Fermi-level transitions (see Figure 1.2). Similar to the case of Au(110) and Ag(110) [27], we assume a model of an anisotropic film of thickness t on top of an isotropic substrate. If there are an anisotropy ΔE in the critical point energy of the dielectric function and an anisotropy $\Delta\Gamma$ in the broadening of the absorption edge, the reflection anisotropy can be written

$$\frac{\Delta r}{r} = \frac{4\pi i E t}{hc} \frac{(\Delta E + i\Delta\Gamma)}{(\varepsilon_b - 1)} \frac{\partial \varepsilon_b}{\partial E} \quad , \tag{5.32}$$

where $\varepsilon_b(E)$ is the bulk dielectric function. Figure 5.15 shows a comparison between the

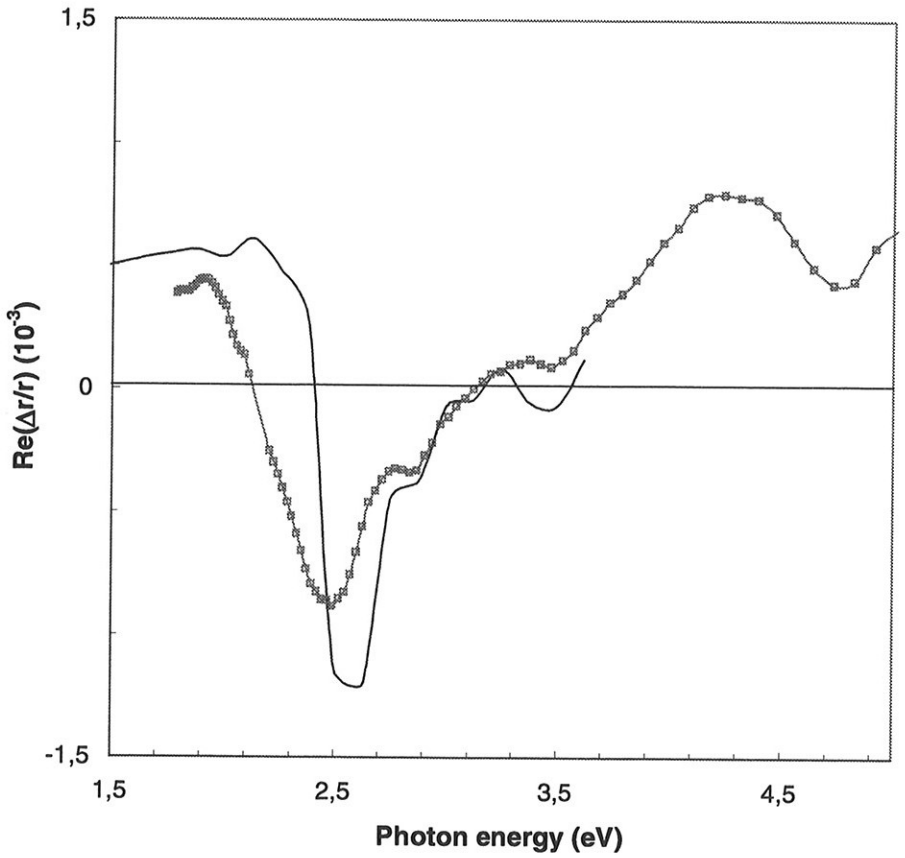

Figure 5.15 Real part of RAS of Au(100). Experimental values (boxes) and critical-point shift model with $t \cdot \Delta E$ = 0.02 nm eV and $t \cdot \Delta\Gamma$ =-0.02 nm eV (solid line).

measured reflection anisotropy and a calculated curve using this model with $t \cdot \Delta E = 0.02$ nm eV and $t \cdot \Delta \Gamma = -0.02$ nm eV. The dielectric data for gold are from Johnson and Christy [21]. For a top layer thickness of $t = 0.4$ nm this corresponds to a value for the energy shift of $\Delta E = 0.05$ eV. The calculated spectrum reproduces the experimental curve reasonably well in the range 1.8 eV – 3.5 eV. The positive feature around 4.3 eV is not reproduced by this model for any reasonable values for ΔE and $\Delta \Gamma$.

Pt(100)

Reflection anisotropy spectra for the clean reconstructed Pt(100) surface have already been published by Borg *et al.* [73]. Their vacuum chamber was equipped with a glass window, and the spectra are therefore restricted to energies below 4 eV. We have performed measurement on the same sample in the same UHV chamber as Borg *et al.*, but this time the chamber was

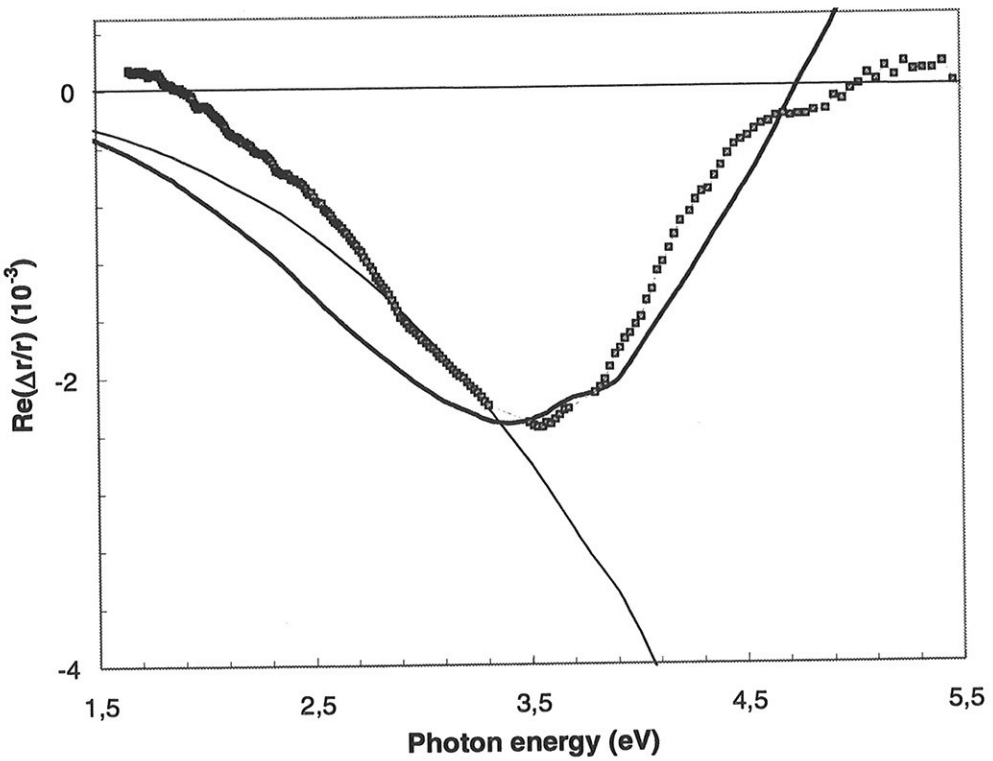

Figure 5.16 Real part of the reflection anisotropy of Pt(100)-hex-R0.7°: experimental values (squares), Wiener effective-medium model (thin solid line) and Bergman effective-medium model (thick solid line).

equipped with a low-strain window to reduce windows-effects. Figure 5.16 shows our result for the real part of reflection anisotropy as defined in (5.31) for Pt(100)-hex-R0.7°. The anisotropy is negative with a broad peak at 3.6 eV. The strength of the peak is of the same order as for Au(100), Au(110) and Cu(110) [30][44]. In the energy range up to 3.5 eV the spectrum is similar to the previous published result. However, at 3.5 eV, our curve has a minimum, whereas the previous published curve shows no sign of a minimum near the end of the measured range at 4 eV.

To give a theoretical explanation of their measurements, Borg *et al.* [73] used an effective-medium model based on a surface layer of Pt grooves on top of a Pt(1x1) isotropic substrate. The reflection anisotropy is given by [27]

$$\frac{\Delta r}{r} = \frac{4\pi i t}{\lambda} \frac{\Delta \varepsilon_s}{(\varepsilon_b - 1)} , \tag{5.33}$$

where $\Delta\varepsilon_s$ is the anisotropy of the dielectric function of the film of thickness t. With a filling factor of 0.5, the dielectric constants of the top layer is given by the Wiener bounds [83]:

$$\varepsilon_{\|b} = (\varepsilon_b + 1)/2 , \tag{5.34}$$

$$\frac{1}{\varepsilon_b} = (\frac{1}{\varepsilon_b} + 1)/2 . \tag{5.35}$$

Here $\varepsilon_\perp$ and $\varepsilon_\|$ are the dielectric function in the direction normal to and parallell with the grooves. Inserting these values into (5.33) we get for the reflection anisotropy

$$\frac{\Delta r}{r} = \frac{2\pi i t}{\lambda} \frac{(\varepsilon_b - 1)}{(\varepsilon_b + 1)} . \tag{5.36}$$

Using different dielectric data for Pt than in the previous published result, we have calculated the real part of the reflection anisotropy [86][87]. The result is shown in Figure 5.16. It is clear from the figure that this model does not describe the anisotropy very well. In fact, the theoretical curve has a minimum that is not shown at 6 eV of $-25 \cdot 10^{-3}$. However, the minimum value and the slope of the curve depend on the chosen thickness t of the surface layer.

We can now proceed by applying the surface dipole model of Mochan and Barrera [32] to the Pt(100) surface. However, the complexity of the reconstruction of the surface complicates the dipole calculations. Instead we model the wave-like surface reconstruction as an effective medium with ellipsoids along the grooves with size about the order of the unit cell. From

Kantor and Bergman [88] it is clear that $\varepsilon_{\perp}$ and $\varepsilon_{\parallel}$ then can be expressed as spectrum of oscillations depending only on the geometry of the ellipsoids. If there are resonances $Z_{\perp}$ and $Z_{\parallel}$ in directions normal to and parallell with the ellipsoids, and their relative strength is F, then the reflection anisotropy is

$$\frac{\Delta r}{r} = \frac{4\pi i t}{\lambda} \frac{1}{(\varepsilon_b - 1)} \left(\frac{(\varepsilon_b - 1)}{(\varepsilon_b + Z_{\perp})} - F \frac{(\varepsilon_b - 1)}{(\varepsilon_b + Z_{\parallel})} \right) \tag{5.37}$$

The resulting reflection anisotropy spectrum is shown in Figure 5.16 for $Z_{\perp} = 6.5$, $Z_{\parallel} = 3.5$ and $F = 0.6$. It is seen from the figure that this model reproduce the measured spectrum reasonably well.

Conclusions

It is clear that the main feature at 2.5 eV of the optical reflection anisotropy of the clean wave-like reconstructed Au(100) surface originates from the anisotropic dielectric function of the outermost surface layer. With a small shift in the *d*-band absorption edge of $\Delta E = 0.05$ eV together with a reduced broadening of the absorption edge for the direction along the rows of atoms, we are able to reproduce the measure anisotropy in the range up to 3.6 eV.

For the clean reconstructed Pt(100)-hex-R0.7° surface we have shown that the anisotropy has a broad negative peak at 3.5 eV, contrary to previous measured results. In addition, our results show that the effective medium theory with a surface optical response given by Wiener bounds is not appropriate to describe the measured spectrum for Pt(100). However, it is possible to model the measured spectrum by an effective medium with ellipsoids along the surface.

5.7 Anisotropy of the clean and oxygen reconstructed Ni(110) surface.

Summary

Reflection anisotropy spectra of the clean, (2x1) oxygen reconstructed and (3x1) oxygen reconstructed Ni(110) surface are presented. We apply a classical local field effect model to the surface, but find that it cannot fully reproduce the measured spectra. The same is true for a more phenomenological model where it is assumed that the reflection anisotropy spectrum is due to a surface-induced shift in the dielectric function.

Introduction

Adsorption of oxygen on Ni(110) generates ordered (2x1) domains. This requires a substantial reorganisation of the surface with a 1/4 monolayer of nickel atoms being displaced to new positions. The p(2x1) structure of Ni(110) has been the subject of several structural surface studies [31][72]. Of several models, the oxygen-induced (2x1) reconstructed missing-row model of the surface is generally accepted. When the surface is exposed to O_2 at room temperature, metal-oxygen rows grow parallel to the [001] direction [31], until a coverage of 0.5 monolayer. Further exposure to O_2 initially induces a (3x1) reconstructed surface, and finally a saturated (2x1) reconstructed surface is obtained

Recently, reflection anisotropy spectroscopy (RAS) studies of the Pt(100), Ag(110) and Cu(110) surface has proved that the application of this technique can give interesting information about electronic properties of metal surfaces [23][27][30][33][73]. For both the silver and copper surface, local field effects at the lattice sites can explain dominant features of the spectra. Peaks at 2.1 eV for Cu(110) and at 1.7 eV for Ag(110) originate from transitions between occupied and unoccupied surface states.

Experimental

The reflection anisotropy,

$$\frac{\Delta r}{r} = 2\frac{(r_{[\bar{1}10]} - r_{[001]})}{(r_{[\bar{1}10]} + r_{[001]})}, \tag{5.38}$$

of a clean and oxygen reconstructed Ni(110) surface was measured as a function of photon energy in the visible and UV wavelength range. The sample, oriented to within 0.1° and

polished by the manufacturer, was located in an UHV chamber with base pressure below $1 \cdot 10^{-10}$ mbar. Several (~40) cycles of 15 - 25 minutes of Ar^+ ion bombardment and 15 - 45 minutes of annealing at 900 K were used to clean the sample. The energy of the argon-ions was 500 eV, and the ion current about 5 $\mu A/cm^2$. In addition, the sample was repeatedly exposed to oxygen (10^{-7} – 10^{-8} mbar) at elevated substrate temperature to remove carbon contamination. The quality of the surface structure was monitored by LEED and RAS. The reproducible procedure for obtaining the different reconstructions was: i) Exposure of the clean surface to 3 L of oxygen produced a Ni(110)-p(2x1)O surface. ii) Further exposure to 4 L of oxygen created a (3x1)O reconstruction. iii) Exposure of the (3x1)O reconstructed surface to 4 L or more of oxygen generated another (2x1)O reconstruction.

The applied RAS spectrometer used for the measurement is similar to the type described by Scholz *et al.* [22], with a spectral range of 1.1 to 5.5 eV. A 150-watt xenon short arc lamp is used as light-source, and a polarised beam is reflected from the sample, modulated by a photoelastic modulator (50kHz), and then analysed to give intensity variations directly proportional to the reflection anisotropy. Both the polariser and analyser are of the Rochon type. A single-grating monochromator connected to a silicon pin diode detector is used to measure this variation and its photon energy dependence. The UHV chamber is equipped with low-strain windows, and a Si(100) sample mounted on the back of the manipulator arm was used to correct for the background spectra.

Results and discussion

The real and imaginary part of the reflection anisotropy as defined in (5.38) for the clean Ni(110) surface are shown in Figure 5.17. All spectra presented here are corrected with respect to window-effects. The real part is negative in the range 1.7 – 5.5 eV, and has a broad negative peak at 3.0 eV. The imaginary part is also negative with the most prominent feature at 4.5 - 4.7 eV. In addition, there is a weak structure at 1.85 eV. There is no clear counterpart around 3.0 eV in the imaginary part to the broad peak in the real part of the reflection anisotropy. Similarly, the features mentioned above in the imaginary part of the reflection anisotropy have no clear counterparts in the real part of the spectrum. From Figure 5.17 it is clear that the reflection anisotropy of Ni(110) continues to be negative in the energy range below 1.7 eV.

In order to explain the measured spectra we apply the surface dipole model of Mochan and Barrera [32] to the nickel surface. Some of the assumptions in this model may not hold for nickel. For example, the electron configuration of Ni, $[Ar]3d^8 4s^2$, implies that the *d*-shell is not completely filled up. In addition, it is difficult to determine a definite plasma frequency and relaxation time for nickel. Nevertheless, we show in Figure 5.18 the results of the local-field effect model with a plasma-energy $\hbar\omega_p = 9$ eV and relaxation time $\tau = 5 \cdot 10^{-15}$ s. The *shape* of the calculated curve in the range up to 4 eV is in some agreement with the measured curve. The calculations predict a broad minimum at 3.2 eV, not far from the minimum of the measured data. Furthermore, the calculated spectrum is negative to well below 1.7 eV, similar

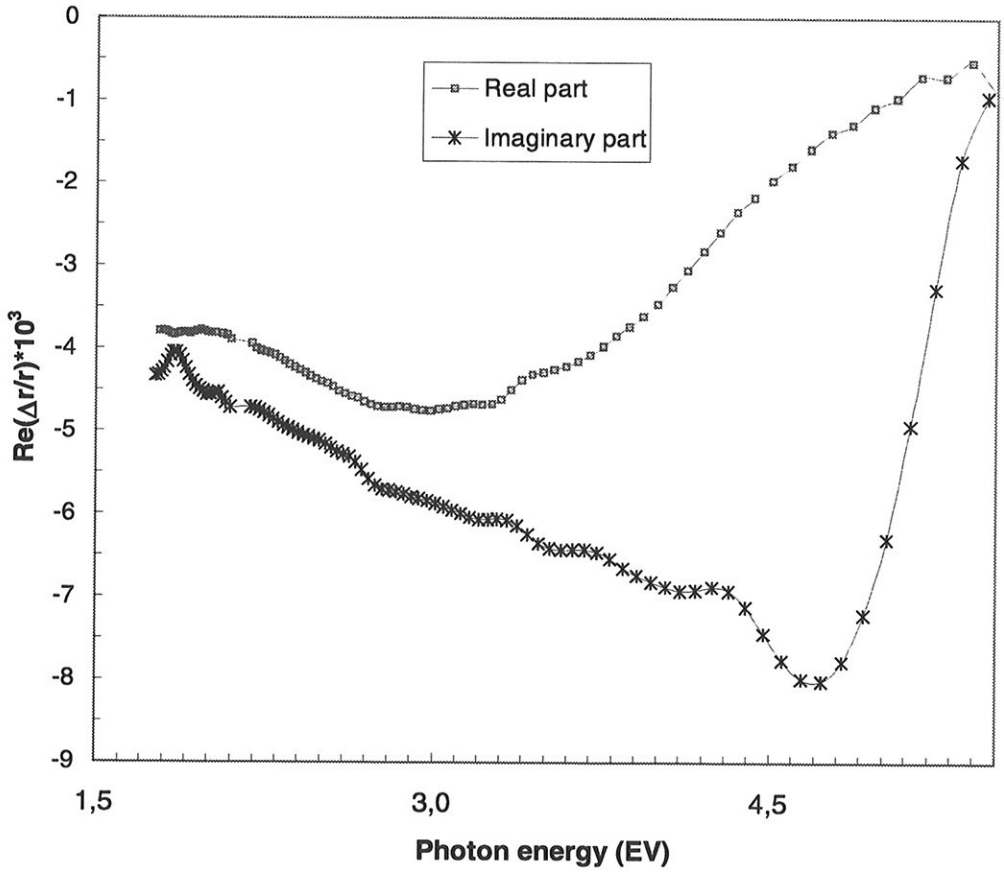

Figure 5.17 Real part (top) and imaginary part (bottom) of reflection anisotropy of the clean Ni(110) surface.

to the measured RAS. On the other hand, the amplitude of the anisotropy in the range up to 4 eV is underestimated by a factor of five, and the positive peak at 4.0 eV is absent in the measurements.

Fernandez *et al.* [27] interpreted the spectra of Ag(110) in a more phenomenological way. Assuming that the surface can be modelled as an anisotropic film of thickness t on top of an isotropic substrate, the reflection anisotropy is given by

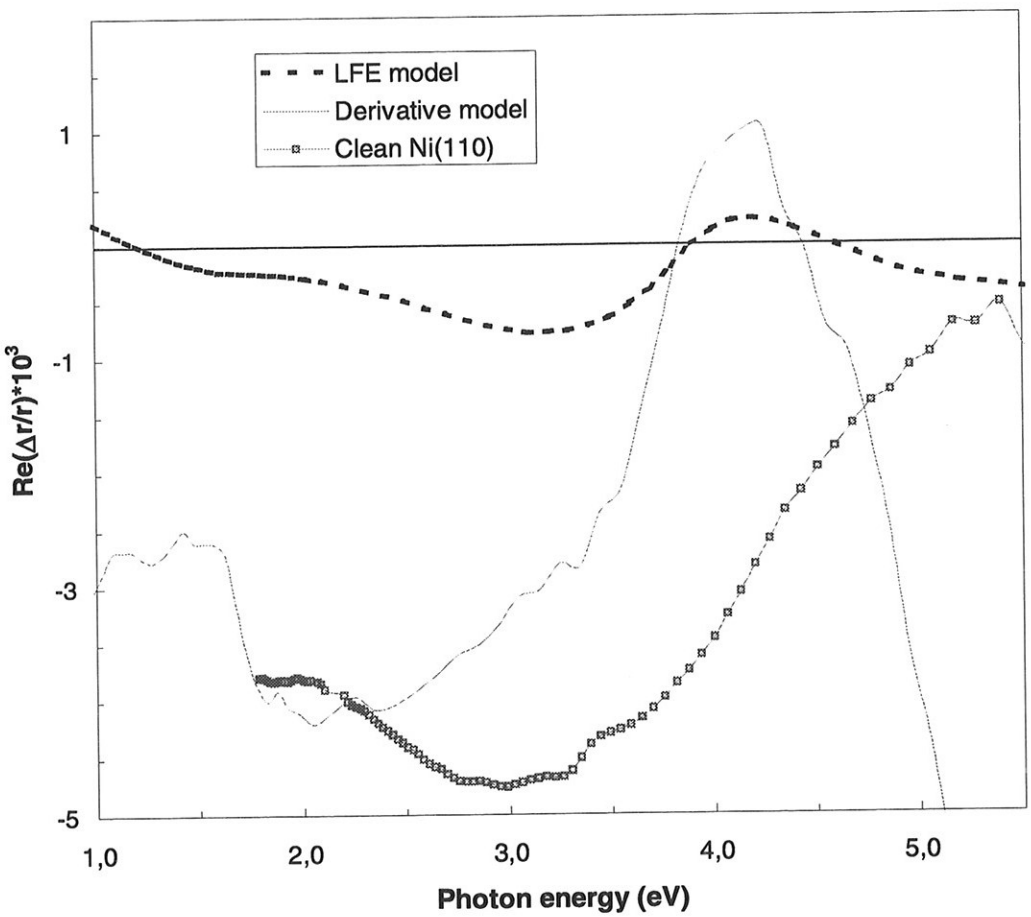

Figure 5.18 Comparison of the real part of measured reflection anisotropy (boxes) with local-field effect model (broken line) and derivative model (solid line). The local-field effect spectrum was obtained using plasma energy $\hbar\omega_p = 9$ eV and relaxation time $\tau = 5 \cdot 10^{-15}$ s. The derivative model is calculated with $\Delta E = 0$ and $t \cdot \Delta\Gamma = 0.24$ nm eV. The permittivity data used are from Palik [50].

$$\frac{\Delta r}{r} = \frac{4\pi i t}{\lambda} \frac{\Delta \varepsilon_s}{(\varepsilon_b - 1)} \,. \tag{5.39}$$

Here $\Delta\varepsilon_s$ is the anisotropy of the dielectric function of the film and ε_b is the bulk dielectric function. If the dielectric function at a critical point is slightly shifted in energy a non-zero $\Delta\varepsilon_s$ results. To first order the reflection anisotropy is

$$\frac{\Delta r}{r} = \frac{4\pi i E t}{hc} \frac{(\Delta E + i\Delta\Gamma)}{(\varepsilon_b - 1)} \frac{\partial \varepsilon_b}{\partial E} \,, \tag{5.40}$$

with ΔE as the difference in the critical point energy between the $[1\,\bar{1}\,0]$ and the [001] direction of the surface, and $\Delta\Gamma$ as the anisotropy of the broadening. The dielectric function of nickel has a critical point at 4 eV [50]. In Figure 5.18 the result of this derivative model is shown for $\Delta E = 0$ and $t \cdot \Delta\Gamma = 0.24$ nm eV. Alternative values for ΔE and $\Delta\Gamma$ did not improve the calculated curve significantly. Interestingly, the curve has a somewhat similar shape as the measured curve in the range up to 4 – 4.5 eV. However, the calculated curve seems to be shifted –0.8 eV with respect to the measured data. In addition, the main feature at 2.2 eV is more pronounced than the broad minimum at 3.0 eV in the measured spectrum. Above 4.5 eV the derivative model deviate significantly from the measured data.

To inspect to what degree the Ni(110) surface is influenced by oxygen, we recorded RA spectra for the oxygen-reconstructed surfaces (2x1)O, (3x1)O and (2x1)O II. These were obtained in sequence as explained above. Figure 5.19 shows the difference between the spectra for the reconstructed surfaces and the clean surface. The difference spectra are positive with a peak around 3.0 eV. It can be seen that the broad minimum of the clean surface at 3.0 eV, also reproduced by the theoretical models, disappears when the surface is reconstructed. The (2x1)O and (2x1)O II difference spectra are almost identical, whereas the anisotropy of the (3x1)O reconstructed surface is slightly different from the two other reconstructed surfaces above 2.8 eV. We have at this stage no definite explanation for the absence the peak at 3.0 eV. However, it is *possible* that the peak in the difference spectra arises from transitions between surface states. At the $\bar{Y}$ point of the surface Brillouin zone, nickel has a surface state at 2.4 eV above the Fermi-level. In addition, a surface state may exist just below the Fermi-level [84][85]. If a transition between these states is allowed and polarisation dependent, then we would expect a feature in the reflection anisotropy spectrum around 3.0 eV. Similar type of resonances have been observed for Ag(110) and Cu(110) [23][30].

Figure 5.20 shows the remarkable change in reflection anisotropy at 3.0 eV during oxygen exposure. When oxygen is added to the UHV chamber, the peak at 3.0 eV disappears very fast. At the maximum of the curve in Figure 5.20, the surface is (2x1)O reconstructed. Subsequent oxygen exposure produces only a small change in reflection anisotropy, until the (2x1)O II reconstruction is reached after 10 L.

Conclusions

In conclusion, we have shown that the observed reflection anisotropy of the clean and oxygen reconstructed Ni(110) surfaces only partially can be explained by the screened local-field

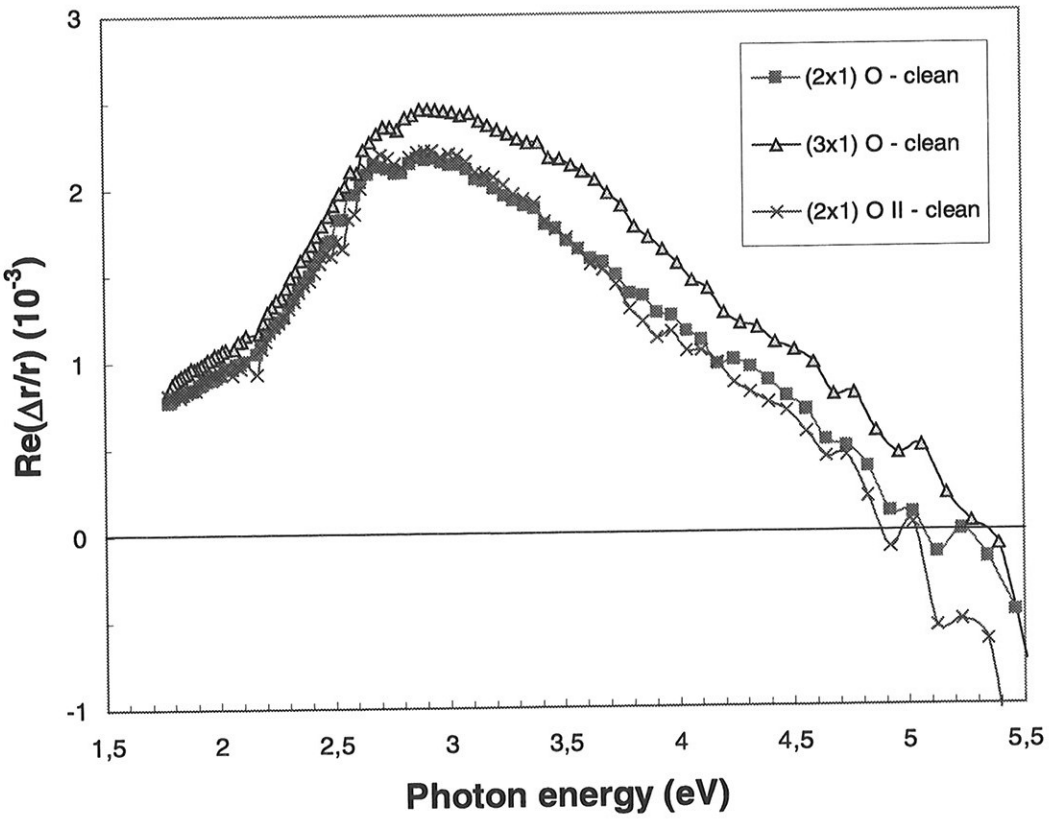

Figure 5.19 Difference in the reflection anisotropy between the reconstructed surfaces (2x1)O (boxes), (3x1)O (triangles), (2x1)O II (crosses) and the clean surface,

effect on resonant dipoles near the surface or by a difference in critical-point energy between the two crystallographic axes of the surface.

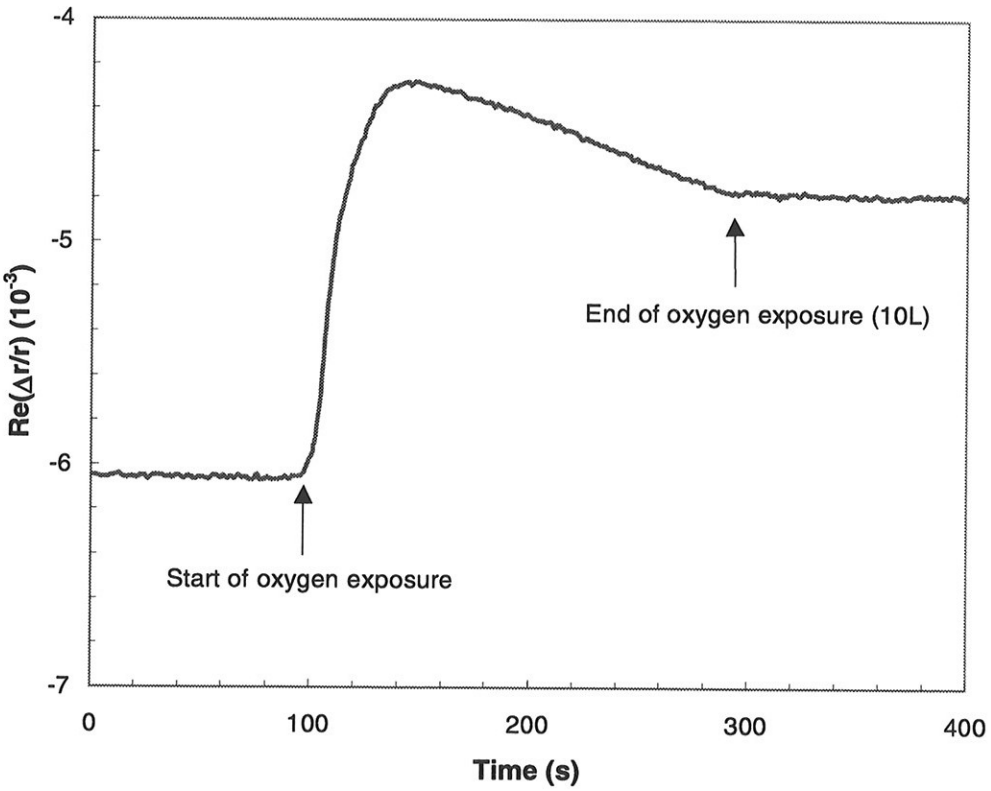

Figure 5.20 Time-dependent reflection anisotropy of Ni(110) at 3.0 eV during oxygen exposure of 10 L.

Appendix A. Useful RAS expressions

- The RAS intensity to the first order:

$$\frac{\Delta I}{\bar{I}} = 2\left(-\mathrm{Im}\frac{\Delta r}{\bar{r}} - 2a_p - \delta_1 \sin 2\theta_1 + \delta_2 \sin 2\theta_2\right) J_1(\delta_m)\sin \omega_{PEM} t$$
$$+2\left(-\mathrm{Re}\frac{\Delta r}{\bar{r}} - 2\Delta P - 2\Delta M\right) J_2(\delta_m)\cos 2\omega_{PEM} t \qquad \text{(A.1)}$$

- The relation between the real part of the reflection anisotropy and the measured signal:

$$\mathrm{Re}\left(\frac{\Delta r}{r}\right) = \frac{\sqrt{2}}{2J_2(\delta_{PEM})} \times \frac{\Delta U_{2\omega}}{U_{dc}}$$
$$= \begin{cases} 2.2355 \times \dfrac{\Delta U_{2\omega}}{U_{dc}}, & \delta_{PEM} = 1.8423\,(106°), \quad J_1^{\max} \\ 1.5299 \times \dfrac{\Delta U_{2\omega}}{U_{dc}}, & \delta_{PEM} = 2.6298\,(151°), \quad J_1 = J_2 \\ 1.4544 \times \dfrac{\Delta U_{2\omega}}{U_{dc}}, & \delta_{PEM} = 3.0521\,(175°), \quad J_2^{\max} \end{cases} \qquad \text{(A.2)}$$

- The relation between the imaginary part of the reflection anisotropy and the measured signal:

$$\mathrm{Im}\left(\frac{\Delta r}{r}\right) = -\frac{\sqrt{2}}{2J_1(\delta_{PEM})} \times \frac{\Delta U_{\omega}}{U_{dc}}$$
$$= \begin{cases} -1.2162 \times \dfrac{\Delta U_{\omega}}{U_{dc}}, & \delta_{PEM} = 1.8423\,(106°), \quad J_1^{\max} \\ -1.5299 \times \dfrac{\Delta U_{\omega}}{U_{dc}}, & \delta_{PEM} = 2.6298\,(151°), \quad J_1 = J_2 \\ -2.2139 \times \dfrac{\Delta U_{\omega}}{U_{dc}}, & \delta_{PEM} = 3.0521\,(175°), \quad J_2^{\max} \end{cases} \qquad \text{(A.3)}$$

- The relation between the wavelength of light and photon energy:

$$E_{foton}(eV) = \frac{1239{,}81}{\lambda_{lys}(nm)} \qquad \text{(A.4)}$$

Appendix B. UHV chamber components

The following table lists the name and type of some of selected components of the UHV chamber dedicated to RAS measurements.

Table B.1. UHV chamber components

Component	Brand and model	Flange	Temperature maximum
LEED	Phi 15-120	DN150CF	
Turbomolecular pump	Pfeiffer-Balzers TSU 332	DN100CF	160°C on flange
Ion-gun for sputtering	VSW AS10-C	DN35CF	200°C
Ion pump	Varian Triode 110 l	DN150CF	350°C
Valve	VAT 10840*E01/08	DN100CF	250°C open, 200°C closed
Low-strain windows	Bomco B6456	DN63CF	400°C
	Bomco B5936	DN35CF	400°C
Titan sublimation pump	Varian	DN100CF	
Manipulator	Varian HPM 9810523	DN100CF	250°C
Manometer	Varian	DN35CF	
Manometer	Varian UHV-24	DN35CF	450°C
Mass spectrometer	VG Anavac-2	DN35CF	250°C

Appendix C. RASLab log file

Every measurements and PEM calibration performed with RASLab creates a log-file similar to the following:

```
Starting simple RAS measurement procedure
Date: 08.05.98 , Time: 11:58:44
Parameters:
Number of scans: 1
Number of samples: 40
Start wavelength (nm): 230
End wavelength (nm): 702
Wavelength step (Å): 20
Number of points: 236
Maximum PEM phase shift: 3.0521
Time between each sample: 15 ms
Lock-in timeconstant: 900
Lockin sensitivity: 10 mV
ADC channel for DC part of signal: 5
Photo amplifier will be adjusted automatically
Values will not be autofiltered at Xe 570nm line
Values will be saved to file c:\Raslab 3\Log\RAS Ag(110) real  080598
1158.log
Monochromator is moved from start to end (increasing wavelength)
Real part of RAS
Correction factor: 1.4535
Kommentar:

Starting scan nr. 1

Pnr. Wl(nm) E(eV)     RAS        Std.Dev.   Int       Abs.RAS   Neg.RAS   Amp.
0    230.0  5.38960  -0.90721   1.76333    0.06430   -0.62417  0.90721   100
1    232.0  5.34420  0.65516    1.82090    0.07324   0.45076   -0.65516  100
2    234.0  5.29871  -1.67171   0.66238    0.08581   -1.15016  1.67171   100
3    236.0  5.25398  -1.82443   0.54382    0.10041   -1.25523  1.82443   100
...
...
...
Maximum RAS:          3.39152
Minimum RAS:          -26.49014
Maximum intensity:    6.88737
Minimum intensity:    0.00000
Measurement finished
```

Appendix D. RAS measurement procedure

In this section a detailed procedure for doing a RAS measurement using our set-up is given as a reference. Only the optical system, the electronic equipment and the RASLab software are described here. Operation of the vacuum chamber, cleaning of samples, etc. is left out, as is detailed information about the instruments.

D.1 Starting the instruments

This procedure should be executed before the first measurement of the day.

Starting the xenon arc lamp.

The xenon arc lamp should be the first instrument to be turned on, because of the strong ignition voltage pulse. If a projector lamp is used, it can be started at a later point.

a) Free the detector from the photoamplifier by unplugging the bayonet plug at the amplifier side.
b) Free the photoelastic modulator from its electronic driver by unplugging the BNCs marked **gauge input** and **drive output.**
c) Start the electronic fans, both at the laboratory wall and at the lamp, and check that the ventilation tube for ozone is in position. Check that the appropriate voltage (~12 V) is connected to the electronic fan at the lamp.
d) Check that all cables between lamp power source and the lamp are connected and securely screened.
e) Check that the xenon arc lamp is in vertical position (±15°).
f) Start the arc lamp by pressing the red button, and thereafter pressing a single time on the black start button. When the lamp is on, check that the current is 7.5 A.
g) Mount the PEM to its driver. Check that the BNC connector with a capacitor is plugged into the gauge input.
h) Plug in the bayonet plug of the photoamplifier.

D.2 Start of the electronic components

When the xenon lamp is started, the rest of the electronics should be turned on.

a) The lock-in amplifier needs time to warm up, and it should therefore be turned on at least 5 minutes, preferably 30 minutes, before the measurement. Check that the input from the photoamplifier is in the right channel.

b) The amplifier for the photodiode detector needs at least 10 minutes warm-up time, and is turned on by the main plug. Check that the green light on top of the amplifier is lit.

c) The stepmotor driver is turned on by following the receipt on the front panel. Check that the current-knob on the back is in the right position for the particular stepmotor in use.

d) The PEM driving unit should be started. Check that the switch on the back of the driver is in external position.

D.3 Starting RASLab

The modulation control of the PEM is done by the RASLab software.

a) Be sure that the computer is on, and that the Windows operating system is functioning properly.

b) Start the RASlab 3 software.

c) Set the voltage on the photoelastic modulator from the software to a finite value, and observe the oscillation of the crystal on an oscilloscope connected to the gauge monitor output of the PEM driver.

d) Check that the position/wavelength of the monochromator is the same as the one given in the software.

e) Block the incoming rays on the detector, and adjust the amplification from software to F=100x. Adjust the offset at this amplification to zero by using the offset compensation knob on the back of the amplifier. This should be done after the warm-up period of the detector. Adjustment of the offset by the offset compensation knob should be done in front of every measurement.

D.4 Optical alignment

The next step in the measurement procedure is to check the optical alignment.

a) Do not move or change the setting of polariser.

b) Looking from the polariser towards the sample, the left spot of the double spot is the ordinary ray that should hit the sample.

c) The distance polariser-sample should be approximately 31 cm (25 – 50 cm).

d) Check that the reflected beam hits the PEM window.

e) Check that the analyser is adjusted to 45° with respect to a vertical line.

f) Adjust the analyser so that its face is normal to the beam.

g) Fine-tune mirror S3 and S4 in Figure 3.2 so that the beam is focused on to the monochromator.

h) Use the focus with vertical astigmatism to separate the ordinary and extraordinary beams at the monochromator input slit.

D.5 Check calibration

a) Adjust the monochromator to 633nm. The intensity on the detector (with a metal sample) is typically 2 – 4 V at amplification $F = 10$x at this wavelength.

b) Adjust the voltage of the photoelastic modulator to give an appropriate phase shift at the given wavelength.

c) Check that the sensitivity, filtering, harmonical frequency and phase of the lock-in amplifier is in the right position.

d) Check that the lock-in amplifier outputs a reasonable value. If not, recalibrate the optical set-up.

D.6 Starting the measurement

The measurement is started from the measurement menu of RASLab 3. Select frequency range, filename, number of samples per wavelength, PEM phase, real or imaginary part and time-constant of the lock-in. The current date and time is automatically added to the filename.

Appendix E. Numerical results from the LFE theory

In this chapter tabulated values for the plane-wise dipole-dipole interaction U^{nm}/a^3 in (4.9) is presented. All values are valid for the unreconstructed (110) face of a face-centred cubic crystal lattice. Table E.1 gives values for interaction between crystallographic planes, while the other tables are for interaction between a crystallographic plane and a mirror plane with effective surface height d as a parameter. The last column states the method(s) used to get the numerical value, according to the following list:

a: Direct summation
b: Hankeltransform
c: Method of van der Hoff & Benson, alternative 1
d: Method of van der Hoff & Benson, alternative 2

Table E.1. Plane-wise dipole-dipole interaction coefficients between crystallographic planes

n – m	s	U_{xx}^{nm}/a^3	U_{yy}^{nm}/a^3	U_{zz}^{nm}/a^3	Method
0	0	2.56268	13.5484	-16.1111	c
1	$1\cdot 2^{-3/2}$	8.38011	2.01158	-10.3917	a,c
2	$2\cdot 2^{-3/2}$	-1.41075	-0.417885	1.82863	a,b,c,d
3	$3\cdot 2^{-3/2}$	0.140854	0.010255	-0.151109	c
4	$4\cdot 2^{-3/2}$	-0.0154789	-6.04146E-4	0.016083	c,d
5	$5\cdot 2^{-3/2}$	1.67473E-3	2.26596E-5	-1.69739E-3	c
6	$6\cdot 2^{-3/2}$	-1.81709E-4	-1.05268E-6	1.82762E-4	c,d
7	$7\cdot 2^{-3/2}$	1.97052E-5	4.39232E-8	-1.97491E-5	c
8	$8\cdot 2^{-3/2}$	-2.13711E-6	-1.93152E-9	2.13905E-6	c,d
9	$9\cdot 2^{-3/2}$	2.31775E-8	8.2756E-11	-2.31858E-7	c
10	$10\cdot 2^{-3/2}$	-2.51366E-8	-3.59152E-12	2.51402E-8	c

Table E.2. Plane-wise dipole-dipole interaction coefficients on a crystallographic plane n from a mirror plane m', with effective surface height $d = 2.0 \cdot 2^{-5/2}$.

m'+ n	s	$U_{xx}^{nm'}/a^3$	$U_{yy}^{nm'}/a^3$	Method
0	$2 \cdot 2^{-3/2}$	-1.41075	-0.417885	c
1	$3 \cdot 2^{-3/2}$	0.140854	0.0102550	c
2	$4 \cdot 2^{-3/2}$	-0.0154789	-6.04145E-4	c
3	$5 \cdot 2^{-3/2}$	1.67473E-3	2.26596E-5	c
4	$6 \cdot 2^{-3/2}$	-1.81709E-4	-1.05268E-6	c
5	$7 \cdot 2^{-3/2}$	1.970518E-5	4.392317E-8	c
6	$8 \cdot 2^{-3/2}$	-2.137114E-6	-1.93152E-9	c
7	$9 \cdot 2^{-3/2}$	2.31775E-7	8.275596E-11	c
8	$10 \cdot 2^{-3/2}$	-2.51366E-8	-3.591518E-12	c

Table E.3. Plane-wise dipole-dipole interaction coefficients on a crystallographic plane n from a mirror plane m', with effective surface height $d = 1.5 \cdot 2^{-5/2}$.

m'+ n	s	$U_{xx}^{nm'}/a^3$	$U_{yy}^{nm'}/a^3$	Method
0	$1.5 \cdot 2^{-3/2}$	-4.81149	-2.33523	c
1	$2.5 \cdot 2^{-3/2}$	0.421069	0.0443769	c
2	$3.5 \cdot 2^{-3/2}$	-0.04713	-3.01571E-3	c
3	$4.5 \cdot 2^{-3/2}$	5.08293E-3	1.06688E-4	c
4	$5.5 \cdot 2^{-3/2}$	-5.51818E-4	-5.11339E-6	c
5	$6.5 \cdot 2^{-3/2}$	5.98347E-5	2.102365E-7	c
6	$7.5 \cdot 2^{-3/2}$	-6.489467E-6	-9.314056E-9	c
7	$8.5 \cdot 2^{-3/2}$	7.03795E-7	3.97614E-10	c
8	$9.5 \cdot 2^{-3/2}$	-7.63285E-8	-1.72862E-11	c

Table E.4. Plane-wise dipole-dipole interaction coefficients on a crystallographic plane n from a mirror plane m', with effective surface height $d = 1.1 \cdot 2^{-5/2}$.

m'+ n	s	$U_{xx}^{nm'}/a^3$	$U_{yy}^{nm'}/a^3$	Method
0	$1.1 \cdot 2^{-3/2}$	-14.7666	-10.11619	c
1	$2.1 \cdot 2^{-3/2}$	0.9961809	0.137366	c
2	$3.1 \cdot 2^{-3/2}$	-0.115167	-0.0110215	c
3	$4.1 \cdot 2^{-3/2}$	0.0123497	3.65939E-4	c
4	$5.1 \cdot 2^{-3/2}$	-1.34204E-3	-1.81571E-5	c
5	$6.1 \cdot 2^{-3/2}$	1.454937E-4	7.34618E-7	c
6	$7.1 \cdot 2^{-3/2}$	-1.578030E-5	-3.28125E-8	c
7	$8.1 \cdot 2^{-3/2}$	1.711392E-6	1.39520E-9	c
8	$9.1 \cdot 2^{-3/2}$	-1.85606E-7	-6.07775E-11	c

Table E.5. Plane-wise dipole-dipole interaction coefficients on a crystallographic plane n from a mirror plane m', with effective surface height $d = 1 \cdot 2^{-5/2}$.

m'+ n	s	$U_{xx}^{nm'}/a^3$	$U_{yy}^{nm'}/a^3$	$U_{zz}^{nm'}/a^3$	Method
0	$1 \cdot 2^{-3/2}$	-20.3247	14.9867	35.3113	c
1	$2 \cdot 2^{-3/2}$	1.23103	0.18071	-0.141174	c
2	$3 \cdot 2^{-3/2}$	-0.144083	-0.0152642	0.159347	c
3	$4 \cdot 2^{-3/2}$	0.0154169	4.97384E-4	-0.0159143	c
4	$5 \cdot 2^{-3/2}$	-1.67597E-3	-2.49367E-5	1.70091E-3	c
5	$6 \cdot 2^{-3/2}$	1.81684E-4	1.00412E-6	-1.82688E-4	c
6	$7 \cdot 2^{-3/2}$	-1.97057E-5	-4.49591E-8	1.97507E-5	c
7	$8 \cdot 2^{-3/2}$	2.1371E-6	1.90943E-9	-2.13901E-6	c
8	$9 \cdot 2^{-3/2}$	-2.31775E-7	-8.32268E-11	2.31858E-7	c

Table E.6. Plane-wise dipole-dipole interaction coefficients on a crystallographic plane n from a mirror plane m', with effective surface height $d = 0.9 \cdot 2^{-5/2}$.

m'+ n	s	$U_{xx}^{nm'}/a^3$	$U_{yy}^{nm'}/a^3$	Method
0	$0.9 \cdot 2^{-3/2}$	-28.6757	-22.60627	c
1	$1.9 \cdot 2^{-3/2}$	1.51818	0.236759	c
2	$2.9 \cdot 2^{-3/2}$	0.180328	-0.02115608	c
3	$3.9 \cdot 2^{-3/2}$	0.0192448	6.75648E-4	c
4	$4.9 \cdot 2^{-3/2}$	-2.09301E-3	-3.42551E-5	c
5	$5.9 \cdot 2^{-3/2}$	2.26875E-4	1.37231E-6	c
6	$6.9 \cdot 2^{-3/2}$	-2.46076E-5	-6.160578E-8	c
7	$7.9 \cdot 2^{-3/2}$	2.66871E-6	2.613105E-9	c
8	$8.9 \cdot 2^{-3/2}$	-2.89430E-7	-1.139703E-10	c

Table E.7. Plane-wise dipole-dipole interaction coefficients on a crystallographic plane n from a mirror plane m', with effective surface height $d = 0.5 \cdot 2^{-5/2}$.

m'+ n	s	$U_{xx}^{nm'}/a^3$	$U_{yy}^{nm'}/a^3$	Method
0	$0.5 \cdot 2^{-3/2}$	-178.498	-169.431	c
1	$1.5 \cdot 2^{-3/2}$	3.41248	0.662313	c
2	$2.5 \cdot 2^{-3/2}$	-0.444919	-0.0787485	c
3	$3.5 \cdot 2^{-3/2}$	0.0466876	2.28458E-3	c
4	$4.5 \cdot 2^{-3/2}$	-5.09165E-3	-122279E-4	c
5	$5.5 \cdot 2^{-3/2}$	5.51640E-4	4.78083E-6	c
6	$6.5 \cdot 2^{-3/2}$	-5.98383E-5	-2.17330E-7	c
7	$7.5 \cdot 2^{-3/2}$	6.48939E-6	9.16276E-9	c
8	$8.5 \cdot 2^{-3/2}$	-7.03797E-7	-4.00841E-10	c

Table E.8. Plane-wise dipole-dipole interaction coefficients on a crystallographic plane n from a mirror plane m', with effective surface height $d = 0.2 \cdot 2^{-5/2}$.

m'+ n	s	$U_{xx}^{nm'}/a^3$	$U_{yy}^{nm'}/a^3$	Method
0	$0.2 \cdot 2^{-3/2}$	-2764.9147	-2754.2675	c
1	$1.2 \cdot 2^{-3/2}$	5.97547	1.32926	c
2	$2.2 \cdot 2^{-3/2}$	-0.884666	-0.213429	c
3	$3.2 \cdot 2^{-3/2}$	0.0906238	5.64404E-3	c
4	$4.2 \cdot 2^{-3/2}$	-9.92051E-3	-3.18540E-4	c
5	$5.2 \cdot 2^{-3/2}$	1.07409E-3	1.21686E-5	c
6	$6.2 \cdot 2^{-3/2}$	-1.16524E-4	-5.59888E-7	c
7	$7.2 \cdot 2^{-3/2}$	1.26366E-5	2.34689E-8	c
8	$8.2 \cdot 2^{-3/2}$	-1.37048E-6	-1.02967E-9	c

References

[1] D.E. Aspnes and A.A. Studna, Phys. Rev. Lett. **54** (1985) 1956.

[2] V.L. Berkovits, L.F. Ivantsov, V.A. Kiselev, I.V. Makarenko, T.A. Minashvili, and V.I. Safarov. JETP Lett. **41** (1985) 551.

[3] O. Archer, R. Benferhat, B. Drevillon and M. Razeghi, in SPIE Vol. **1361** (1990) 1156.

[4] B. Koopmans, B. Richards, P.V. Santos, K. Eberl and M. Cardona, Appl. Phys. Lett. **69** (1996) 782.

[5] A. Zangwill, *Physics at surfaces*, Cambridge University Press (1988), page 171-174.

[6] C. Kittel, *Introduction to Solid State Physics,* Wiley (1966).

[7] P.E. Feibelman, Prog. Surf. Sci, **12** (1982) 287.

[8] D.E. Aspnes, J.P. Harbison, A.A. Studna and L.T. Florez, Appl. Phys. Lett. **52** (1988) 957.

[9] J.D. Jackson, *Classical Electrodynamics*, Wiley (1975), page 310-312.

[10] M. Reigstad, *Konstruksjon, bygging og testing av et kompakt refleksjon-anisotropi-spektroskopi system*, Project report, NTNU (1998).

[11] E. Klaveness and G. Risberg, *Refleksjon-anisotropi-spekroskopi ved bruk av Wollaston-prisme*, Project report, NTNU (1997).

[12] L. Bleckman, O. Hunderi, W. Richter and E. Wold, Surf. Sci. **351** (1996) 277.

[13] J. Rumberg, *Development and Optimization of the Reflectance Anisotropy Spectroscopy (RAS) Technique with respect to Online Growth Control*, Diploma Thesis, TU-Berlin (1996).

[14] M. Stchakovsky, *Conception et realisation d'un ellipsometre spectroscopique a modulation de phase*, Ph.D. Thesis, Universite de Paris-Sud Centre d'Orsay (1991).

[15] J. Tarriba and W.L. Mochán, Phys. Rev. B **46** (1992) 12902.

[16] J.D. Jackson, *Classical Electrodynamics*, Wiley (1975), page 153.

[17] C.A. Scholl. Proc. Phys. Soc. **87** (1966) 897.

[18] B.M.E. van der Hoff og G.C.Benson, Can. J. Phys. **31** (1953) 1087.

[19] N. Kar and A. Bagchi, Sol. State Com. **33** (1980) 645.

[20] Y. Borensztein, W.L. Mochan, J. Tarriba, R.G. Barrera and A. Tadjeddine, Phys. Rev. Lett. **71** (1993) 2334.

[21] P.B. Johnson and R.W. Christy, Phys. Rev. B **6** (1972) 4370.

[22] S.M. Scholz, A.B. Müller, W. Richter, D.R.T. Zahn, D.I. Westwood, D.A. Wolf and R.H. Williams, J. Vac. Sci Technol. **10** (1992) 1710.

[23] Ph. Hofmann, K.C. Rose, V. Fernandez, A.M. Bradshaw and W. Richter, Phys. Rev. Lett. **75**, (1995) 2039.

[24] W.L. Mochán and R.G. Barrera, Phys. Rev. Lett. **55** (1985) 1192.

[25] M.Y. Jiang, G. Pajer and E. Burnstein, Surf. Sci. **242** (1991) 306.

[26] L.E. Urbach, H.L. Percival, J.M. Hicks, E.W. Plummer and H.-L. Dai, Phys. Rev. B **45** (1992) 3769.

[27] V. Fernandez, D. Pahlke, N. Esser, K. Stahrenberg, O. Hunderi, A.M. Bradshaw and W. Richter, Surf. Sci. **377** (1997) 388.

[28] K.-M. Ho, B.N. Harmon and S.H. Liu, Phys. Rev. Lett. **44** (1980) 1531.

[29] D. E. Aspnes, J.P. Harbison, A.A. Studna, L.T. Florez and M.K. Kelly, J. Vac. Sci. Technol. A, **6** (1988) 1327.

[30] J.-K. Hansen, J. Bremer and O. Hunderi, Surf. Science **418** (1998) L58

[31] R. Courths, S. Hüfner, P. Kemkes and G.Wiesen, Surf. Sci. **376** (1997) 43.

[32] W.L. Mochan, R.G. Barrera, Y. Borensztein and A. Tadjeddine, Physica A **207** (1994) 334.

[33] K. Stahrenberg, T. Hermann, N. Esser, J. Sahm, W. Richter, S.V. Hoffmann, Ph. Hoffmann, Phys. Rev. B **58** (1998) R10207.

[34] R. Cuorno, H.A. Makse, S. Tomassone, S.T. Harrington and H.E. Stanley, Phys. Rev. Lett. **75** (1995) 4464.

[35] Z. Csahok, Z. Farkas, M. Menyhard, G. Gergely and Cs.S. Daroczi, Surface Science **364** (1996) L600.

[36] J. Naumann, J. Osing, A.J. Quinn and I.V. Shvets, Surface Science **388** (1997) 212.

[37] A. C.-T. Chan and G.-C. Wang, Surface Science **414** (1998) 17.

[38] S. Rusponi, C. Boragno, and U. Valbusa, Phys. Rev. Lett. **78** (1997) 2795.

[39] E.A. Eklund, E.J. Snyder and R.S. Williams, Surf. Science **285** (1993) 157.

[40] P. Bedrossian and T. Klitsner, Phys. Rev. B **44** (1991) 13783.

[41] G. Ehrlich and F.G. Hudda, J. Chem. Phys. **44** (1966) 1039.

[42] P. Meakin, Phys. Rep. **235** (1993) 189.

[43] J. Bremer, J.-K. Hansen, and O. Hunderi, Appl. Surf. Sci. **142** (1999) 286.

[44] J.-K. Hansen, J. Bremer and O. Hunderi, Phys. Stat. Sol. (a) **170** (1998) 271.

[45] B.R. Cooper, H. Ehrenreich and H.R. Philipp, Phys. Rev. A **138** (1965) 494.

[46] G.A. Held, J.L. Jordon-Sweet, P.M. Horn, A. Mak and R. J. Birgenau, Phys. Rev. Lett. **59** (1987) 2075.

[47] I.K. Robinson, E. Vlieg, H. Hornis and E. H. Conrad, Phys. Rev. Lett. **67** (1991) 1890.

[48] S.V. Khare and T.L. Einstein, Phys. Rev. B **57** (1998) 4782.

[49] P. Winsemius, F.F. van Kampen, H.P. Lengkeek and C.G. van Went, J. Phys. F: Metal Phys. **6** (1976) 1583.

[50] E.D. Palik, *Handbook of Optical Constants of Solids*, Academic Press, Boston (1985), page 351.

[51] P.J. Feibelmann, Phys. Rev. B **9** (1974) 5077.

[52] M. Rocca, M. Lazzarino and U. Valbusa, Phys. Rev. Lett. **69** (1992) 2122.

[53] L. Yibing, A.C. Levi and M. Rocca, Surface Science **336** (1995) 371.

[54] A. Tadjeddine, D.M. Kolb, and R. Kötz, Surface Science **101** (1980) 277.

[55] A. Liebsch, *Electronic Excitations at Metal Surfaces*, Plenum Press, New York (1997).

[56] G. Lee, P.T. Sprunger and E.W. Plummer, Surface Science **286** (1993) L547.

[57] T. Yasuda, L. Mantese, U. Rossow and D. E. Aspnes, Phys. Rev. Lett. **74** (1995) 3431.

[58] D.E. Aspnes, L. Mantese and K.A. Bell, J. Vac. Sci. Technol. B **16** (1998) 2367.

[59] J. Bremer, J.-K. Hansen and O. Hunderi, Surf. Sci. Lett. **436** (1999) 735.

[60] D. Beaglehole and O. Hunderi, Phys. Rev. B **2** (1970) 309.

[61] O. Hunderi and D. Beaglehole, Phys. Rev. B **2** (1970) 321.

[62] S.N. Jasperson and S.E. Schnatterly, Phys. Rev. **188** (1969) 759.

[63] J.M. Elson and R.H. Ritchie, Phys. Stat. Sol. (b) **62** (1974) 461.

[64] J.M. Elson and R.H. Ritchie, Phys. Rev. B **4** (1971) 4129.

[65] E. Kretschmann and E. Kröger, J. Opt. Soc. Am. **65** (1975) 150.

[66] H. Raether, *Surface Plasmons*, Springer, Berlin (1988).

[67] M. Rocca and U. Valbusa **287/288** (1993) 770.

[68] K.-D. Tsuei, E.W. Plummer, A. Liebsch, E. Pehlke and P. Bakshi, Surf. Science **247** (1991) 302.

[69] F. Moresco, M. Rocca, V. Zielasek, T. Hildebrandt and M. Henzler, Phys. Rev. B **54** (1996) R141333.

[70] E.W. Plummer, Sol. State Comm. **84** (1992) 143.

[71] A. Liebsch, Phys. Rev. B **57** (1998) 3803.

[72] P. Pollak, R. Courths and St. Witzel, Surf. Sci. Lett. **255** (1991) 523.

[73] A. Borg, O. Hunderi, W. Richter, J. Rumberg, H.J. Venvik, Phys. Stat. Sol. (a) **152** (1995) 77.

[74] F. Abelés, *Optical Properties of metals*, in *Optical properties of solids*, edited by F. Abelés, North-Holland (1972).

[75] G. Harbeke, *Optical Properties of semiconductors*, in *Optical properties of solids*, edited by F. Abelés, North-Holland (1972).

[76] A. Borg, A,-M. Hilmen and E. Bergene, Surf. Sci. **306** (1994) 10.

[77] A. Zangwill, *Physics at surfaces*, Cambridge University Press (1988), page 116.

[78] W.L. Mochán, R.G. Barrera, Y. Borensztein and A. Tadjeddine, Physica A **207** (1994) 334-339.

[79] D.G. Fedak and N.A. Gjosten, Surf. Sci. **8** (1967) 77.

[80] D. Passerone, F. Ercolessi and E. Tosatti, Surf. Sci. **377** (1997) 27.

[81] P. Heilmann, K. Heinz and K. Müller, Surf. Sci. **83** (1979) 487.

[82] D.L. Abernathy, D. Gibbs, G. Grübel, K.G. Huang, S.G.J. Mochrie, A.R. Sandy and D.M. Zehner, Surf. Sci. **283** (1993) 260.

[83] O. Wiener, Abh. Math.-Phys. Kl. Königlich Saechs. Ges. **32** (1912) 509.

[84] A. Goldmann, M. Donath, W. Altmann and V. Dose, Phys. Rev. B **32** (1985) 837.

[85] C.T. Chen and N.V. Smith, Phys. Rev. B **33** (1986) 3740.

[86] O. Hunderi, unpublished.

[87] Database of optical indices, Sopra SA, France, (http://www.sopra-sa.com/indices.htm).

[88] Y. Kantor and D. Bergman, J. Phys. C: Solid State Phys., **15** (1982) 2033.

[89] J. Bremer, J.-K. Hansen, K. Stahrenberg and T. Worren, Surf. Sci., in print.